TROUBLESHOOTING ULTRASHORT PULSE MEASUREMENT:

THE COHERENT ARTIFACT AND OTHER ISSUES

A Thesis
Presented to
The Academic Faculty

by

Michelle Ann Rhodes

In Partial Fulfillment
of the Requirements for the Degree
Doctor of Philosophy in the
School of Physics

Georgia Institute of Technology
May 2016

TROUBLESHOOTING ULTRASHORT PULSE MEASUREMENT:

THE COHERENT ARTIFACT AND OTHER ISSUES

Approved by:

Dr. Rick Trebino, Advisor
School of Physics
Georgia Institute of Technology

Dr. Chandra Raman
School of Physics
Georgia Institute of Technology

Dr. Jennifer Curtis
School of Physics
Georgia Institute of Technology

Dr. Joseph Perry
School of Chemsitry
Georgia Institute of Technology

Dr. Turgay Uzer
School of Physics
Georgia Institute of Technology

Date Approved: 03/10/2016

ACKNOWLEDGEMENTS

I would first like to thank my parents for their unwavering support of my educational goals and for being excellent role models to a young scientist.

I owe a huge debt to my advisor, Rick Trebino, and to my colleague, Justin Ratner, for conceiving of and beginning the coherent artifact project.

I have had many valuable collaborators over the course of this project. I am deeply grateful to Günter Steinmeyer, Jonathan Birge, Saidur Rahaman, Marin Iliev, Madhuri Mukhopadhyay, and Alberto Comin for their assistance with this research. I would also like to thank the many people in my research group who have helped me over the years, including Jeff Wong, Zhe Guang, Ping Zhu, Matt Davis, Ramprasath Rajagopal, and Justine Stiftel.

I would finally like to acknowledge the support of my brothers of the Gamma Tau chapter of the Psi Upsilon Fraternity. Their mighty friendship has sustained me throughout my graduate career. I could not have asked for a better support system.

TABLE OF CONTENTS

LIST OF FIGURES

LIST OF SYMBOLS

t	time
δt	time resolution of simulation
ω	angular frequency
$\delta\omega$	frequency resolution of simulation
E	complex electric field
φ, $\varphi(\omega)$	spectral phase
τ, $\tau(\omega)$	group delay
ϕ	other phase
T	delay
G	root mean square difference between measured and retrieved FROG traces
Ω	spectral shear
θ	relative phase of double pulses
t_s	temporal separation of double pulses
σ_t	Gaussian temporal pulse width
f	frequency of phase modulation
Φ_0	amplitude of phase modulation
ψ	phase offset of phase modulation
N	number of time/frequency points in simulation
x	transverse spatial coordinate
y	transverse spatial coordinate
k, k_x	transverse spatial frequency or off-axis propagation vector, Fourier pair of x
k_y	transverse spatial frequency or off-axis propagation vector, Fourier pair of y

LIST OF ABBREVIATIONS

2DSI	Two Dimensional Spectral shearing Interferometry
CW	continuous wave
FROG	Frequency Resolved Optical Gating
FTSI	Fourier Transform Spectral Interferometry
FWHM	full width at half-maximum
MIIPS	Multiphoton Intrapulse Interference Phase Scan
PG	polarization gating
RGB	red, green, and blue
RMS	root mean square
SEA	Spatially Encoded Arrangement (for)
SHG	second-harmonic generation
SPIDER	SPectral Interferometry for Direct Electric-field Reconstruction
SRSI	Self-Referenced Spectral Interferometry
STRIPED FISH	Spatially and Temporally Resolved Intensity and Phase Evaluation Device: Full Information from a Single Hologram
TADPOLE	Temporal Analysis by Dispersing a Pair Of Light E-fields
XFROG	Cross-correlation Frequency Resolved Optical Gating
XPW	Cross-Polarized Wave generation

SUMMARY

Theoretical limitations of several ultrashort pulse measurement techniques are investigated. Particular attention is paid to the consequences of averaging over many pulses of different shapes. Averaging over many pulses is a very common practice, and if the pulse shape varies then the measurement result will be incorrect. This issue, referred to as a coherent artifact, is simulated for frequency-resolved optical gating using several nonlinearities, spectral interferometry for direct electric field reconstruction, two-dimensional spectral shearing interferometry, self-referenced spectral interferometry using cross-polarized wave generation, and multiphoton intrapulse interference phase scan. The role of measurement feedback in identifying pulse-shape instability is explored where possible. Several techniques receive additional analysis, such as searching for ambiguities or simulating convergence conditions. In addition, a method for intuitively displaying spatiotemporally distorted pulses is explored and developed.

CHAPTER 1

THE COHERENT ARTIFACT IN INTENSITY AUTOCORRELATION

An ideal measurement technique is not only accurate, but also robust. If the accuracy of a measurement is too easily compromised by difficult experimental circumstances, then extreme care must be taken in interpreting its results. In particular, multi-shot pulse-shape measurements of unstable pulse trains have yielded confusing or misleading results. The multi-shot measurement necessarily involves contributions from an ensemble of different events, which cannot be directly represented in the measurement result. It is therefore fundamentally impossible for any multi-shot measurement of an unstable pulse train to yield a truly accurate result. This is especially problematic because this ensemble measurement may not reflect typical characteristics of the pulse train. Because single-shot measurements are difficult to perform with most laser sources due to low pulse energies and long camera integration times, it is important for a pulse-measurement method to yield a reasonable average result. Further, it is very important that the method indicate whether its measurement averages over different events versus identical events.

Specifically, intensity-autocorrelation measurements of trains of differing pulses are well-known to yield a narrow spike at zero delay atop a broad background. The spike, referred to now as the "coherent artifact," is a measure of the coherent, nonrandom, or repeatable component of the pulse train. While some have mistakenly interpreted its width as a measure of the pulse width, the broad background is the correct indicator of the actual pulse width. And the presence of a coherent artifact actually indicates instability or complexity in the pulse train. More precisely, the coherent artifact

represents only the shortest repeatable substructure in the pulses and ignores any variations between the pulses.

Historical Overview

The coherent artifact has caused confusion in laser pulse measurement for almost as long as pulse measurements have been conducted. When laser pulses broke the nanosecond barrier, fast electronics were no longer fast enough to measure them. As a result, researchers turned to nonlinear optics to help determine how short these pulses were. The intensity autocorrelation, which is the nonlinear signal generated by two pulse replicas as a function of delay between them, emerged as essentially the only method for measuring short pulses [1-3]. One of the most widely-used measurement setups involved counter-propagating two pulses to generate variations in delay as a function of space, and recording the scattered two-photon fluorescence signal from the side with a camera.

In the late 1960s, significant confusion arose when researchers noticed that peaks could be observed in intensity-autocorrelation measurements even when the lasers involved were not mode-locked [4-6]. In 1968, several authors [7, 8] used previous work on light coherence [9, 10] and correlation functions [11, 12] to explain the variety of autocorrelation traces that could result from measuring laser light. It was established that a peak always appears at zero delay in an autocorrelation [8, 13-17] unless the light under measurement is perfectly monochromatic and has an infinite coherence length. All broadband sources yield a central peak, and the width of this peak is approximately equal to the inverse spectral width, called the coherence time [16, 17]. This peak should not be assumed to be indicative of a short pulse. It is sometimes called a coherent artifact because it arises from coherence effects, but it occurs in single-shot measurements involving only the pulse intensity (e.g. autocorrelation) and should not be confused with multi-shot phenomena discussed later. In addition to a central peak, autocorrelations of complex pulses will also show a pedestal [14, 18, 19]. The relative strengths of the

pedestal and coherence peak provide useful information about pulses. For example, broadband fluorescence and white-light sources have a coherence spike but no pedestal. Such sources usually have much longer pulse lengths, so their pedestals are difficult to separate from the usual two-photon fluorescence background. Imperfect mode-locking of lasers tends to yield shorter, noisy pulses whose autocorrelations have cusp-like coherence spikes on top of a noticeable broad pedestal. A fully mode-locked laser yielding transform-limited pulses has a very strong coherence peak and no pedestal. For good reviews of this discovery process, see [14] and [17].

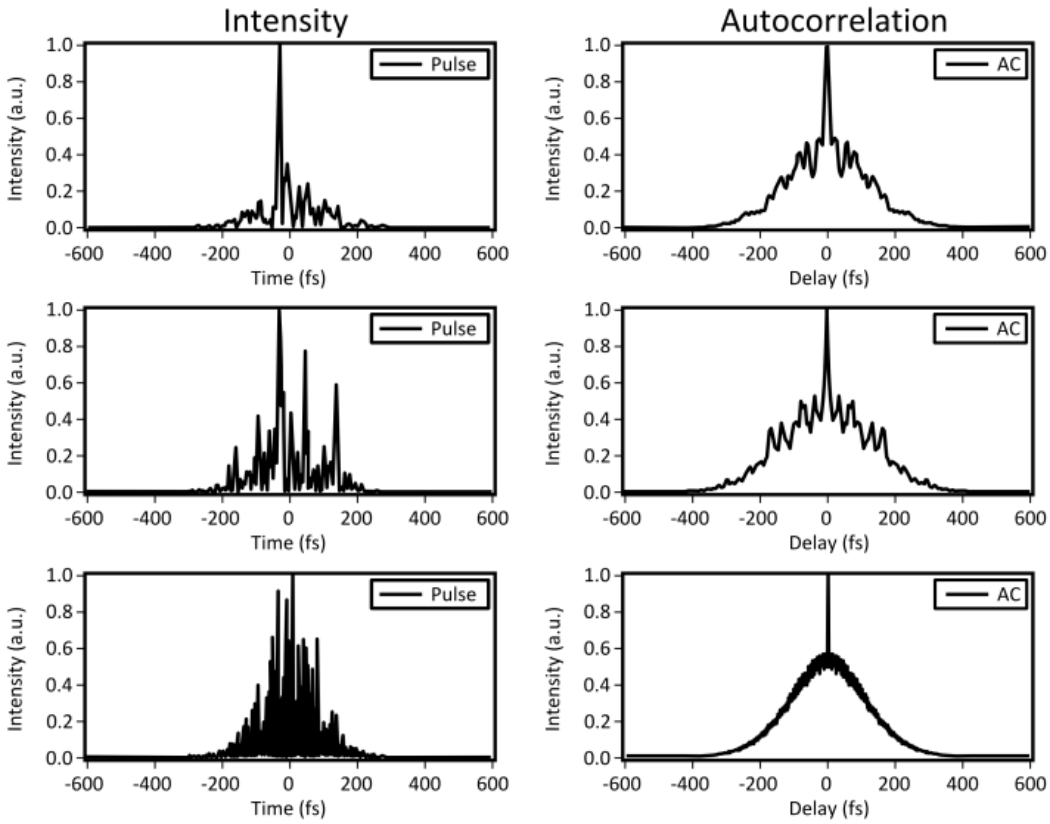

Figure 1.1: Single-shot intensity autocorrelations of pulses of increasing complexity [5]. Very complex pulses actually have very simple autocorrelations. Note the coherence spike in each autocorrelation, which indicates only the coherence time of the pulse, and not the pulse length. This coherence time indicates the characteristic temporal modulation period within the much wider enveloping structure of the pulse. These pulses are typical of what one would expect from lasers that are not mode-locked.

Once clear criteria for measurements that showed true short pulses, not just coherent artifacts, had been established and experimentally verified [14, 20, 21], attention turned to the shape of the autocorrelation, especially the pedestal. The pedestal defines the temporal resolution in spectroscopic pump-probe experiments and is therefore of far greater interest than the shorter coherence time. The temporal duration of the enveloping pulse profile is consequently referred to as the pulse duration in the following, because the duration of individual sub-pulses is of little relevance for time-resolved experiments. Even though several authors noted that the contrast and shape of the autocorrelation and pedestal were not particularly sensitive to the pulse profile [19, 22-25], there were no alternative optical measurement techniques available at the time. The problem was complicated by the fact that actual pulse lengths were typically much longer than the corresponding coherence time [8, 21], signifying that some phase distortions must be present. This problem was even further complicated by the fact that most TPF measurements, with only a few exceptions [26], were in fact averages over many pulses in a pulse train. Because the intensity-autocorrelation pulse-retrieval problem had so many ambiguities, researchers could only guess at the actual pulse distortions present [22, 27, 28].

As a result, misinterpretations were common. For example, Treacy believed that he had fully compressed his pulses by compensating for positive frequency chirp [29, 30]. However, Fisher and Fleck [31] pointed out that Treacy's results (showing a short spike atop a broad background) were consistent with the output pulses of the laser each having a different random walk for their phase versus time. Compensating such pulses for positive chirp would result in random temporal structure in the intensity that varied from pulse to pulse. The multi-shot autocorrelation of such a train of pulses would be the same as that reported by Treacy, and his results therefore did not prove that the uncompensated pulses had positive chirp. This was the first identification of the multi-

shot coherent artifact. The insight that a train of varying pulses could mimic a shorter-pulse, stable train in a measurement was quite surprising.

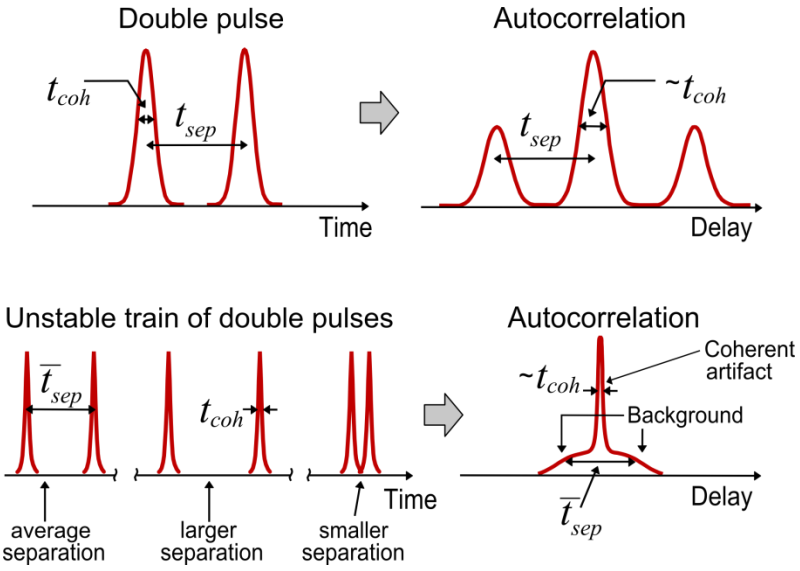

Figure 1.2: The coherent artifact in autocorrelation. Top: Double pulse and its background-free autocorrelation [32]. Bottom: A train of variably spaced double pulses and their multi-shot autocorrelation. The coherent artifact results from the short nonrandom coherent component of the double pulses (a single pulse), while the broader background results from the overall average pulse length (the combination of both pulses). This trace is typical of autocorrelations of nearly all trains of unstable, complex pulses.

As laser technology improved and pulse trains became more stable, these types of issues became less prominent but did not disappear. In the late seventies, researchers had trouble matching autocorrelations of synchronously pumped dye lasers with a pulse shape [33-36]. The closest pulse profile was a single-sided exponential pulse; however, Van Stryland [37] argued that the autocorrelations were also consistent with a train of Gaussian pulses with a distribution of pulse widths. Birmontas *et. al.* [38] extended Van Stryland's analysis to include variations in pulse energy as well as duration and showed that the autocorrelation underestimates the average pulse length of unstable trains when the fluctuations in pulse power and length are correlated. It took more than a decade to unveil the physics behind the observed unstable synchronously pumped mode-locking and to find a means for stabilization of the mode-locking process [39, 40].

The non-uniqueness of the autocorrelation function [41-43] combined with the possibility of unstable trains remained a significant problem for laser pulse measurement until the development of more powerful pulse-measurement techniques and further improvements in laser technology. Unlike autocorrelation, modern pulse measurement techniques do not suffer from non-uniqueness (except for trivial ambiguities) and provide not only the intensity profile, but also the phase of pulses. However, their reliability in the face of pulse trains with pulse-shape instabilities has only recently begun to be examined in detail [32, 44]. And while synchronous pumping has been widely replaced by more robust and stable passive mode-locking techniques, unstable pulse trains often still arise, especially in supercontinuum compression experiments [45-47].

In conclusion, practitioners of ultrafast optics should remain cautious about the stability of their pulses and should interpret their measurements accordingly. It should *not* be taken as given that all modern passive mode-locking techniques for bulk lasers always produce stable pulse trains. And the burden of proof that a new design yields a stable pulse train is, as always, on the researcher reporting it. Care is especially necessary when characterizing white-light supercontinuum pulses and their possible compression. Pulse break-up instabilities are common in white-light generation in microstructure fibers [44-46], filaments [48], and also mode-locked fiber lasers [49, 50].

What types of variations don't cause a coherent artifact?

While instabilities besides pulse-shape fluctuations certainly exist, they are typically of little relevance for ultrashort pulse measurement techniques, in particular if the techniques are completely self-referenced. Beam pointing fluctuations as well as pulse energy variations may certainly increase the noise levels in the detection and require suitable averaging techniques [51]. Carrier-envelope phase fluctuations [52] could be another possible noise source for few-cycle laser pulses. Such effects can clearly be seen when measuring cross-correlations or interferograms using two

subsequent pulses from a pulsed laser source [53, 54]. It is understood, however, that carrier-envelope effects could otherwise only pose an issue for pulses whose coherent spectra span more than an octave [55], a situation far less common than the coherence spike. Moreover, all mode-locked lasers exhibit pulse timing jitter [56], which is typically characterized by RF measurement techniques [57]. However, such techniques do not have the resolution to measure ultrashort pulse shapes or pulse-shape fluctuations, making them ill-suited to many applications where intensity and phase measurements are used. All measurement techniques discussed in the following analysis employ pulse-replicas that are derived from the same oscillator or amplifier pulse. Pulse arrival time cannot be measured in this case, and variations in arrival time are unobservable. Even the cross-correlation variants of measurement techniques nearly always use an undistorted pulse from the same laser as a reference, removing the problem of synchronizing multiple laser sources. This makes these pulse measurement techniques completely immune to timing jitter noise. More importantly, none of the noise sources mentioned above cause a multi-shot coherence spike, as pulse-shape instabilities do.

Goals of this Thesis

When considering the possibility of pulse-shape instabilities, it becomes clear that an intensity-and-phase pulse-shape measurement has a responsibility to give some measure of the reliability of its result, which should include the stability of the pulse train. In particular, the technique should not introduce new non-trivial ambiguities resulting in confusion, for example, between a stable train of very short pulses and an unstable train of much longer ones. Given that a measurement can only give a single intensity and phase, and so cannot represent all the pulses of an unstable train, a good measurement technique should still give an approximation of a typical pulse. In addition, it is vital that there are indicators of instability. Although many modern pulse-measurement techniques have single-shot capability, including several of the techniques

discussed in this thesis, multi-shot measurements are extremely common in practice. Consequently, pulse-measurement techniques must be evaluated to determine how they respond to averaging over unstable pulse trains.

In the following chapters, we will simulate the responses of many pulse measurement techniques to varying pulse trains. We will discuss how to differentiate measurements of stable and unstable trains in each of them and make recommendations for convincing measurements. While many techniques are not able to provide representative pulses when faced with an unstable laser source, several are capable of providing clear indicators of instability. Because the progress of ultrafast science relies on developing ever more reliable and accurate measurement techniques, understanding the effects of instability is extremely important.

CHAPTER 2

CREATING PULSE TRAINS FOR SIMULATED MEASUREMENTS

In order to understand the behavior of pulse measurement techniques for varying pulse trains, we constructed pulse trains that had both a stable component and an unstable component. The stable component was consistent in each pulse while the unstable component was different in every pulse. This structure allowed us to understand how the measurement technique reacted to each component. Since we wanted to be able to control the average length and complexity of the pulses, we needed have an adjustable method of randomly generating the unstable pulse component. Over the course of our studies, two different methods were used to create the unstable pulse component.

Pulse Trains Used in Previous Work

The first method used was developed by a former student in our group, Justin Ratner. Justin's approach was to take the spectrum of the stable component as a starting point. He then generated a random spectral phase by assigning each frequency a phase between 0 and 2π, and then smoothing the phase with moving average. The width of the moving average window determined the strength of the variations in the spectral phase. This unstable component was then added to the stable component to generate a pulse. Using this method, Justin generated two trains of fairly short pulses, one train with pulses about twice as long as the stable component and another train with pulses about 4.5 times as long as the stable component. Each pulse train contained 5000 pulses.

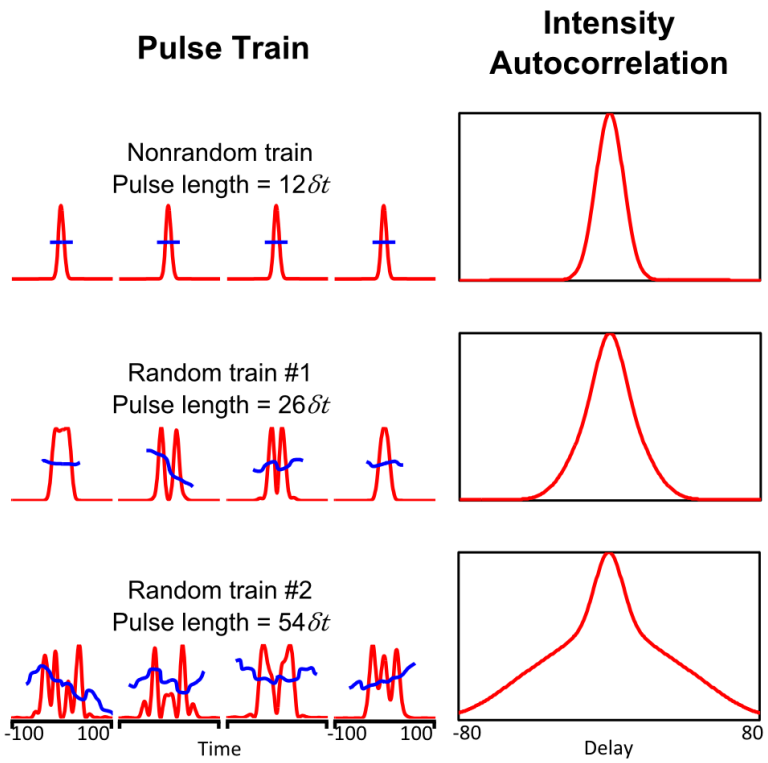

Figure 2.1: Pulse trains and their autocorrelations. Left column: Example pulses from the pulse trains created by Justin [32]. Red is temporal intensity and blue is temporal phase. Right column: the average intensity autocorrelation of the whole pulse train.

There were two issues I discovered with this approach. First, it is difficult to get very complicated random pulse components. Smoothing the uniformly random spectral phase by any amount resulted in a phase with very little variation. The spectral phase of these unstable components was always close to π, with small local deviations. The unstable components were consequently very simple pulses. The reason that Justin was able to generate interesting random pulses using this method is because the unstable component tended to be out of phase with the stable component. The two pulse components nearly cancel out, and only the variations in the unstable pulse survive. Even though the total pulses are moderately complex, the unstable components are not. If we wanted to generate more complicated unstable components, we would have to use a different method.

The second issue with Justin's approach is that because the pulses were generated from stable and unstable components canceling out, the absolute phase of the pulses was always close to $\pm\pi/2$. While self-referenced techniques are oblivious to the absolute phase, techniques using a reference pulse will be unnecessarily confused by a pulse train that is so strongly anti-correlated. In addition, we would prefer the absolute phase of the unstable component to be uniformly random, rather than having a preferential value.

Pulse Trains Created for This Work

With these issues in mind, my goal was to create a second set of pulse trains that were more complicated and had a uniformly random absolute phase. I chose the stable component to be a flat phase Gaussian with temporal FWHM $20\,\delta t$, where δt is the temporal sampling rate. The frequency sampling rate is $\delta\omega = 2\pi/N\delta t$, where N is the array size (4096). Similarly to Justin, the unstable component started with the same spectrum as the stable component.

Instead of generating a random spectral phase and then smoothing it, I applied the random spectral phase and then computed the Fourier transform of the unstable component. I then applied a wide Gaussian envelope (or filter) in the time domain (see Fig. 2.2). Since this process gates out a significant portion of the energy in the unstable component, its energy must be increased to be of comparable intensity to the stable component. I multiplied the amplitude of the unstable component by a constant so that, on average, it had similar intensity at $t = 0$ to the nonrandom component. Consequently, the energy contained in the random pulse component is larger than in the stable pulse component, since the random component is much longer in time. The random and stable components were then added together to create a pulse. I made sure that the amplitude adjustment was appropriate afterward by calculating the average intensity profile of the train and checking that the transition from the nonrandom spike to a broad background

occurred near 50% of the peak intensity. The average temporal width and complexity of the pulses in the train was adjusted by changing the width of the Gaussian time envelope.

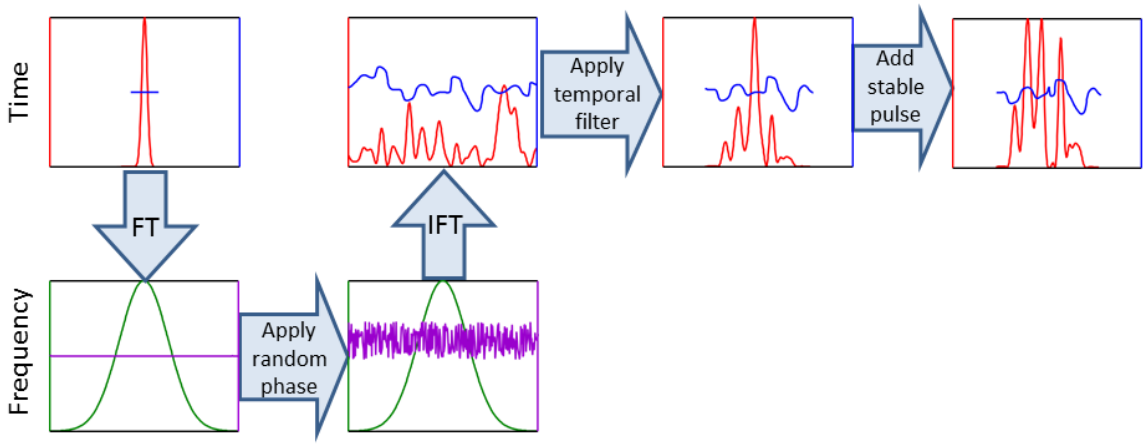

Figure 2.2: Pulse creation flowchart. Red is temporal intensity, blue is temporal phase, green is spectral intensity, and purple is spectral phase.

Two pulse trains were constructed (see examples in Fig. 2.3). The first train used a time envelope with a width of 100 δt, which resulted in a train with an average FWHM pulse length of 59 δt. The second used a time envelope with a width of 300 δt to generate a train with average length 192 δt. These pulse trains contained 5000 pulses each. The average spectra of both trains were nearly identical to the spectrum of the nonrandom component, even though the spectra of individual pulses were quite different. The same two random pulse trains were used to compute traces for all the measurement techniques I studied. Figure 2.3 shows the intensity autocorrelations of these pulses.

The number of pulses in each train (5000) is chosen to be relatively consistent with common experimental practice. Typical cameras have an exposure time on the order of tenths of a second, meaning that even kilohertz-rep-rate systems can average over several hundred pulses in a single frame, and the more common megahertz-rep-rate systems average over considerably more than 5000 pulses.

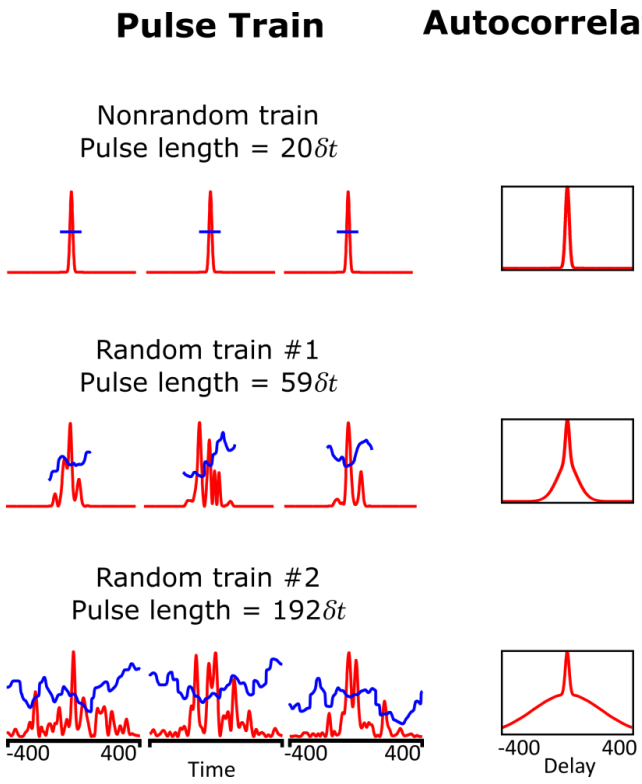

Figure 2.3: New pulse trains and their autocorrelations [58]. Left column: Example pulses from the pulse trains created for this work. Red is temporal intensity and blue is temporal phase. Right column: the average intensity autocorrelation of the whole pulse train. Note the differences in delay scale from Fig. 2.1.

Coherence Properties of the Pulse Trains

In order to allow comparisons between the coherence properties of these pulse trains and other works, the resulting coherence of the trains is computed from the modulus of the complex degree of first-order coherence [59]:

$$\bar{g}^{(1)}(\omega) = \left| \frac{\langle E_i^*(\omega) E_j(\omega) \rangle_{i \neq j}}{\sqrt{\langle |E_i(\omega)|^2 \rangle \langle |E_j(\omega)|^2 \rangle}} \right| \tag{2.1}$$

where indices i and j label numerically generated individual spectra $E_i(\omega)$ and $E_j(\omega)$, respectively, and ω is the angular frequency. Figure 2.4 shows the resulting coherence averaged over all pulse combinations for the pulse train with an average FWHM pulse length of 59 δt as well as that for length 192 δt. In both cases, maximum coherence is reached near the center frequency $\delta\omega = 0$, with $\bar{g}^{(1)}$values of about 0.14 and 0.04,

respectively. For the case of 59 δt, the coherence quickly decreases further away from the center frequency, whereas it stays nearly constant for 192 δt. As perfect coherence is indicated by $\bar{g}^{(1)} = 1$, it is plain to see that noise increases with increasing FWHM pulse length in our parameterization of the problem.

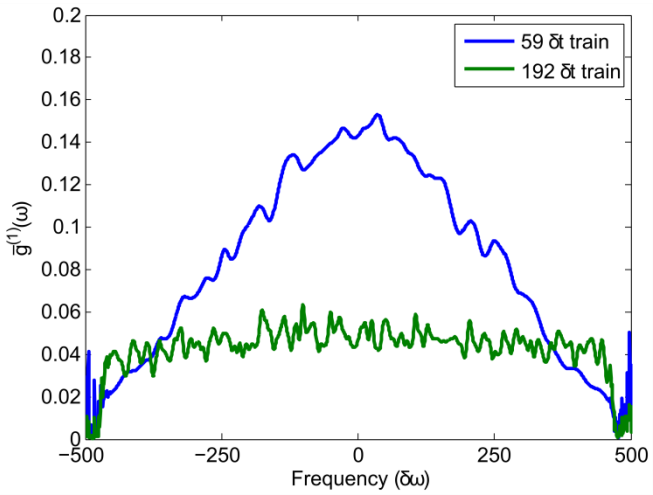

Figure. 2.4: Average modulus of the complex degree of first-order coherence $\bar{g}^{(1)}(\omega)$ for the two pulse trains considered in the simulations [58]. Perfect coherence, i.e., identical pulse shapes in the train are indicated by $\bar{g}^{(1)} = 1$.

CHAPTER 3

THE COHERENT ARTIFACT IN FREQUENCY-RESOLVED OPTICAL GATING (FROG)

At the beginning of this project, we hypothesized that FROG would perform well for unstable pulse trains. This expectation was based on an experiment done several years earlier, in which our group attempted to measure supercontinuum pulses [44]. Unbeknownst to us at the time, these pulses are extremely complicated and vary significantly from pulse to pulse. Because the measurement averaged over millions of different pulses, the retrieval could not find a single pulse that matched the measured trace. As a result, there were significant differences between the measured and retrieved traces, both numerically and visually. These differences are very important in identifying a measurement of an unstable pulse train.

Basics of FROG

FROG is a spectrally resolved autocorrelation, also known as a spectrogram [60]. The general expression for a FROG measurement is:

$$I_{FROG}(\omega, T) = \left| \int_{-\infty}^{\infty} E(t) E_g(t - T) \exp(-i\omega t)\, dt \right|^2 \tag{3.1}$$

This is the Fourier transform of the signal field, created by the interaction of the pulse, $E(t)$, and its gate, $E_g(t - T)$, in a nonlinear medium. The resulting measurement is a function of both frequency ω and delay T. The gate function depends on the nonlinearity. For second harmonic generation (SHG) FROG, the gate is the field itself (see Fig. 3.1). The corresponding trace expression is:

$$I_{SHG\ FROG}(\omega, T) = \left| \int_{-\infty}^{\infty} E(t) E(t - T) \exp(-i\omega t)\, dt \right|^2 \tag{3.2}$$

For polarization-gating (PG) FROG, the gate is the intensity of the field. The trace expression for PG FROG is :

$$I_{PG\ FROG}(\omega, T) = \left|\int_{-\infty}^{\infty} E(t)E(t-T)\exp(-i\omega t)\,dt\right|^2 \tag{3.3}$$

For cross-correlation (X)FROG, the gating field is a reference field, and the expression is identical to Equation 3.1.

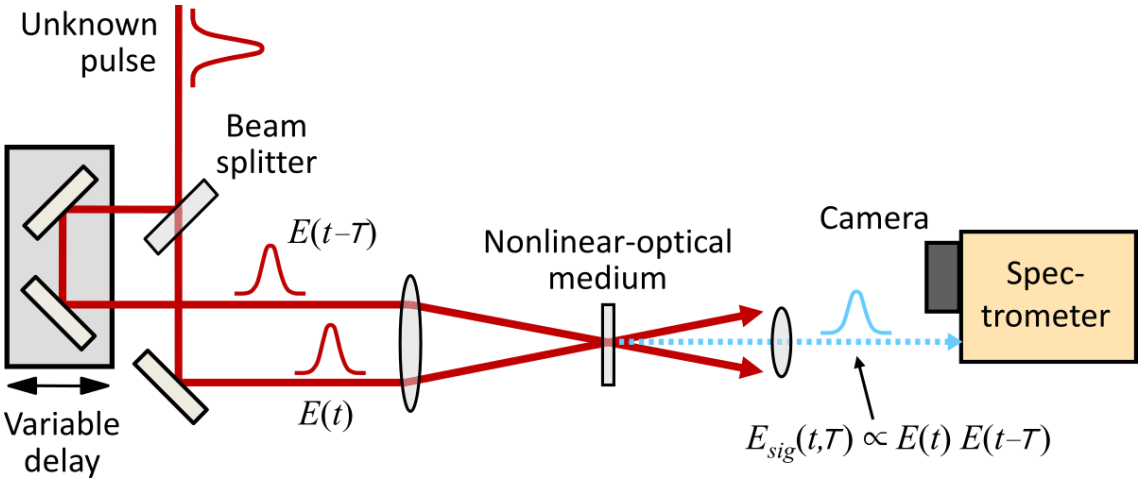

Figure 3.1: Example experimental diagram for SHG FROG. The gate is a delayed pulse replica. Instead of recording the energy as a function of delay, which is an autocorrelation, FROG records the spectrum as a function of delay.

FROG uses an iterative algorithm to retrieve the intensity and phase of the measured pulse. The algorithm searches for a single electric field that both matches the measured trace and matches the nonlinear interaction (as described in Eqn. 3.1, depending on the nonlinearity) [61]. Despite its complexity, the generalized projections algorithm for FROG has been demonstrated to be quite robust [62]. After the algorithm finishes, the retrieved trace is often compared against the measured trace.

FROG errors

It has become traditional to use the so-called G error – the RMS difference between the measured and retrieved traces across the entire trace–as the measure for how well the retrieved FROG trace matches the measured trace. Given a measured, normalized trace $I_{FROG}(\omega_i, T_j)$ and a retrieved trace $I_{FROG}^{(k)}(\omega_i, T_j)$, the G error is given by:

$$G = \sqrt{\frac{1}{N^2}\sum_{i,j=1}^{N}\left|I_{FROG}(\omega_i, T_j) - \mu I_{FROG}^{(k)}(\omega_i, T_j)\right|^2} \tag{3.4}$$

where μ is chosen to minimize G. This error metric normalizes by the number of points, N^2, and is appropriate for use within the FROG algorithm, and also when additive noise is the dominant source of noise in the trace, including the trace's edges. Because most FROG traces have more multiplicative noise than additive noise and hence large regions of near-zero values in their outer regions, the value of the G error that indicates good agreement varies with the size of the trace. It has been suggested by Scott *et. al.* [63] that, in most cases, a better way to normalize the error for human understanding would be to normalize by the energy in the measured trace. This error, named G', is given by:

$$G' = \sqrt{\frac{\sum_{i,j=1}^{N}\left|I_{FROG}(\omega_i,T_j) - \mu I_{FROG}^{(k)}(\omega_i,T_j)\right|^2}{\sum_{i,j=1}^{N}\left|I_{FROG}(\omega_i,T_j)\right|^2}} \tag{3.5}$$

Scott *et. al.* found that less than 5% G' error (or a G' error approximately equal to the known multiplicative noise in the measurement) was indicative of good agreement in most cases, and the simple nonrandom retrievals included in the top rows of Figs. 3.2-3.4 have well under 1% G' error. Both errors are used in this chapter, and FROG users are encouraged to consider the more intuitive G' error.

FROG characteristics

It should be mentioned that an important feature of all versions of FROG is that the measured trace contains more points than are strictly necessary to retrieve an answer, which can help safeguard against spurious measurement effects. As a result, there are simple consistency checks that can be calculated. Summing the trace over delay produces a frequency marginal which is related to the spectrum of the pulse [43]. Summing over frequency gives a delay marginal, which is typically related to an autocorrelation. These quantities are useful in ensuring that the measurement has been performed properly and the pulse has been retrieved from the measured trace correctly.

Also, simple agreement between the measured and retrieved traces is a general indicator of a high-quality measurement. Because FROG uses both time and frequency domains to determine pulse properties, in the case of instability it is likely to have discrepancies in both domains and between the measured and retrieved traces.

Simulations

FROG traces were computed using a sampling rate of 4 δt and 4 $\delta\omega$ to reduce the size of the traces and to be consistent with common experimental practice. The pulses were also cropped from the array size of 4096 to 1024, yielding a FROG trace size of 256x256. The XFROG measurement used a flat phase Gaussian reference pulse with a temporal FWHM of 43 δt. All FROG versions were simulated in the single-shot configuration, and the traces were averaged over all pulses in a train.

The maximum number of iterations of the FROG algorithm was limited to 1000. This limit is more than adequate for single pulses from the most complicated pulse train to converge on the first attempt. Experimental FROG traces are generally said to have converged if measured and retrieved traces have a G error of less than 0.01 (1%). Simulated traces without noise should be well under this limit if it is possible for the algorithm to converge. Regardless of convergence, the algorithm was run five times for each averaged measured trace, using different random noise for the initial condition each time, as suggested in Ref [62]. Because high RMS error is a strong indicator of measurement problems, and because non-convergence of the algorithm in such a pathological situation is a concern, the retrieved trace with the smallest error was chosen from the five results. In this way we hoped to capture the worst-case scenario for identifying unstable pulse trains, where the errors are small. By choosing the trace with the lowest error, we choose the trace that is most similar to the measured trace.

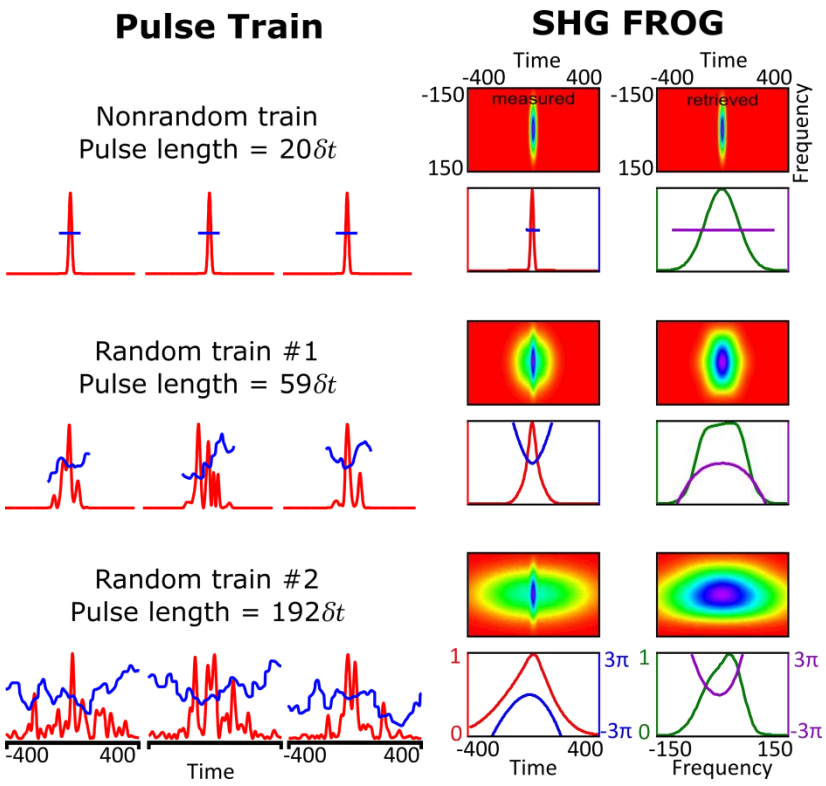

Figure 3.2: Simulated averaged SHG FROG measurements over random and nonrandom pulse trains [58]. Left column: example pulses. Right column: SHG FROG measurements and retrieved pulses. From the top row to the bottom row, the G errors are 0.0002, 0.014, and 0.02, and G' errors are 0.45%, 19%, and 19% respectively.

Second-Harmonic Generation FROG

The resulting measured SHG FROG traces (see Fig. 3.2) show a spike similar to autocorrelation's familiar coherent artifact in the center, with a broad, smooth background around it. The spike is very similar in size and shape to the SHG FROG trace of the stable, nonrandom pulse. The spike and the broad background with similar spectral width are both very consistent with how the pulse trains were constructed. Retrieved SHG FROG traces for the random trains show very clear differences from the measured traces. The retrieved traces are very smooth, lacking the structure observed in the measured traces. In particular, the coherent-artifact-like structure is missing from the retrieved traces.

The stable trace has a G error of 0.0002 and a G' error of 0.45%, indicating that the retrieval is in good agreement with the measured trace. In contrast, the averaged

measurement of the first random train has a G error of 0.014 and a G' error of 19%. Both the G error and the G' error are unacceptably large, especially for noiseless theoretical traces. Similarly, the averaged measurement of the second random train has a G error of 0.020 and a G' error of 19%. In combination with the obvious visual differences in trace structure, the large errors in the SHG FROG retrieval provide a very clear warning of pulse-train instability.

Considering the retrieved pulses, we find that SHG FROG retrieves pulses with FWHM lengths of 69 δt and 293 δt, overestimating the average FWHM lengths of the pulse trains, which are 59 δt and 192 δt respectively. The retrieved pulses are much simpler than the actual pulses. So while the retrieved pulses are in some respects representative of the pulse train, the complexity of the actual pulses is not reflected.

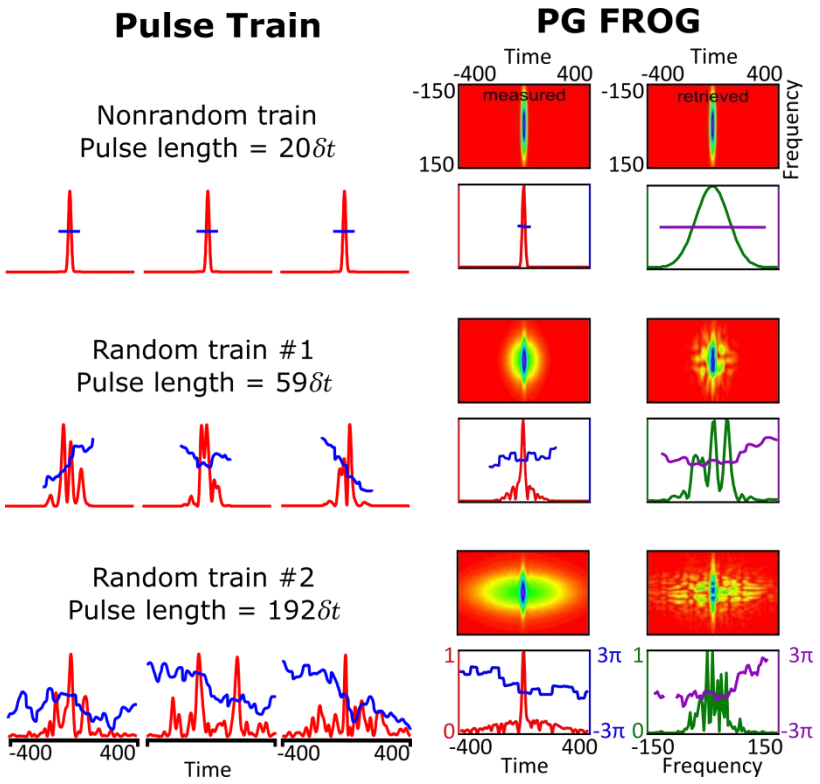

Figure 3.3: Simulated averaged PG FROG measurements over random and nonrandom pulse trains [58]. Left column: example pulses. Right column: PG FROG measurements and retrieved pulses. From the top row to the bottom row, the G errors are 0.0002, 0.016, and 0.03 and the G' errors 0.39%, 27%, and 41% respectively.

Polarization Gating FROG

Measured PG FROG traces (see Fig. 3.3) of random trains also show a coherent-artifact-like structure similar to the trace of the stable pulse. The background measured by PG FROG is less broad than the background measured by SHG FROG. Since the polarization gating signal depends on the field to the third power, it is less sensitive than other FROG geometries. Consequently, the background, which has a low average intensity, is less apparent. The retrieved traces still differ significantly from the measured traces, however. The retrieved traces are structured, despite the smooth appearance of the measured traces.

The trace agreement for the stable pulse is excellent, with a G error of 0.0002 and a G′ error of 0.39%, indicating a correct measurement. The discrepancies for the random trains are considerable. The retrieved trace for random train 1 has a G error of 0.016 and a G′ error of 27%. The retrieved trace for random train 2 has a G error of 0.030 and a G′ error of 41%. These errors are larger than the retrieved errors for unstable SHG FROG measurements, and are quite far from the acceptable error limits. This should come as no surprise, given that the retrieved traces for PG FROG look so different from the measured traces.

The pulses retrieved from the random train measurements have a large spike in the middle and low-intensity structure in the wings of the pulse. PG FROG therefore retrieves pulses with FWHM temporal widths much smaller than the actual FWHM pulse widths. The retrieved widths are 23 δt and 22 δt, while the actual average FWHM widths are 59 δt and 192 δt respectively. While the FWHM pulse estimates are less accurate than those retrieved by SHG FROG, the pulses retrieved by PG FROG show structure that is reminiscent of the actual measured pulses. So even though the FWHM length is less accurate, the pulse complexity is more representative.

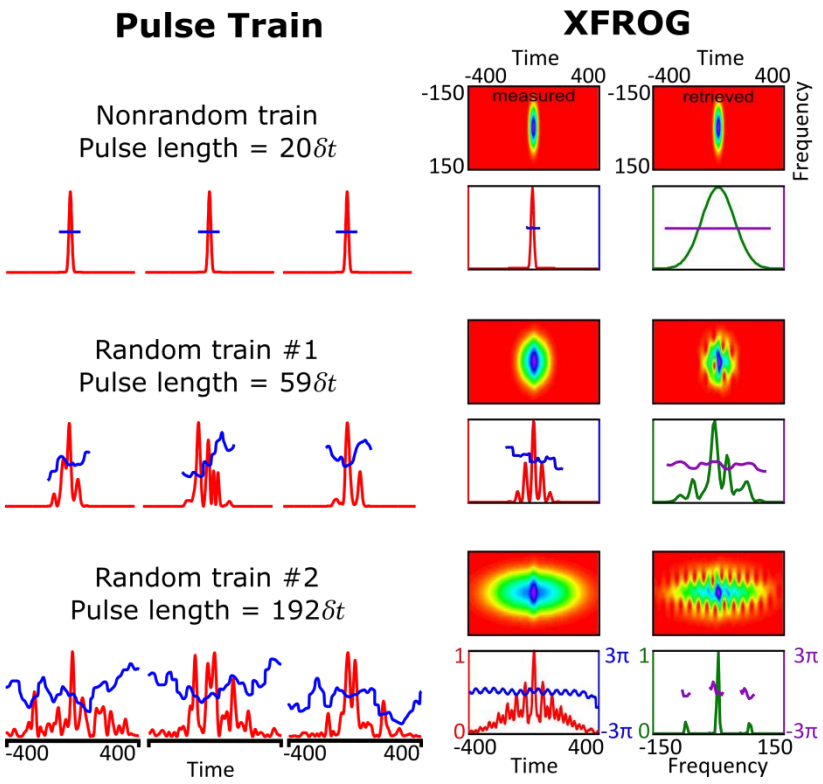

Figure 3.4: Simulated averaged XFROG measurements over random and nonrandom pulse trains [58]. Left column: example pulses. Right column: XFROG measurement and retrieved pulses. From the top row to the bottom row, the G errors are 0.0001, 0.026, and 0.041 and G' errors are 0.22%, 34%, and 34% respectively.

Cross-Correlation FROG (XFROG)

XFROG is most sensitive FROG geometry simulated here. Because the gating pulse is a reference pulse, the measurement is essentially linearly-dependent on the field we want to measure. Because of this, measured XFROG traces show the randomly-varying background more clearly than SHG or PG FROG traces (see Fig. 3.4). While the large-scale structure of the retrieved traces matches the measured traces, the retrieved XFROG traces of the random pulse trains have a great deal of structure that is not present in the measured traces.

The stable pulse is retrieved correctly, with a G error of 0.00001 and a G' error of 0.22%. The traces of random trains have very high errors. The first random train has a retrieved trace with a G error of 0.026 and a G' error of 34%, and the second random train has a retrieved trace with a G error of 0.041 and a G' error of 34%.

XFROG retrieves pulses that are very similar in complexity to actual pulses in the train. Examining the example pulses, we see that the retrieved pulses are a good representation of the random pulse trains. However, the FWHM temporal length of these pulses is much shorter than the average FWHM lengths of the trains. XFROG retrieves 21 δt and 120 δt as the FWHM, which is less than 59 δt and 192 δt respectively.

Discussion and Conclusions

SHG FROG has the smallest retrieved errors of the FROG techniques, consistent with having some trivial ambiguities not present in the other FROG techniques used. SHG FROG has an ambiguity in the direction of time, while PG FROG and XFROG do not. These techniques vary in their ability to represent the actual pulses in the train, but the retrieved pulses are always longer and more complicated than the stable component.

Because no single pulse exists that can possibly yield the measured FROG trace, the retrieval tends to stagnate and be sensitive to the initial guess. For the unstable trains, the algorithm was unable to converge on any attempt, and doubling the iteration limit to 2000 had little to no effect on the resulting RMS error. This strongly suggests that convergence is not possible for these traces.

Because the FROG algorithm has been demonstrated to be quite robust [62], significant disagreement between measured and retrieved traces should generally be attributed to instability or measurement error of some type, rather than non-convergence, as is occasionally speculated. In particular, the blotchy, structured appearance of the retrieved PG FROG and XFROG traces, contrasting with the smooth measured traces, is unlikely to result from anything but pulse-train instability. It appears that over-determination in the FROG trace is a significant advantage in the presence of instability. The clear differences in measured and retrieved traces for unstable trains, along with the common practice of publishing both of these traces, make it very difficult to mistake instability in a FROG measurement.

CHAPTER 4

THE COHERENT ARTIFACT IN SPECTRAL INTERFEROMETRY FOR DIRECT ELECTRIC FIELD RECONSTRCUTION

Spectral interferometry for direct electric field reconstruction (SPIDER) [64] is another popular ultrashort measurement technique. It encodes the group delay of a pulse onto spectral fringes so that the spectral phase can be measured. The spectral phase is extracted from the measured data by a very straightforward calculation, and so it is considered by some to be a much simpler technique. Unfortunately, unlike FROG, SPIDER provides essentially no feedback about the success of the measurement. Combined with the fact that interferometry very generally reacts poorly to variations, there is reason to be concerned with how SPIDER will react to unstable pulse trains. We find that large variations in pulse shape wash out of SPIDER measurements completely, and it can be difficult to distinguish a measurement of an unstable pulse train from a measurement of a stable pulse train.

Background on SPIDER

SPIDER is based on interfering two pulse replicas with slightly different center frequencies to determine the spectral phase of pulses. The difference in center frequency between the pulse replicas is referred to as the shear. Spectrally shearing one of the replicas means that the difference in spectral phase between two frequencies separated by the shear affects the interference fringes, allowing the phase to be reconstructed. In SPIDER, the pulse replicas have a relative delay, creating spectral fringes that are modulated by the difference in phase (see Fig. 4.1). The ideal SPIDER signal is:

$$S_{SPIDER} \propto |E(\omega) + E(\omega+\Omega)\exp(i\omega T)|^2$$
$$= S(\omega) + S(\omega+\Omega) + 2\sqrt{S(\omega)}\sqrt{S(\omega+\Omega)}\cos[\tau(\omega)\Omega + \omega T] \qquad (4.1)$$

Here $E(\omega)$ is the complex amplitude of the pulse electric field in terms of frequency, Ω is the spectral shear, T is the delay between the pulse replicas, $S(\omega)$ is the spectrum of the pulse, and $\tau(\omega)$ is the group delay of the pulse. To create this signal, two pulse replicas interact in a nonlinear crystal with different portions of a significantly chirped pulse. The difference in local frequency between these portions creates the spectral shear. Sum-frequency generation is the typical nonlinear interaction, but difference-frequency generation works equally well and may be preferable for some wavelengths.

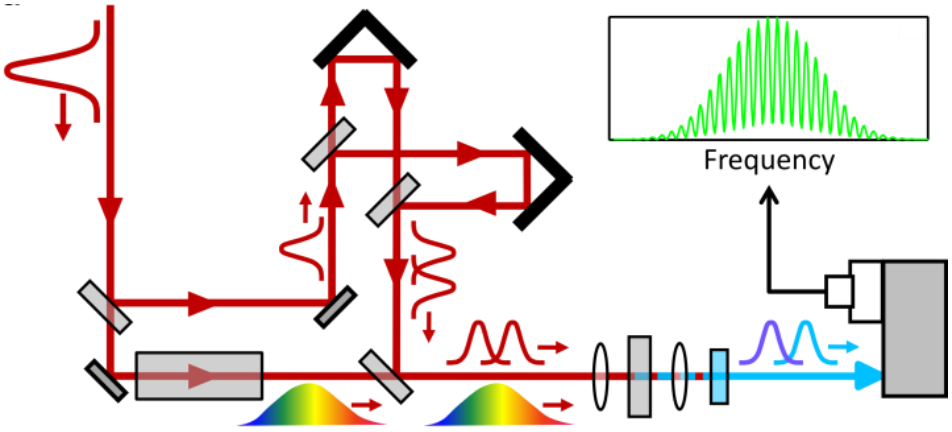

Figure 4.1: Basic schematic of SPIDER [65]. The delay lines necessary to maintain the correct relative delay between chirped and non-chirped pulses are omitted for simplicity. We show a dispersive medium being used to generate chirped pulses, but a prism or grating and a mirror may be used instead. Pulse replicas interact with the chirped pulse in a sum-frequency-generation crystal and are measured by a spectrometer after a filter removes the fundamental light. In a SPIDER measurement the relative delay between pulse replicas generates spectral fringes which are modulated by the local group delay.

Analytical Consideration of the Impact of Instability

In order to understand the potential impact of instability on SPIDER, we will perform some analytical calculations. In line with the pulse trains we have created, we will assume that the pulse train has a stable, consistent component $E(\omega)$ and a randomly varying component $E_{rand}(\omega)$. The expression for the ideal multi-shot SPIDER trace under these conditions is:

$$S_{SPIDER} \propto \langle |E(\omega) + E(\omega+\Omega)\exp(i\omega T) + E_{rand}(\omega) + E_{rand}(\omega+\Omega)\exp(i\omega T)|^2 \rangle \quad (4.2)$$

This expression contains several simplifying assumptions. Because the shear comes from stretching a pulse replica, it must be assumed that a stretched unstable pulse still has linear chirp. Further, the original pulse should be short enough to only overlap with a small portion of the stretched pulse, or the frequency shear will not be constant for all parts of the sheared pulse. Consideration of these effects complicates interpretation of the unstable signal too much to allow analytical progress, and so they will be ignored here. Multiplying out all the terms in Equation 4.2 yields:

$$\begin{aligned} S_{SPIDER} \propto \langle & |E(\omega)|^2 + |E(\omega+\Omega)|^2 + |E_{rand}(\omega)|^2 + |E_{rand}(\omega+\Omega)|^2 \\ & + 2Re\{E^*(\omega)E(\omega+\Omega)\exp(i\omega T) + E^*(\omega)E_{rand}(\omega) \\ & + E^*(\omega)E_{rand}(\omega+\delta\omega)\exp(i\omega T) + E^*(\omega+\delta\omega)\exp(i\omega T)\,E_{rand}(\omega) \\ & + E^*(\omega+\delta\omega)E_{rand}(\omega+\delta\omega) + E^*_{rand}(\omega)E_{rand}(\omega+\delta\omega)\exp(i\omega T)\}\rangle \end{aligned} \tag{4.3}$$

Now we make some arguments about the impact of instability to simplify this expression. Even if only the zeroth-order (constant) phase of the random pulse is allowed to vary, the random field will be positive as often as it is negative. Thus, any terms that have only one factor of the random field $E_{rand}(\omega)$ will sum to zero in the multi-shot average. All of the cross terms between the random and nonrandom components drop out, leaving:

$$\begin{aligned} S_{SPIDER} \propto \langle & |E(\omega)|^2 + |E(\omega+\Omega)|^2 + |E_{rand}(\omega)|^2 + |E_{rand}(\omega+\Omega)|^2 \\ & + 2Re\{E^*(\omega)E(\omega+\Omega)\exp(i\omega T) + E^*_{rand}(\omega)E_{rand}(\omega+\Omega)\exp(i\omega T)\}\rangle \end{aligned} \tag{4.4}$$

Now we will write this expression in terms of the spectra of the stable and random components, $S(\omega)$ and $S_{rand}(\omega)$, and their spectral phases, $\varphi(\omega)$ and $\varphi_{rand}(\omega)$, noting that the stable component has a constant spectrum and phase:

$$\begin{aligned} S_{SPIDER} \propto & S(\omega) + S(\omega+\Omega) + \langle S_{rand}(\omega)\rangle + \langle S_{rand}(\omega+\Omega)\rangle \\ & + 2\sqrt{S(\omega)}\sqrt{S(\omega+\Omega)}\cos[\varphi(\omega+\Omega) - \varphi(\omega) + \omega T] \\ & + 2\langle\sqrt{S_{rand}(\omega)}\sqrt{S_{rand}(\omega+\Omega)}\cos[\varphi_{rand}(\omega+\Omega) - \varphi_{rand}(\omega) + \omega T]\rangle \end{aligned} \tag{4.5}$$

Finally, we rewrite the expressions in the cosines in terms of the group delay as a function of frequency for each component, $\tau(\omega) = d\varphi/d\omega$ and $\tau_{rand}(\omega) = d\varphi_{rand}/d\omega$:

$$S_{SPIDER} \propto S(\omega) + S(\omega+\Omega) + \langle S_{rand}(\omega)\rangle + \langle S_{rand}(\omega+\Omega)\rangle + 2\sqrt{S(\omega)}\sqrt{S(\omega+\Omega)}\cos[\tau(\omega)\Omega + \omega T] + 2\langle\sqrt{S_{rand}(\omega)}\sqrt{S_{rand}(\omega+\Omega)}\cdot\cos[\tau_{rand}(\omega)\Omega + \omega T]\rangle \quad (4.6)$$

The net result is a sum of the spectra and sheared spectra, plus the well-known fringe term for the stable component and another for the random component. Equation 4.6 is the sum of the SPIDER traces of each pulse component alone. The random fringes are averaged over many shots, however. If $\tau_{rand}(\omega)$ is constant for a given pulse, but varies from pulse to pulse, corresponding to a random component with a variable arrival time, then the random fringe term will begin to wash out. If $\tau_{rand}(\omega)\Omega$ varies by as much as 2π in this way, then the fringes from the random component wash out completely. In this case, the only contribution of the random field to the SPIDER trace will be some background. Unfortunately, such a background can also be caused by misalignment and other ever-present and typically harmless effects, so, in practice, it is usually ignored. As a result, it is essentially impossible to distinguish the above harmless effects from the existence of a random component.

The impact of higher-order phase variations in the random component is not immediately clear, and this will be explored in the simulations. However, the above analytical calculations suggest that SPIDER may be unable to see some random variations in multi-shot measurements.

Simulation

SPIDER traces were computed using an array size of N = 4096 and pulse separation T of 450 δt. The frequency shear used was 9 $\delta\omega$, corresponding to 10% of the FHWM bandwidth of the trains. The SPIDER traces were computed using the ideal case

of Equation 4.1, because including any additional effects would make the traces more difficult to retrieve. The traces of all 5000 pulses in a train were averaged, and the spectral phase was retrieved using the Takeda algorithm typically employed in SPIDER [66].

In both of the measurements of random pulse trains, SPIDER yields only the nonrandom component, which is the coherent artifact (see Fig. 4.2). As expected from the analytic calculations, the fringe visibility is less than 100%, signifying that fringes have washed out due to variations. The measurement of random train 2 has much more background (80% background) than the measurement of random train 1 (13% background), which is also consistent with the calculations. The group delay is expected

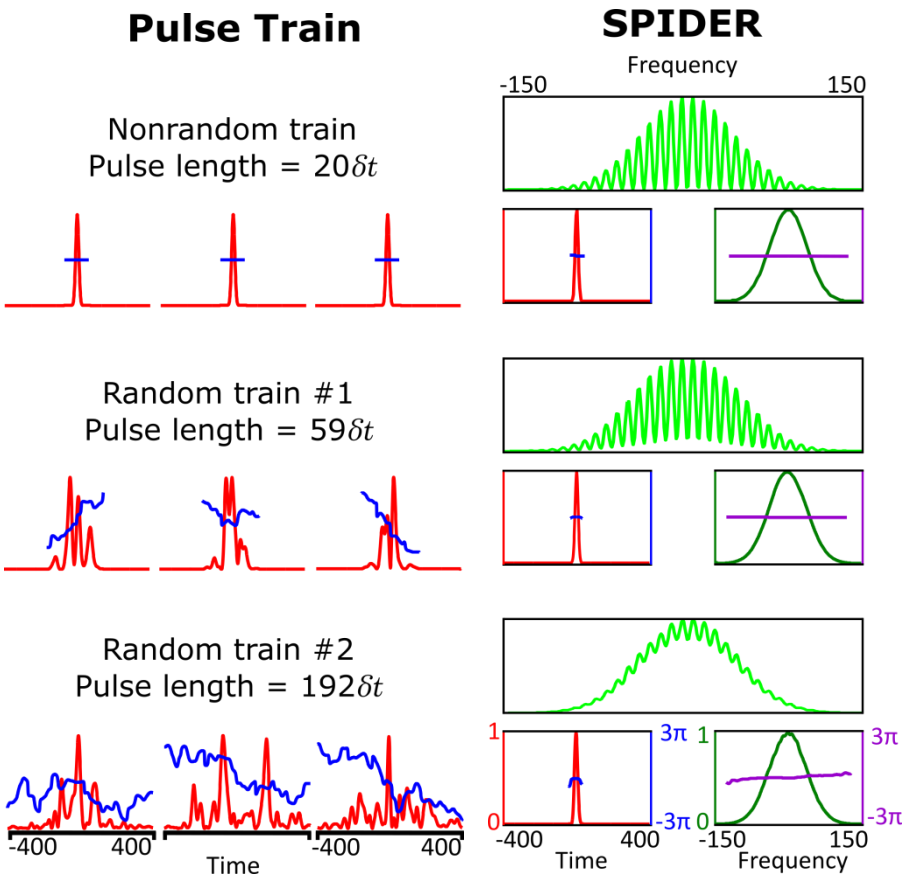

Figure 4.2: Simulated averaged SPIDER measurements of random and nonrandom trains [58]. SPIDER retrieves the nonrandom component only with decreasing fringe visibility: 100%, 87%, and 20% respectively.

to vary over a larger range from pulse to pulse in train 2, and the background should therefore be larger.

For train 1, higher order phase variations appear to cancel out of the SPIDER measurement while leaving very little background. Since the random pulse component contains a large percentage of the pulse energy for both random trains, the background would be much more prominent if the fringes from the unstable component washed out completely. Recalling from Equation 4.6 that we should be able to write these measured traces as the sum of the average traces of each pulse component, it becomes clear that the fringes from the unstable component have not washed out. This means that the averaged fringes from this random component are consistent with a flat spectral phase and a very short pulse. As a result, SPIDER misses a great deal of structure in the random trains.

The only difference between the measurement of the stable train and the measurement of random trains is the presence of background. Of course, background also occurs in SPIDER from a number of benign measurement effects. Any differences between the pulse replicas are likely to cause background. This includes differences in energy split, spatial overlap, and spatial mode-matching, as well as any damage spots or dust present in only one arm of the experimental setup. We conducted informal survey of published papers using SPIDER and found that the fringe visibility in real measurements rarely exceeded 80%.

To demonstrate that such effects can be indistinguishable from instability in the pulse train, a second SPIDER trace is fitted to the multi-shot traces (see Fig. 4.3). We assume that the pulse being measured is a flat-phase Gaussian pulse. The temporal pulse width of the Gaussian and the relative energy of the sheared and non-sheared pulses are allowed to vary. In all cases, the fit is in phase with the multi-shot trace, and will therefore give the same spectral phase.

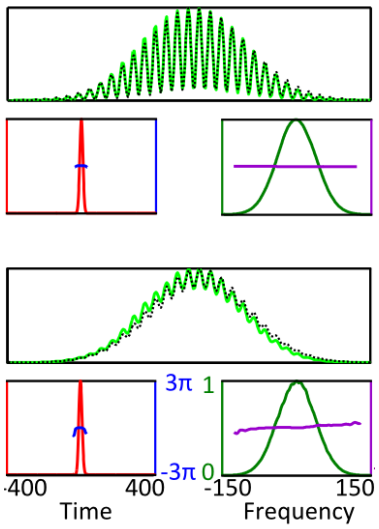

Figure 4.3: SPIDER traces of flat-phase pulses fitted to simulated measurements of unstable pulse trains [58]. The black dotted line indicates the fitted trace, which allows the pulse duration and the relative intensity between pulse replicas to vary.

Conclusions

SPIDER retrieves a coherent artifact in the presence of instability, ignoring all variations in the random pulses. Because the only difference between SPIDER measurements of stable and unstable pulse trains is background in the trace, it cannot effectively distinguish between a correct measurement of a stable pulse train and an incorrect measurement of an unstable pulse train. It is difficult to distinguish between background due to benign, practical effects in the lab and more serious instability. Very close to a 100% fringe visibility is necessary for a convincing estimate of the pulse length based on a SPIDER measurement. For example, a SPIDER fringe visibility of 87% (a better than average value) corresponds to a measured pulse length too short by a factor of approximately 3 (see Fig. 4.2). As a result, SPIDER traces with background cannot be trusted to accurately characterize an ultrashort pulse unless the stability of the pulse train has been convincingly guaranteed in some other fashion.

CHAPTER 5

UNSTABLE MULTIPULSING IN SPIDER AND SHG FROG

The pulse trains described in Chapter 2 correspond to only one of many possible types of instability. Multiple pulsing is possible in essentially all ultrafast laser systems at high pump powers. In this chapter, we will consider the impact of unstable multiple pulsing on SPIDER and SHG FROG, which are the two most commonly used pulse measurement techniques. We will perform calculations to inform our expectations of how these techniques will react and to help understand the results of the simulations.

Theory

Double Pulses in SPIDER

The previous chapter contains some analytical consideration of averaged SPIDER measurements, and we will expand upon those calculations for the specific case of unstable double pulses. Given a spectral shear Ω and delay T, a general expression for the SPIDER signal of a single pulse in terms of the electric field $E(\omega)$ is:

$$S_{SPIDER} \propto |E(\omega) + E(\omega+\Omega)\exp(i\omega T)|^2 = |E(\omega)|^2 + |E(\omega+\Omega)|^2 + 2|E(\omega)||E(\omega+\Omega)|\cos(\tau(\omega)\Omega + \omega T). \quad (5.1)$$

The spectral fringes depend on the group delay $\tau(\omega)$. To consider the impact of multiple pulsing, we consider two identical pulses with a relative phase θ and temporal separation t_s. The SPIDER trace of these pulses is then:

$$S_{SPIDER} \propto \left| \begin{matrix} E(\omega) + E(\omega+\Omega)\exp(i\omega T) + E(\omega)\exp(i\theta + i\omega t_s) \\ +E(\omega+\Omega)\exp(i\omega T)\exp(i\theta + i(\omega+\Omega)t_s) \end{matrix} \right|^2. \quad (5.2)$$

Considering identical pulses does limit the generality of this analysis to some degree, but it is helpful to eliminate other sources of variation in order to study the effects of varying

the separation and relative phase. Expanding Equation 5.2 and collecting terms results in a lengthy, yet tractable expression:

$$S_{SPIDER} \propto |E(\omega)|^2[1+\cos(\theta+\omega t_s)] + |E(\omega+\Omega)|^2[1+\cos(\theta+(\omega+\Omega)t_s)]$$
$$+|E(\omega)||E(\omega+\Omega)|\begin{Bmatrix}\cos(\tau(\omega)\Omega+\omega T)+\cos(\tau(\omega)\Omega+\omega T+\Omega t_s)\\ +\cos(\tau(\omega)\Omega+\omega(T+t_s)+\theta+\Omega t_s)\\ +\cos(\tau(\omega)\Omega+\omega(T-t_s)-\theta)\end{Bmatrix}. \quad (5.3)$$

The first two terms describe the overall intensity envelope of the SPIDER trace. The envelope shows the expected spectral modulations for a double pulse. The other four terms describe the interference fringes. The first two fringe terms represent the fringes that would be present in ordinary SPIDER measurements of each pulse alone. As in an ordinary SPIDER measurement, each pulse interferes with a sheared replica of itself. The second pair of fringe terms describes the spectral interference between each pulse and the sheared replica of the other pulse. These fringes have a different periodicity and depend on the relative phase between the two pulses.

If the relative phase θ between the pulses varies randomly over a range from 0 to 2π, then in the averaged measurement the spectral modulations even out and the last two fringe terms average to zero. In this case, the expression for the trace simplifies to:

$$S_{SPIDER} \propto |E(\omega)|^2 + |E(\omega+\Omega)|^2$$
$$+|E(\omega)||E(\omega+\Omega)|\{\cos(\tau(\omega)\Omega+\omega T)+\cos(\tau(\omega)\Omega+\omega T+\Omega t_s)\}. \quad (5.4)$$

Note that this expression is similar to, but slightly different from the general SPIDER expression given in Equation 5.1. Here we have two fringe terms contributing to the trace, differing by a factor of the shear times the pulse separation. The temporal range (or temporal support) of a SPIDER measurement is given by $2\pi/\Omega$, and therefore the factor Ωt_s is equivalent to 2π times the ratio of the pulse separation to the temporal support. Depending on the pulse and the measurement parameters, this ratio can be rather small. When the pulse separation is much smaller than the temporal support, the sum of these two fringe terms will be indistinguishable from a single fringe term. In addition, even if

these terms are significantly out of phase, their sum still varies at the same frequency (see Fig 5.1). SPIDER does not attempt to measure the absolute phase or arrival time of pulses, and therefore the absolute phase of the fringes in the trace is not a relevant quantity. Pulse separations of a significant fraction of the temporal support simply result in reduced fringe visibility due to partial cancellation. This means that if the relative phase of the two pulses is random, SPIDER will measure double pulses as a single pulse.

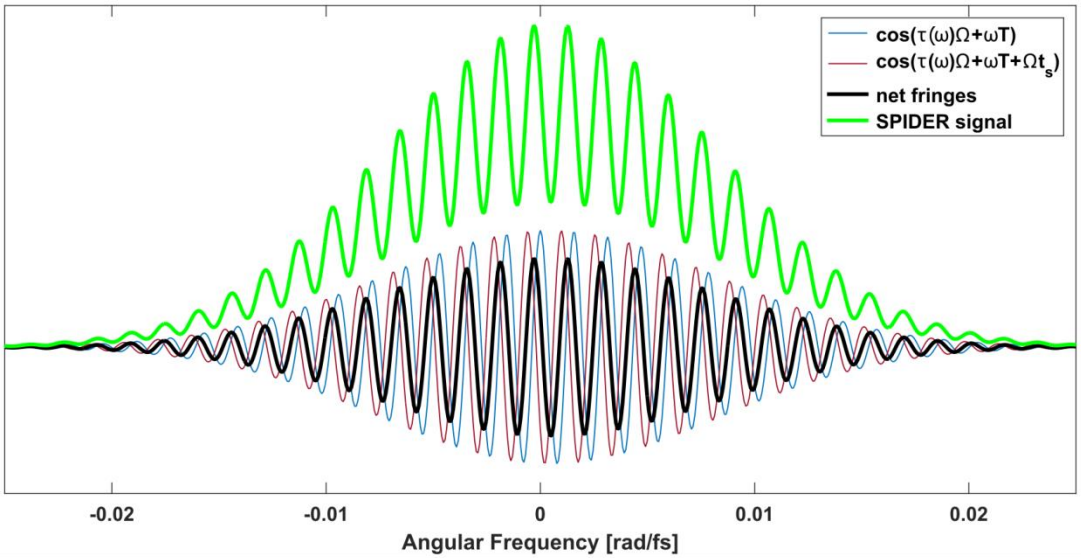

Figure 5.1: Fringe terms and SPIDER signal evaluated for an equal-energy double pulse with stable pulse separation, averaged over relative phases from 0 to 2π. The last two fringe terms in Equation 3 average to zero and are not plotted. The pulse separation and shear are chosen such that $\Omega t_s = 3\pi/4$. Because the two fringe terms are not in phase, there is some cancellation in their sum and the trace shows some background.

Cases in which the relative phase does not vary over the full range are much more difficult to understand analytically, as they required all the terms found in Equation 5.3. Also, the impact of variations in the pulse separation is not particularly clear. If the pulse separation varies over a large enough range that Ωt_s varies by 2π then several of the fringe terms in Equation 5.3 will vanish, but the last term will remain in some form.

Double Pulses in SHG FROG

Analytic analysis of FROG is frequently unfeasible because of the complexity of self-referenced spectrograms. However, assuming that the two pulses under consideration are flat-phase Gaussian pulses allows such a calculation to be performed for this case. While this assumption is of course quite restrictive, the simulations we present in this paper will also use flat-phase Gaussian pulses, and the calculation is still informative about other cases. If the electric field of a Gaussian double pulse in the time domain is

$$E(t) = \exp(-t^2/\sigma_t^2) + \exp(-(t+t_s)^2/\sigma_t^2 + i\theta) \tag{5.5}$$

then the corresponding SHG FROG measurement is:

$$I_{SHG\ FROG}(\omega,\tau) = \left|\int_{-\infty}^{\infty} E(t)E(t-\tau)\exp(-i\omega t)\,dt\right|^2 = \tag{5.6}$$

$$\left|\int \left[\exp\left(\frac{-t^2}{\sigma_t^2}\right) + \exp\left(\frac{-(t+t_s)^2}{\sigma_t^2}\right)\right]\left[\exp\left(\frac{-(t-\tau)^2}{\sigma_t^2}\right) + \exp\left(\frac{-(t+t_s-\tau)^2}{\sigma_t^2}\right)\right]\exp(-i\omega t)\,dt\right|^2 \tag{5.7}$$

where τ is the delay. Some tedious calculations eventually reduce this expression to:

$$I_{SHG\ FROG}(\omega,\tau) \propto$$

$$\exp\left(\frac{-\tau^2}{\sigma_t^2}\right)\exp\left(\frac{-\omega^2\sigma_t^2}{4}\right)\left[\begin{array}{c}\cos^2\left(\frac{\omega t_s}{2}+\theta\right) + 2\cos\left(\frac{\omega t_s}{2}+\theta\right)\exp\left(\frac{-t_s^2}{2\sigma_t^2}\right)\cosh\frac{t_s\tau}{\sigma_t^2} \\ +2\exp\left(\frac{-t_s^2}{\sigma_t^2}\right) + \exp\left(\frac{-t_s^2}{\sigma_t^2}\right)\cosh\frac{2t_s\tau}{\sigma_t^2}\end{array}\right] \tag{5.8}$$

The second and third terms turn out to be vanishingly small, and the last term can be broken into a more intuitive form, resulting in a more natural expression:

$$I_{SHG\ FROG}(\omega,\tau) \propto \exp\left(\frac{-\tau^2}{\sigma_t^2}\right)\exp\left(\frac{-\omega^2\sigma_t^2}{4}\right)\cos^2\left(\frac{\omega t_s}{2}+\theta\right) +$$

$$\frac{1}{2}\exp\left(\frac{-\omega^2\sigma_t^2}{4}\right)\left[\exp\left(\frac{-(\tau-t_s)^2}{\sigma_t^2}\right) + \exp\left(\frac{-(\tau+t_s)^2}{\sigma_t^2}\right)\right] \tag{5.9}$$

This is the typical double-pulse SHG FROG trace. The delay and frequency envelopes are equal to the trace of a simple Gaussian pulse. There are three lobes in this spectrogram, appearing at $\tau = 0$ and $\tau = \pm t_s$ respectively. The middle lobe is modulated with fringes that depend on the pulse separation and relative phase. The side lobes are lower in intensity, but share the same widths as the center lobe.

Varying the relative phase θ over the full range causes the fringes in the middle lobe to be erased. The resulting simple trace with three smooth lobes is not a valid spectrogram for any electric field. Temporally space lobes in the trace dictate that the field must have satellite pulses, but satellite pulses always cause the spectrum to be modulated. Integrating the trace over delay yields a smooth spectral profile, which must be equal to the autoconvolution of the spectrum. The pulse spectrum cannot be modulated and have a smooth autoconvolution. So the averaged trace requires the pulse spectrum to be both smooth and modulated, and cannot be satisfied with any single electric field.

Varying the pulse separation changes the position of the side lobes and the periodicity of the fringes in the center lobe. Averaging over a variety of separations results in temporally wider, less intense side lobes in the aggregate trace. The response of the FROG retrieval algorithm is not easy to predict and is best explored by simulations.

Simulations will seek to confirm the calculations presented in this section and show how the FROG algorithm responds to traces created by unstable double pulses. Simulations also have the ability to investigate cases involving small relative phase variations or couplings between pulse separation and relative phase.

Simulations of Unstable Double Pulses

These simulations average over sets of 5000 pulses, calculating the ideal signal for each pulse as given by Equation 5.1 for SPIDER and Equation 5.6 for SHG FROG. We define flat-phase Gaussian pulses with a temporal FWHM of 150 fs on a temporal grid of 4096 points spaced by 20 fs. The corresponding spectral resolution is 0.077 rad/ps. For SPIDER parameters, we choose the delay to be 4ps and the shear to be 12 frequency steps or 0.9 rad/ps. The temporal support is consequently 6.8 ps. FROG traces are cropped and sampled to reduce the number of points to 512x512. This trace size is fairly large, and therefore the associated G errors normalized by the number of points will be smaller than is typically expected.

In all cases, the two pulses have equal energy. We include one set of pulses where only the relative phase varies, and a second set of pulses where both the separation and the relative phase vary. For each case, we include a plot of the averaged autocorrelation, the average spectrum, and a polar plot of the temporal pulse separation as a function of relative phase.

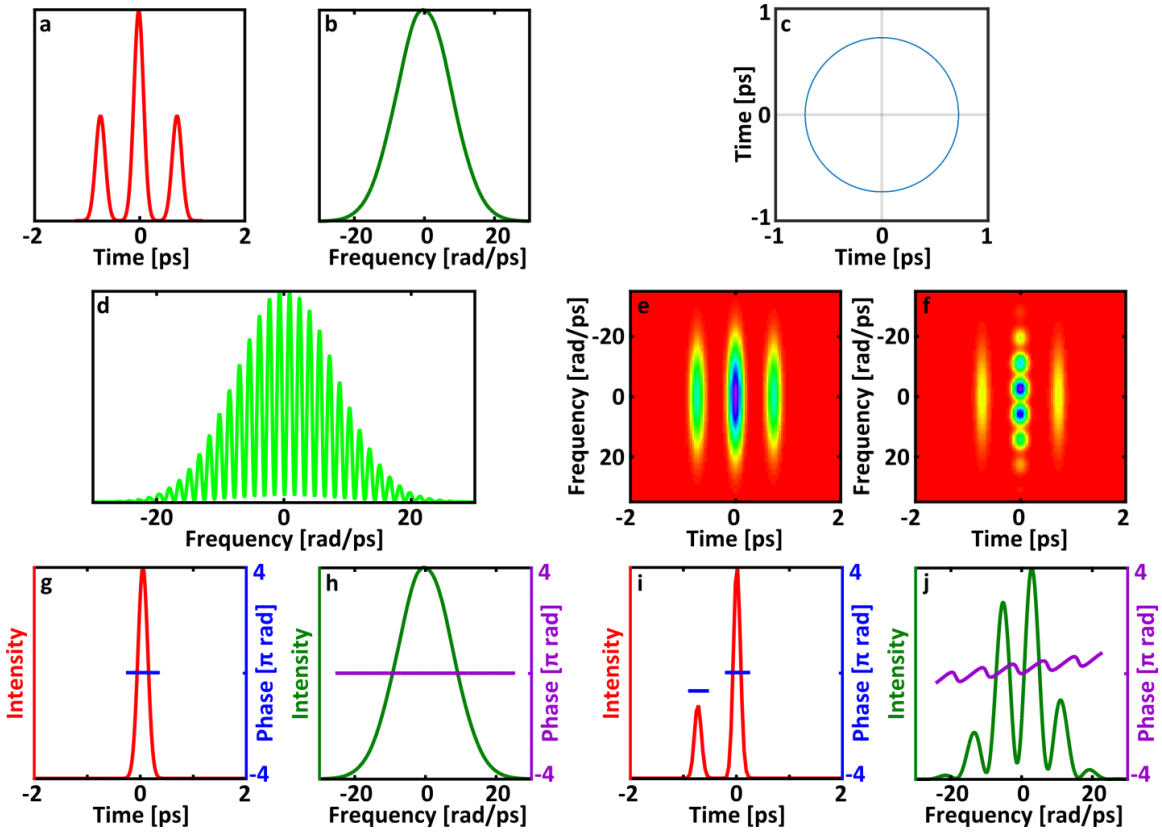

Figure 5.2: SPIDER and FROG measurements of a train of double pulses with stable separation and varying relative phase. (a) The average autocorrelation. (b) Average spectrum of the double pulse train. (c) Polar plot of the pulse separation as a function of relative phase. (d) Average SPIDER measurement of the whole pulse train (e) Average FROG measurement of the whole pulse train (f) Retrieved FROG trace with G error 0.0140. (g) Temporal intensity (red) and phase (blue) of the pulse retrieved by SPIDER (h) Spectral intensity (green) and phase (purple) of the pulse retrieved by SPIDER (i) Temporal intensity (red) and phase (blue) of the pulse retrieved by FROG (j) Spectral intensity (green) and phase (purple) of the pulse retrieved by FROG.

Phase Variation Only

For the first case, where only the relative phase varies, the pulse separation is set to 720fs. The autocorrelation is identical to the autocorrelation of a single pulse (see Fig

5.2a) and the plot of the separation vs phase is a circle (see Fig 5.2c). The relative phase variations result in an average spectrum that is nearly Gaussian (Fig 5.2b). The average SPIDER trace (Fig 5.2d) shows essentially no background. This is expected, because the pulse separation chosen is a very small fraction of the temporal support. The fringes in the trace correspond to a flat spectral phase (Fig 5.2h), and the satellite pulse is consequently invisible (Fig 5.2g). The measured FROG trace (Fig 5.2e) has the predicted structure of three smooth lobes. The retrieved trace (Fig 5.2f) is visually different from the measured trace, with lower-intensity side lobes and fringes in the main lobe. The G error between measured and retrieved traces is 0.014. The retrieved pulse (Fig 5.2i) does have a satellite at the correct delay, although the intensity of the satellite is much lower than in the actual pulse train.

Phase Variation and Separation Variation

For the second case with variations in both relative phase and temporal pulse separation, the pulse separation was allowed to vary uniformly from 640 fs to 800 fs. The separation vs phase plot is a more diffuse circle of varying radius (see Fig 5.3). The average autocorrelation is surprisingly similar to a single-pulse autocorrelation (an autocorrelation of a single pulse with an average separation is shown in black in Fig 5.3a). The side lobes in the autocorrelation are slightly broadened and their height is slightly reduced. Similarly to the first case, the relative phase variations cause the average spectrum to be close to Gaussian.

The average SPIDER trace is also very similar, showing little difference from average trace in the previous case. The SPIDER measurement again fails to see the satellite pulse in the averaged measurement. The averaged measured FROG trace shows slight broadening of the side lobes, similarly to the autocorrelation. The retrieved FROG trace is visually quite different from the measured trace, showing an additional pair of

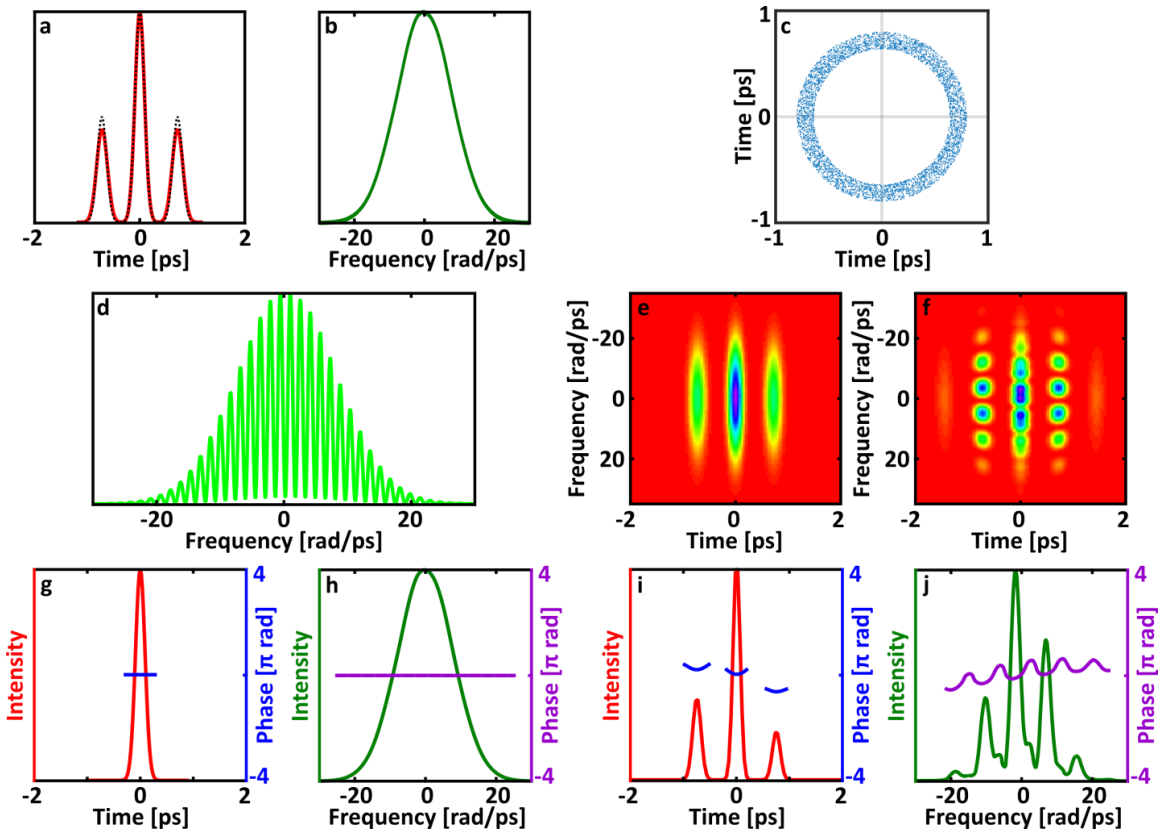

Figure 5.3: SPIDER and FROG measurements of a train of unstable double pulses with varying separation and relative phase. (a) The average autocorrelation is shown in red, and the black dotted line shows the autocorrelation of a pulse with an average separation. (b) Average spectrum of the double pulse train. (c) Polar plot of the pulse separation as a function of relative phase. (d) Average SPIDER measurement of the whole pulse train (e) Average FROG measurement of the whole pulse train (f) Retrieved FROG trace with G error 0.0124. (g) Temporal intensity (red) and phase (blue) of the pulse retrieved by SPIDER (h) Spectral intensity (green) and phase (purple) of the pulse retrieved by SPIDER (i) Temporal intensity (red) and phase (blue) of the pulse retrieved by FROG (j) Spectral intensity (green) and phase (purple) of the pulse retrieved by FROG.

side lobes indicative of a third pulse. The G error is 0.0124. Both satellite pulses retrieved are much less intense than the actual satellite pulses. The temporal separations of the two satellites from the main pulse are each equal to the average separation in the pulse train (720 fs). The retrieved pulses are slightly chirped and have phases of approximately $\pi/6$, 0, and $-2\pi/3$ respectively.

When Phase and Separation are Coupled

While many researchers of unstable multipulsing do not explicitly discuss relative phase, some simulations show that the phase and the separation between pulses can be related in interesting ways in some cases [67]. Based on these observations, we include a third test case where the phase varies over a range less than 2π and the pulse separation follows an interesting path as the phase changes (see Fig 5.4c). The maximum temporal

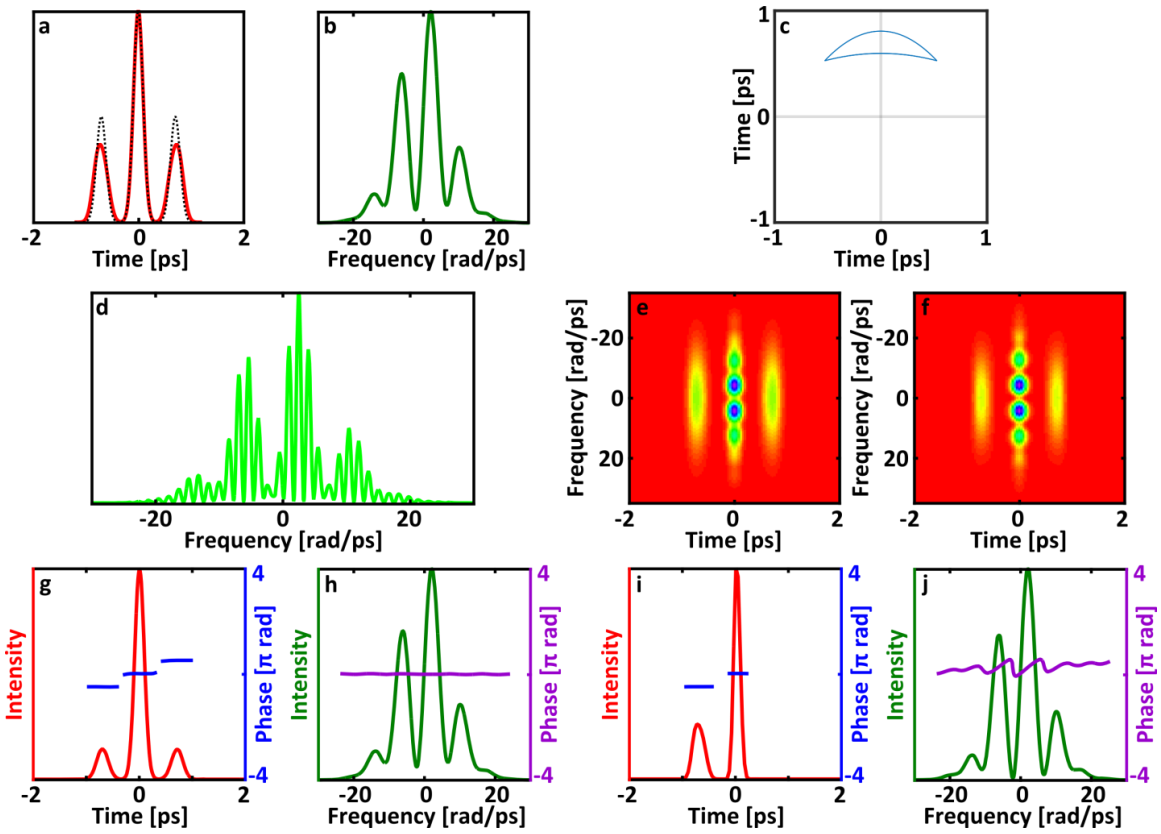

Figure 5.4. SPIDER and FROG measurements of a train of unstable double pulses with varying separation and relative phase. (a) The average autocorrelation is shown in red, and the black dotted line shows the autocorrelation of a pulse with an average separation. (b) Average spectrum of the double pulse train. (c) Polar plot of the pulse separation as a function of relative phase. (d) Average SPIDER measurement of the whole pulse train (e) Average FROG measurement of the whole pulse train (f) Retrieved FROG trace with G error 0.0016. (g) Temporal intensity (red) and phase (blue) of the pulse retrieved by SPIDER (h) Spectral intensity (green) and phase (purple) of the pulse retrieved by SPIDER (i) Temporal intensity (red) and phase (blue) of the pulse retrieved by FROG (j) Spectral intensity (green) and phase (purple) of the pulse retrieved by FROG.

separation is 800 fs and the minimum separation is 590 fs. The relative phase varies from $\pi/4$ to $3\pi/4$. The larger range of separations causes the side lobes in this autocorrelation to be wider and shorter than in the autocorrelation for the second case. The small range of relative phases results in a spectrum that is quite modulated.

The average SPIDER trace of this pulse train is also heavily modulated, although the spectral phase retrieved from it is nearly flat. The retrieved temporal pulse shape includes very small satellite pulses with relative phases of $-\pi/2$ and $\pi/2$ at the average delay of 700 fs. The measured FROG trace shows some blurring of the fringes in the central lobe and more diffuse side lobes. The retrieved trace is much more similar to the measured trace than in previous cases, although there are still discrepancies. The retrieved temporal pulse has a low intensity satellite with a temporal separation of about 700 fs and relative phase of $-\pi/2$. Interestingly, this satellite pulse does not have the same temporal width as the main pulse. It is significantly wider, with a FWHM width of about 250 fs. This is also apparent from the spectrum, which has better fringe visibility in the center than at the edges. Despite the longer satellite pulse, the side lobes in the retrieved trace are still not as wide as the side lobes in the measured trace.

Conclusions

Based on the simulations and calculations presented here, we find that SPIDER does not see satellite pulses when the relative phase of the satellite pulse varies over 0 to 2π. This is true regardless of whether the temporal separation of the two pulses varies. In addition, smaller variations in spectral phase cause SPIDER to significantly underestimate the intensity of satellites. Since these compromised traces are indistinguishable from normal, correct SPIDER traces, it will be very difficult to know when a random satellite may be present. This means that SPIDER is not capable of guaranteeing that the output of a given laser is stable using an averaged measurement.

SHG FROG also consistently underestimates the intensity of satellite pulses. Retrieved satellites correctly represent the average pulse separation when the pulse separation varies. Retrieved traces have structural differences from measured traces when the pulse train is unstable, and their rms error is slightly larger than what is expected for quality measurements, especially in the absence of noise. Careful study of measured and retrieved traces can give hints about the nature of the measured pulses.

CHAPTER 6

THE COHERENT ARTIFACT IN TWO-DIMENSIONAL SPECTRAL SHEARING INTERFEROMETRY

Two-dimensional spectral shearing interferometry (2DSI) is based on SPIDER and was designed to address some potential issues with that technique [68]. Retrieving the correct spectral phase with SPIDER depends on good calibration of the delay between the pulse replicas [69]. While this is not a fatal flaw, 2DSI aims to dodge this concern completely by removing this delay. Unfortunately, the modifications introduced by 2DSI are unlikely to greatly improve its response to unstable pulse trains. In addition to confirming that 2DSI measures a coherent artifact, we explore the effects of simulating a less idealistic version of the 2DSI equations and demonstrated the role of the frequency shear in unstable measurements. We also simulate measurements over only a few unstable pulses, to demonstrate that any amount of averaging can be problematic.

Differences between 2DSI and SPIDER

2DSI and SPIDER are both based on interfering pulse replicas with slightly different center frequencies to determine the spectral phase of pulses. 2DSI differs from SPIDER in that it uses pulse replicas that overlap exactly in time, but have a small relative phase offset in addition to the frequency shear (see Fig. 6.1). This is accomplished by allowing a single pulse replica to interact with different portions of two significantly chirped pulses. The delay between the chirped pulses sets the spectral shear. A phase offset between the resulting higher-frequency pulse replicas is created by varying the delay between the quasi-CW beams very slightly. Scanning the phase offset through several electric field cycles and recording the resulting spectrum at each delay

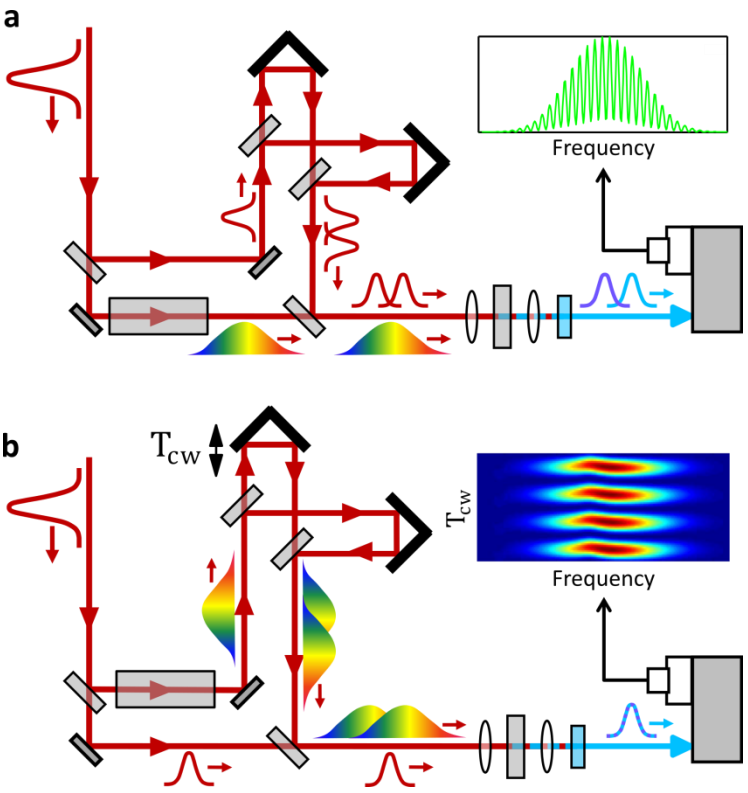

Figure 6.1: Basic schematic of (a) SPIDER, for reference; and (b) 2DSI. The delay lines necessary to maintain the correct relative delay between chirped and non-chirped pulses are omitted for simplicity. We show a dispersive medium being used to generate chirped pulses, but a prism or grating and a mirror may be used instead. Pulse replicas interact in a sum-frequency-generation crystal and are measured by a spectrometer after a filter removes the fundamental light. In a SPIDER measurement the relative delay between pulse replicas generates spectral fringes which are modulated by the local group delay. In a 2DSI measurement, interferometrically scanning the delay between chirped pulse replicas creates fringes in the delay direction which are similarly modulated by the local group delay.

produces a two-dimensional plot with several visible fringes in the delay direction. An expression for the ideal 2DSI signal is:

$$S_{2DSI}(\omega,\tau_{cw}) = S(\omega) + S(\omega-\Omega) + 2\sqrt{S(\omega)S(\omega-\Omega)}\cos[\omega T_{cw} + \varphi(\omega) - \varphi(\omega-\Omega)] \quad (6.1)$$

where T_{cw} is the phase offset. As in SPIDER, one can make the approximation that the phase difference in the cosine term is approximately the group delay (the derivative of the phase) times the shear, or:

$$S_{2DSI}(\omega,\tau_{cw}) \approx S(\omega) + S(\omega-\Omega) + 2\sqrt{S(\omega)S(\omega-\Omega)}\cos[\omega T_{cw} + \tau(\omega)\Omega] \quad (6.2)$$

where $\tau(\omega)$ is the group delay. The fringe at each frequency will be offset according to the group delay at that frequency. Consequently, the group delay can be obtained by Fourier transforming the signal along the phase/delay direction and taking the phase of either AC sideband. The group delay can then be integrated to determine the spectral phase as in SPIDER.

Previous chapters have demonstrated that the effect of pulse-shape instability on a SPIDER measurement is to reduce the fringe visibility. This occurs due to variations in the group delay. The group-delay term in Eq. (5.2) controls the offset of the sinusoidal fringe pattern at each frequency. If the group delay changes, the fringes move. Thus, averaging over many pulses with different group delays means that the fringes begin to wash out, resulting in lower peaks and higher troughs. The equations describing 2DSI are so similar to the equations describing SPIDER that there is little reason to expect it to react differently to instability. Consequently, we expect variations to wash out of the measurement, leaving background in the 2DSI traces.

An interesting feature of the 2DSI setup compared to the traditional SPIDER setup is that the spectral shear is a free parameter. In SPIDER, the spectral shear is coupled to the delay between the pulses. This means that in 2DSI it is more reasonable to adjust the shear between measurements. Since the spectral shear scales how much the group delay displaces the fringes (see Eqn. 5.2), it has the potential to have an interesting impact on unstable measurements. We will accordingly simulate 2DSI measurements with two different spectral shears. There are several other SPIDER variants besides 2DSI that are able to easily adjust the spectral shear. In particular, in the absence of spatiotemporal distortions, SEA SPIDER [70] traces are essentially equivalent to the 2DSI traces shown in this chapter, and the discussion presented in this chapter will also apply directly to that technique.

Implementing More Realistic Averaging

In the typical equations for SPIDER and 2DSI given here, the stretched pulses used in the measurement are assumed to be essentially continuous-wave beams of the desired frequency. This assumption is reasonable for measuring short pulses with fairly flat spectral phases. In the general case, however, considering sum-frequency generation with stretched pulses instead of CW beams significantly complicates the mathematics involved. These effects may very well be important, especially when considering averaging over many different pulses. The simplest correction to the above equations is to consider the impact of a difference in phase between different colors in the pulse.

Generally speaking, a pulse's spectral phase is not flat and any two frequencies will have a non-zero phase difference. When the pulse is stretched, these two colors will retain their original phase difference in addition to any phase difference caused by chirping. Even if we assume that the chirp is symmetrical, such that it does not introduce any additional relative phase, the pulse replicas will still inherit the relative spectral phase of the two up-converting frequencies. If the spectral phase varies from pulse to pulse, then the relative phase of the pulse replicas will vary as well. The effect of these variations is to introduce an additional shift the fringes from shot to shot. We expect this to further decrease the fringe visibility in simulated unstable-train measurements, in addition to the reduction in fringe visibility already expected from group-delay variations.

Simulation Details

A 2DSI measurement of each pulse train was simulated for two different frequency shears. The larger shear ($9\delta\omega$) corresponds to 10% of the full width at half maximum (FWHM) bandwidth of the pulses, identical to the shear used in the SPIDER simulations. The smaller shear ($4\delta\omega$) corresponds to 4% of the FWHM bandwidth. The simulated traces were created with 16 delay increments per electric field cycle, with 4 full cycles. Although 2DSI is an inherently multi-shot technique, the averaged measurement

is simulated with each pulse contributing to the signal at each delay. We treat the measurement as an ergodic process in which averaging over time is equivalent to averaging the whole trace over a large number of pulses. This is consistent with typical oscillator repetition rates compared to delay stage scan rates. However, if very few pulses are used to generate signal at each delay or if there is some systematic drift in the laser source, then it is possible that the trace may not be periodic with respect to phase offset. If this happens, it is a very clear indicator of pulse-shape instability.

To explore how important the approximations are, we have simulated these 2DSI measurements both using a CW-beam type simulation (where the spectral phase does not

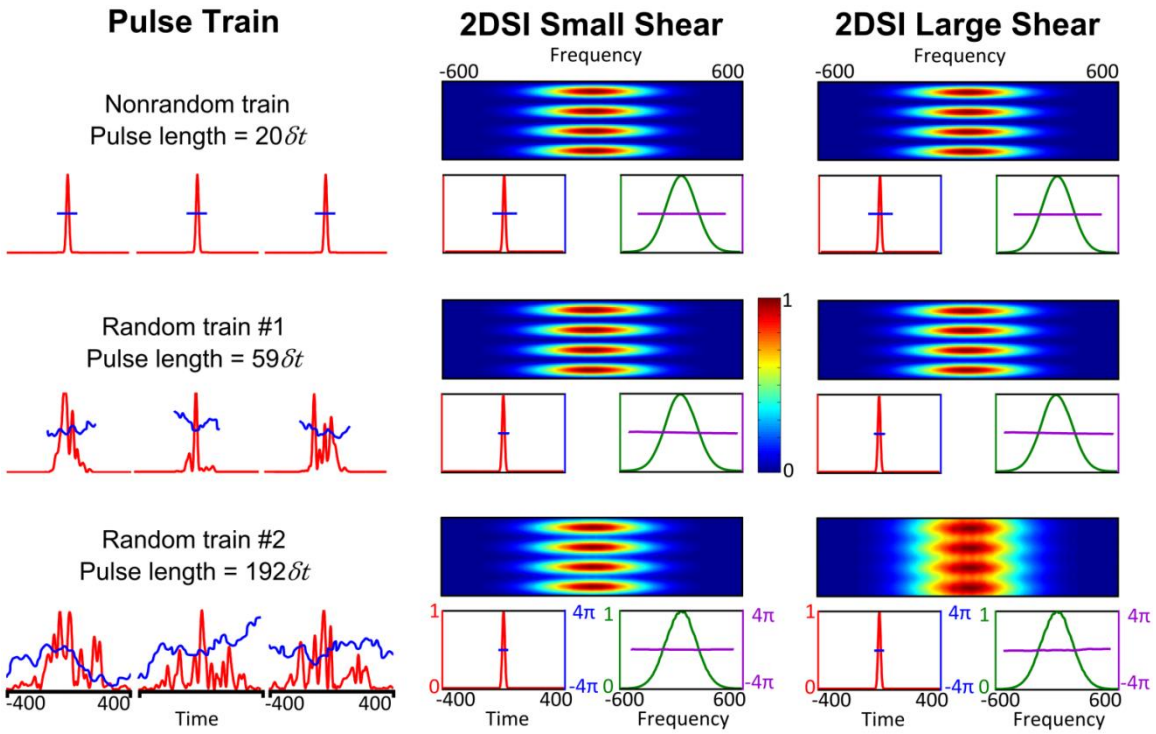

Figure 6.2: Coherent artifact simulation for 2DSI using CW beams [65]. (Red is temporal intensity, blue is temporal phase, dark green is spectral intensity, and purple is spectral phase). Measurements in the middle column use a small frequency shear: 4% of the FWHM pulse bandwidth. The fringe visibility is 98% for the 59 δt train and 78% for the 192 δt train (backgrounds of 2% and 22% respectively). Measurements in the right column use a larger frequency shear: 10% of the FWHM pulse bandwidth. The fringe visibility is 90% for the 59 δt train and 23% for the 192 δt train (backgrounds of 10% and 77% respectively).

affect the up-converting beams) and with the small correction that includes the relative phase of the up-converting frequencies.

Simulation Results and Discussion

The simulated measurements of the pulse trains using 2DSI without the relative phase correction are shown in Figure 6.2. Notice that all of the simulated measurements yield a flat spectral phase, which is the frequency-domain equivalent of the coherent artifact. Applying this flat phase to the separately measured average spectrum yields a pulse with the same temporal width as the stable component of the pulse train. This means that 2DSI measures only the stable component of an unstable pulse train—the coherent artifact. The measurement result does not reflect any of the variations between the pulses.

The one clear difference between the measurements of the unstable trains and the measurement of the stable train is the difference in fringe visibility. There is appreciable background in the measurements of the longer unstable pulse train, which is very obvious when using a large shear. The reason for larger shears yielding worse fringe visibility is apparent from Eq. (6.2): the fringes are shifted by an amount equal to the group delay multiplied by the spectral shear. Variations in the group delay due to pulse-shape instability cause the fringes to change position from shot to shot. The larger shear causes more fringe movement and therefore worse fringe visibility. This also explains why the fringe visibility is worse for the more complicated pulse train. This train has more, larger variations in the group delay, also causing more fringe displacement.

Results of More Realistic Simulation

All of the general trends in the simpler simulation results are repeated for the simulations with the relative-phase correction, shown in Figure 6.3. As expected, the backgrounds are generally larger and the fringe visibility is generally worse.

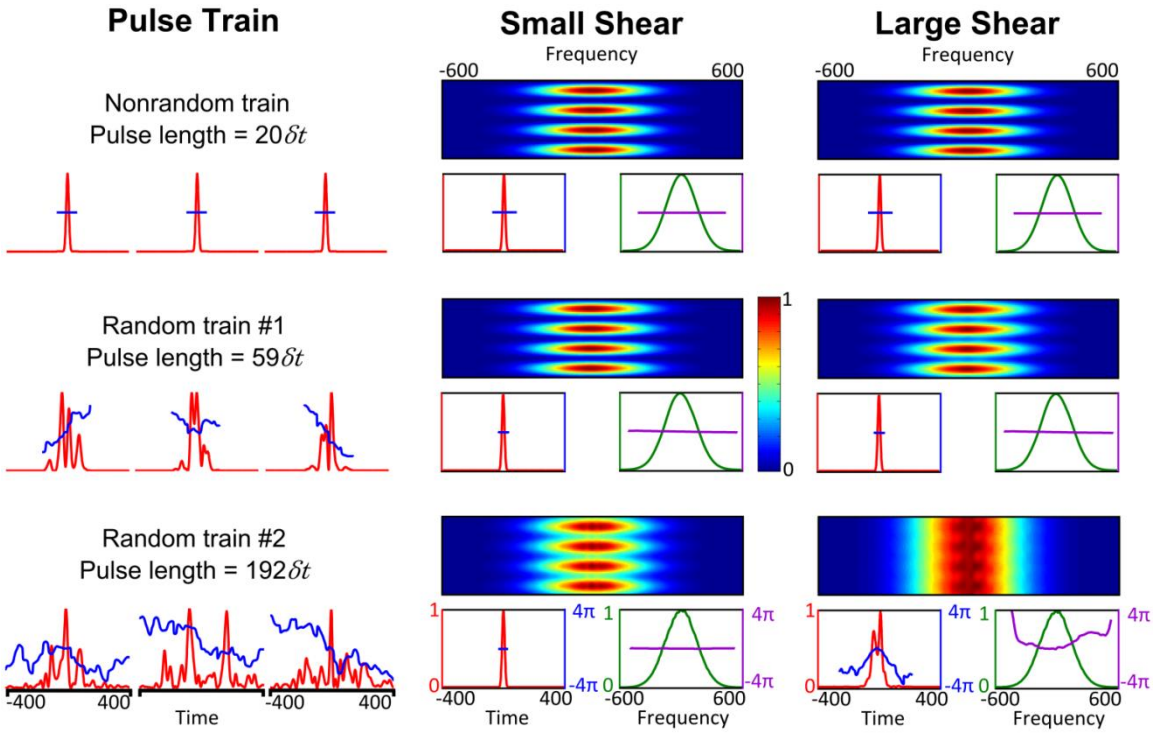

Figure 6.3: Coherent artifact simulation for 2DSI taking into account the relative spectral phase of up-converting frequencies [65]. Measurements in the middle column use a small frequency shear: 4% of the FWHM pulse bandwidth. The fringe visibility is 94% for the 60 δt train and 49% for the 192 δt train (backgrounds of 6% and 51% respectively). Measurements in the right column use a larger frequency shear: 10% of the FWHM pulse bandwidth. The fringe visibility is 76% for the 60 δt train and 3% for the 192 δt train (backgrounds of 24% and 97% respectively).

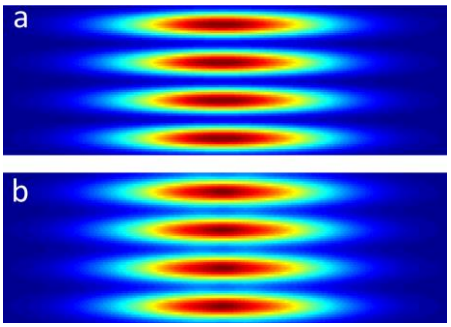

Figure 6.4: Direct comparison of fringe visibility for large-shear measurements of the 60δt pulse train (a) without and (b) with the relative phase correction. The background is 10% in (a) and 24% in (b).

Interestingly, the background for the shorter unstable pulse train increases much more when using a larger shear in this simulation (see Fig. 6.4 for direct comparison). While the background in the small shear measurement of random train 1 increases from 2% to 6% when the relative phase correction is included, the background in the large shear measurement increases from 10% to 24% in the more accurate simulation. This means that using background as an indicator of instability should be more robust than is suggested by the simpler simulation. However, most of the measurements still produce fringes that indicate a flat spectral phase and hence only a coherent artifact. The exception to this generalization is the larger shear measurements of the more complicated pulse train with the relative phase correction. In this case, the fringes are nearly nonexistent, with the background reaching 97% of the peak fringe visibility. The near-absence of fringes makes it abundantly clear that this measurement represents a highly unstable pulse train. The retrieved spectral phase is not particularly indicative of the characteristics of the pulse train, however. In fact, the retrieved phase changes if we choose different frequencies (still separated by the same shear) to up-convert the pulse (see Fig. 6.5).

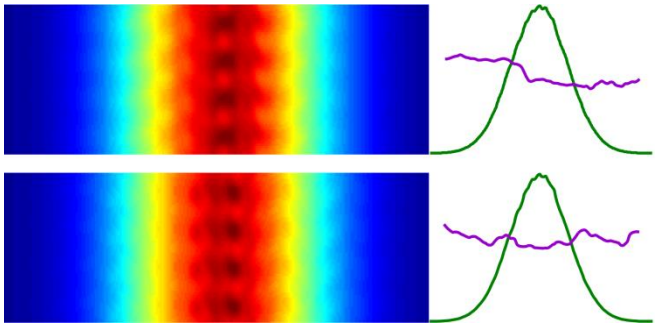

Figure 6.5: Examples of different spectral phases (purple line, right) retrieved from traces (left) of the longer pulse train using different pairs of frequencies in the chirped pulses to generate the same large shear. A third example is in the bottom-right corner of Figure 6.3.

Implications of the More Realistic Simulation

Based on our simulations, we conclude that considering the impact of spectral phase on the chirped pulses is informative and important when the spectral phase varies appreciably. Of course, the reality of using stretched pulses as quasi-CW beams to generate spectrally sheared replicas is even more complicated than the simple correction considered here. However, it is important to keep in mind that the viability of this measurement technique depends on having a suitably accurate mathematical description of the physical nonlinear measurement. If too many adjustments to the model are required to correctly model the experiment, then there are serious theoretical problems with the measurement technique.

In this case, further corrections or a full-field simulation are unlikely to result in better predicted fringe visibility. In addition, many other causes of reduced fringe visibility are likely to remain consistent in measurements with different spectral shears, while the fringe visibility caused by instability becomes distinctly more pronounced with large shears. We can therefore conclude that the presence of background in a large-shear 2DSI measurement is an effective warning of pulse-shape instability.

The Role of Spectral Shear

Because large-shear measurements are more sensitive to instability, it might be tempting to conclude that large shears are preferable in all cases. However, using large shears in spectral shearing techniques can yield less accurate spectral phases because the measurement effectively samples the group delay of the pulse more sparsely [71]. Another consequence of using large shears is that the assumption used to transform Eq. (6.1) into Eq. (6.2) becomes less accurate. When the shear is large, it is more of a stretch to assert that $\varphi(\omega + \Omega) - \varphi(\omega)$ is proportional to the derivative of the phase (a.k.a. the group delay, $\tau(\omega)$). Higher order terms in the expansion of the phase become more important as the shear increases, and dropping them introduces larger errors.

Fortunately, the frequency shear in 2DSI is an independent parameter that can be adjusted without changing other measurement parameters, by simply changing the delay between the chirped pulses. When the spectral shear is an independent measurement parameter, it is simple to make a large-shear measurement to verify the stability of the pulse train in addition to making a small-shear measurement to better estimate the spectral phase of the pulse. This has other beneficial implications: it has been shown that spectral phase measurements taken at different shears can be combined to improve the overall accuracy of the retrieved spectral phase [71].

A standard SPIDER setup does not have this flexibility, because the spectral shear and the delay between the pulses cannot be changed separately without also altering the amount of chirp applied to the stretched pulse. This makes it harder to do a direct comparison and makes it less likely that any background due to benign alignment issues will be consistent between measurements with different shears.

Averaging over a Small Number of Pulses

Making a measurement that averages over significantly fewer pulses still results in fairly flat spectral phases and short retrieved pulses. Figure 6.6 shows the results of averaging over 10, 50, and 200 pulses from random train number 1 (instead of all 5000) for both small and large shears, including the relative phase correction. For a small number of pulses with the type of variations we consider here, the average spectrum is significantly different from the average spectrum of the whole pulse train. Despite this, the measured spectral phase is quite flat, and therefore the retrieved pulses are quite short and simple in the time domain. Comparing trace a) and trace d) clearly shows the increased fringe displacement that occurs for larger shear values. The retrieved spectral phase is identical for both shears in all cases. The lower part of Figure 6.6 shows the ten pulses that contributed to the average in parts a) and d). These pulses are clearly rather long and complicated, in stark contrast to their average measurement. The lesson is clear:

averaging over only a few pulses does not protect one from making a very wrong measurement in the presence of serious instability.

The fringe visibility in a) is quite high at 97%, only showing a 3% background. Interestingly, the background in d) is 22%, which is only slightly lower than the 24%

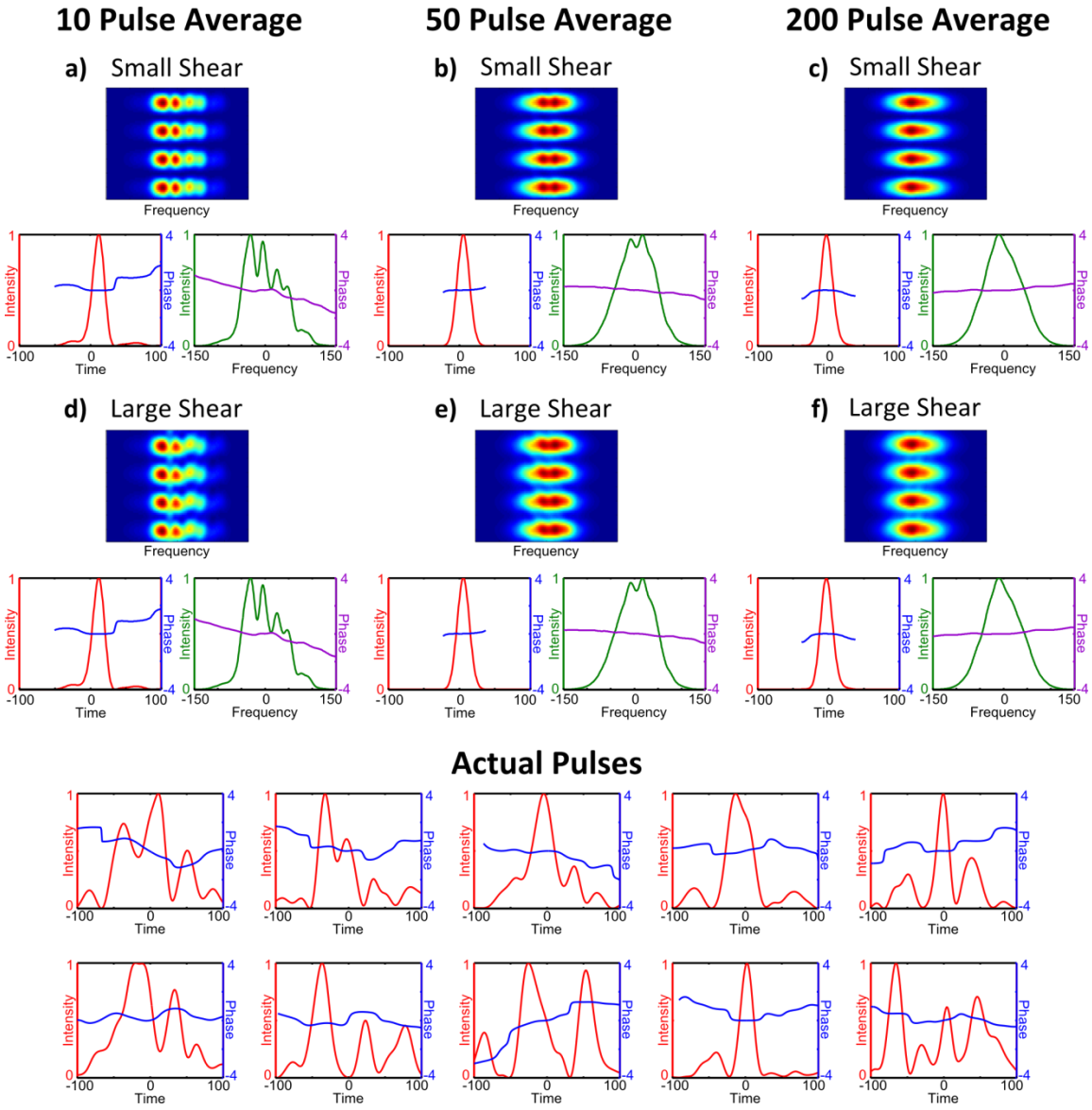

Figure 6.6: Coherent artifact simulation for 2DSI considering a small number of pulses taken from random train 1. Top row: traces created with small spectral shear (4% of bandwidth). Middle row: traces created with larger shear (10% of bandwidth). Bottom rows: temporal intensity and phase of the ten pulses averaged over in traces (a) and (d). Trace (a) has 97% fringe visibility and 3% background. Traces (b) and (c) have 94% fringe visibility and 6% background. Traces (d) and (e) have 78% fringe visibility and 22% background. Trace (f) has 76% fringe visibility and 24% background.

background present in the large-shear, full 5000-pulse average of that pulse train. When averaging over 50 or more pulses, the spectral phase is entirely flat and adding additional pulses mainly serves to even out the average spectrum. The background in the small shear traces b) and c) is 6%, consistent with the small-shear measurement of the full train. Likewise, the backgrounds in e) and f) are 22% and 24% respectively. Aside from the shape of the average spectrum, these measurements of 50 pulses are essentially the same as the corresponding measurements of 5000 pulses.

Of course, when we aren't working in the limit of averaging over many pulses, the exact characteristics and behavior of the pulse-to-pulse variations have a large impact on the results. One can therefore expect the threshold at which the average measured phase becomes flat to change based on the type and strength of the variations considered. Nevertheless, it is clear that it is possible for a measurement of only a few pulses to be quite wrong.

Summary

In conclusion, 2DSI generally retrieves only a coherent artifact when confronted with unstable pulse trains. But it can successfully warn users of very unstable pulse trains. This requires the extra step of taking a measurement with a large frequency shear to ensure that the fringe visibility is still good. In the absence of this additional information, however, 2DSI can misrepresent an unstable train of complicated pulses as a stable train of simple pulses. In addition, small variations might remain undetected even with an additional measurement. Consequently, this information should always be presented unless the stability of the source has been convincingly guaranteed in some other fashion.

CHAPTER 7

THE COHERENT ARTIFACT IN SELF-REFERENCED SPECTRAL INTERFEROMETRY

We have seen that two interferometric techniques, SPIDER and 2DSI, perform poorly when measuring unstable pulse trains. There have been two main reasons for this. The first reason is that variations tend to wash out of interferometric measurements, and the second reason is that SPIDER and 2DSI have no way to check if the measurement is correct. The strength of FROG lies primarily in the feedback provided by matching a retrieved trace to a measured trace.

In this chapter, we will consider self-referenced spectral interferometry (SRSI) [72], which is an interferometric technique that has a consistency check available. While the interferometric nature of this technique is likely to cause some issues, we find that its feedback can warn against incorrect measurements.

Introduction to SRSI

Self-referenced spectral interferometry is an extension of a technique that has been known for many years: spectral interferometry. Spectral interferometry measures the spectral phase of an unknown pulse by measuring the spectral fringes created between that pulse and a pulse with a known phase and a relative delay [73]. One of the major limitations of spectral interferometry for ultrashort pulse measurement is that a reference pulse with an equally wide or wider spectrum and a known phase is required to measure an unknown pulse. For very short pulses, an appropriate reference pulse is often not readily available.

SRSI attempts to overcome this limitation by using a nonlinear process known as cross-polarized wave generation to create a reference pulse from the unknown pulse. As

the name suggests, the pulse generated via this nonlinear interaction has a polarization orthogonal to the polarization of the input pulse, and therefore is easily separated from the input. This effect is third order and automatically phase-matched. A good approximation of the XPW reference pulse is:

$$E_{XPW}(t) = |E(t)|^2 E(t) = \mathcal{FT}^{-1}\{E(\omega) * E^*(\omega) * E(\omega)\} \quad (7.1)$$

which takes into account all the frequency combinations that contribute to the signal at a given frequency [74]. This process will tend to make a reference pulse that is shorter (or at least has sharper features) in the time domain. In many cases, this reference pulse will also have a broader spectrum with smaller, although still non-zero, phase variations compared to the input pulse. Equation 7.1 neglects other third order effects that could potentially occur, such as self-phase modulation and cross-phase modulation. In the limit that the conversion efficiency for XPW generation is very low, this is a reasonable assumption. As in standard spectral interferometry, the input pulse and the reference pulse experience a relative delay, and the resulting spectral fringes are measured by a spectrometer (see Fig. 7.1).

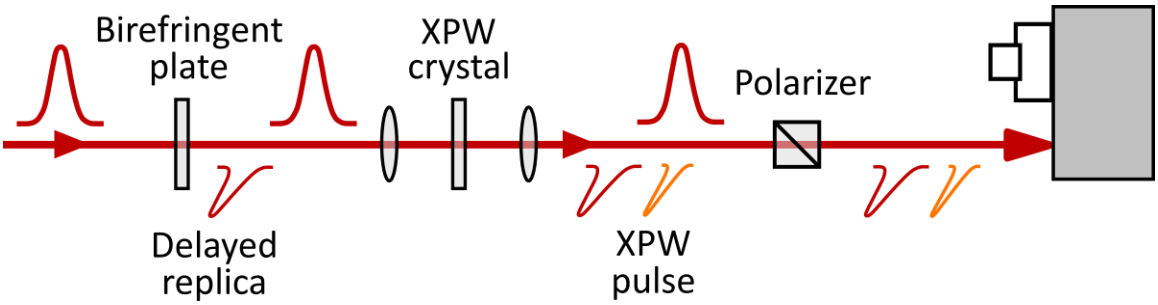

Figure 7.1: Basic experimental schematic for SRSI. A birefringent plate generates a delayed pulse replica that is orthogonally polarized. This replica generates spectral fringes with the reference pulse generated by XPW (shown here as the orange pulse). The input polarization is rejected by a polarizer before the spectrometer.

Retrieving Pulses in SRSI

Using standard Fourier-transform spectral interferometry (FTSI) techniques [73, 75], two spectra and the phase difference can be computed from the spectral interferometry signal. The phase difference measured in the trace is not necessarily equal

to the phase of the input because the reference pulse will have some residual phase; however, the true input phase can be retrieved iteratively [76, 77] (see Fig. 7.2). The first step is to estimate the XPW phase by simulating it, using the measured phase difference as the phase of the input pulse. With this estimate for the XPW phase, the input phase can be more accurately taken to be the sum of the measured phase difference and the XPW phase. This more accurate version of the input phase can be used to calculate a better estimate for the XPW phase, and the process iteratively continues until convergence is reached. Since a pulse is completely defined by its intensity and phase in the spectral domain, the pulse has been retrieved once its phase is found. A small issue with this retrieval algorithm is that the simulated pulses sometimes begin to accumulate linear spectral phase. This is very easily corrected by shifting the pulse back to its original temporal location in time on each pass through the algorithm, just before the XPW pulse is calculated.

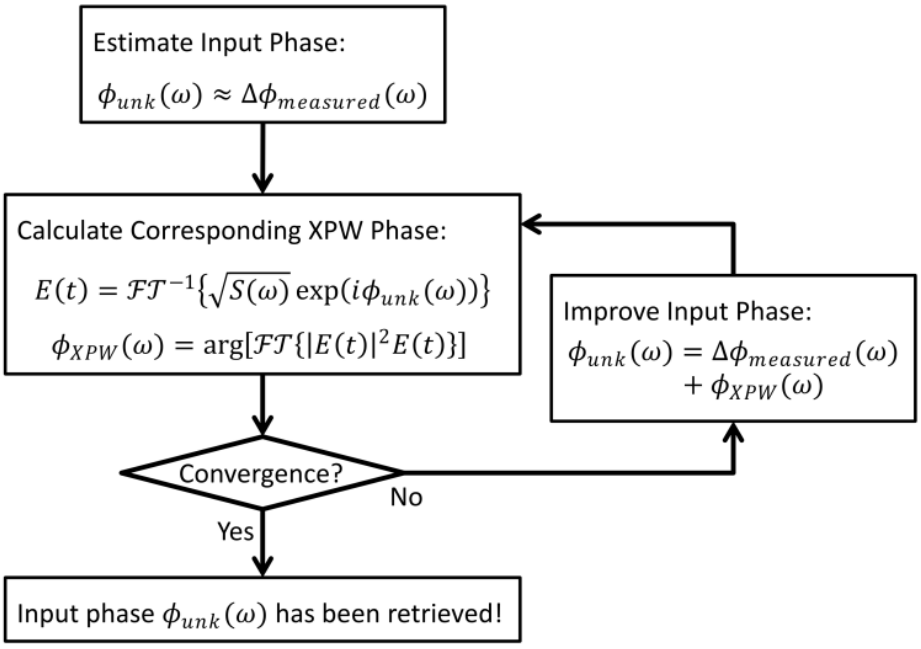

Figure 7.2: Phase retrieval algorithm for SRSI [76]. $S(\omega)$ is the spectrum of the input pulse to be measured, and $\varphi_{unk}(\omega)$ is its phase.

Convergence of the Retrieval Algorithm

The pulse retrieval algorithm for SRSI is said to have converged when the modification of the phase on a single pass of the algorithm becomes negligible [78]. Quick convergence is expected when the XPW reference has a spectrum that is at least as broad as the input spectrum. As the input phase increases and the reference spectrum narrows, the retrieval converges more slowly. It has been shown [78] that for quadratic phase and a Gaussian spectrum, the requirement that the reference spectrum be at least as broad as the input spectrum (a necessary requirement for spectral interferometry that SRSI must also follow) is a more conservative limit on the convergence conditions than would be imposed by the retrieval algorithm itself. For a Gaussian spectrum, the limits on various degrees of polynomial phase can be calculated, but in general, the convergence conditions of the algorithm must be simulated.

In our limited investigations, we simply ran through 20 iterations of the retrieval algorithm, rather than monitoring the change in the phase on each pass. The pulses that converged did so in less than 20 iterations, and those that failed to converge clearly stagnated well before 20 iterations. Although our simulations were far from exhaustive, in our experience the algorithm for SRSI is quite fast.

Limitations of SRSI and the Role of Feedback

SRSI relies on the input pulse to have a chirp that is small. Otherwise, the reference pulse generated by the XPW process will have a narrower spectrum than the input [74], resulting in an inability to measure the phase of some of the frequencies present in the input pulse. This restriction is quite limiting, and consequently this method is not endorsed by its creators for pulses chirped to more than twice their Fourier-transform limit [79]. In addition, non-ideal experimental conditions (such as poor polarizer extinction or alignment) can reduce this validity range even further.

If a pulse is not simple enough to generate a XPW reference with a broader spectrum, then the retrieval process will converge to an incorrect pulse. This is the case for the pulse shown in Fig. 7.3. While a separately measured input spectrum can be compared with the two measured spectra to indicate an unsuccessful measurement (and to make sure the XPW spectrum and the spectrum of the input pulse have not been confused for each other), it is difficult to know in advance if this technique will succeed in measuring the pulse. And it is important to remember that a technique that can only measure simple pulses will always give a simple pulse as a result, and so can yield a simple pulse when the pulse is in fact quite complex.

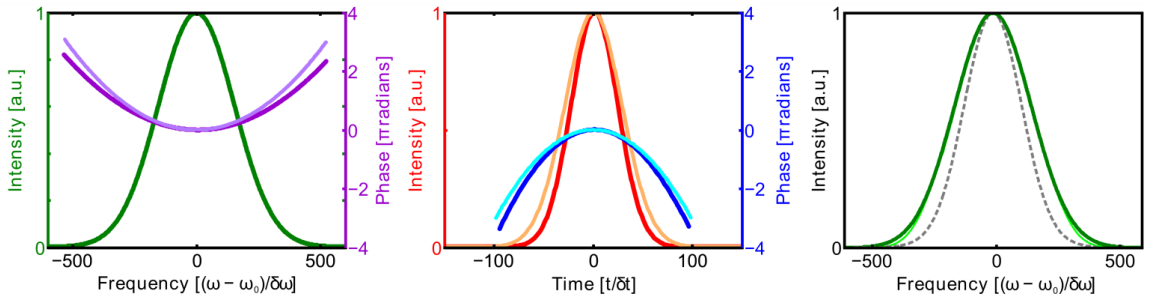

Figure 7.3: Example simulated measurement of a pulse that is outside the validity range of SRSI. Left: Retrieved spectral intensity (dark green) and phase (dark purple) with actual phase (light purple). Middle: Retrieved temporal intensity (red) and phase (dark blue) with actual intensity (orange) and phase (cyan). Right: fundamental (light green thin solid line) and XPW (dotted gray line) spectra retrieved from the trace with independent fundamental spectrum (dark green thick line). The measurement underestimates the chirp of the pulse and its temporal duration.

Ambiguities in SRSI

An ambiguity exists in a measurement technique if two distinct electric fields generate the same measurement result. Ambiguities are especially difficult to identify in ultrashort-pulse measurement techniques because the mathematics of these techniques is inherently nonlinear, making general analytical solutions difficult and generally unavailable. FROG benefits from its equivalence to a well-known, essentially well-posed problem: the two-dimensional phase-retrieval problem. But, in general, identification of ambiguities can only be performed by the brute-force running of large numbers of pulses

through a retrieval algorithm. Fortunately, this is not difficult to do. This has been done for FROG, and no ambiguities aside from trivial ambiguities have been found [62].

A similar approach yields no nontrivial ambiguities for SRSI within its limited validity range. We simulated measurements of over 5000 arbitrary pulses and found no cases in which the retrieval converged well to an incorrect pulse, although there were a significant number of pulses for which the retrieval did not converge. Some of those that did not converge were undoubtedly outside of the validity range of SRSI.

Theoretically, while it is clear that no two input pulses should generate the same reference pulse, it has not been proven that a pulse is uniquely determined by the quantities measured by SRSI. These quantities are the input pulse spectrum, the spectrum of the XPW pulse generated from it, and the phase difference between those two pulses. Even though the intensity and phase of the reference pulse is unique for each input pulse, it is not immediately clear that the phase difference is necessarily unique for each set of input pulse and corresponding reference pulse. It seems very unlikely that there would be a large number of nontrivial ambiguities associated with those constraints, however.

Feedback in SRSI

SRSI does have a couple of feedback mechanisms that are quite helpful in guarding against these problems. As has already been mentioned in the section on validity ranges, an independently measured spectrum should be compared to the two spectra calculated from the trace to make sure that the XPW reference pulse has a spectrum that is at least as broad as that of the input. This is necessary for remaining within the validity range of SRSI. The right panel of Figure 7.3 shows these three spectra. The independently-measured fundamental spectrum matches up well with the fundamental spectrum from the trace, and the XPW spectrum (gray line) is narrower than the fundamental spectrum If the input spectrum taken from the trace differs significantly from an independent spectrum, or if neither spectrum calculated via FTSI matches the

independent input spectrum, something has gone wrong in the measurement and the measured phase should not be trusted.

In addition, a much stronger consistency check is available. Similarly to how measured and retrieved traces are compared in FROG, in SRSI we can compare measured and retrieved spectra for the XPW pulse [78]. Once the phase of the input pulse has been retrieved we can calculate the corresponding XPW reference pulse and its expected spectrum. This can then be compared with the reference XPW spectrum measured in the trace. This feedback mechanism is rather sensitive, because the XPW process exaggerates temporal structure in the input pulse, and the temporal profile of the input pulse is sensitive to the spectral phase. Consequently, the retrieved spectrum of the XPW pulse will not match the measured spectrum if the retrieved spectral phase is incorrect. If the measured and retrieved XPW pulse spectra are not similar, again, the measurement result should not be trusted as correct.

To illustrate this, we generated example theoretical measurements of moderately complicated pulses, some of which converged to the correct pulse in the retrieval and some of which did not. We plot the spectral and temporal intensity and phase of these pulses, both actual and retrieved, along with four spectra: the actual spectrum (or independent spectrum), measured spectrum, measured XPW spectrum, and retrieved XPW spectrum. When the measured and retrieved XPW spectra are the same, the retrieved pulse is correct.

Figures 7.4-7.6 show these example pulse retrievals. Figure 7.4 shows a moderately complicated pulse that was not correctly retrieved. This is most evident in the discrepancy in temporal intensity between the retrieved pulse and the actual input pulse. The retrieved XPW spectrum does not agree with the spectrum measured in the trace, and the XPW spectrum measured in the trace is narrower than the spectrum of the input pulse. This pulse is outside the validity range of the technique, and comparing the spectra makes it easy to identify that this is the issue.

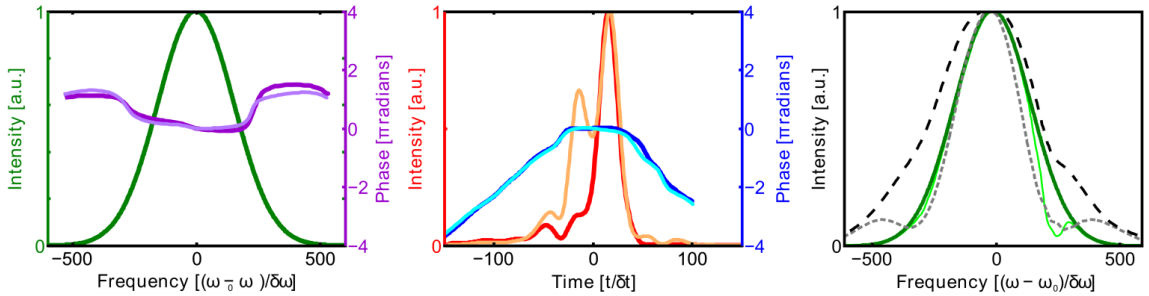

Figure 7.4: Example simulated measurement that was not correctly retrieved. Left: Retrieved spectral intensity (dark green) and phase (dark purple) with actual phase (light purple). Middle: Retrieved temporal intensity (red) and phase (blue) with actual intensity (orange) and phase (cyan). Right: Measured input (light green thin solid line) and XPW (gray dotted line) spectra from the trace with independent input spectrum (dark green thick solid line) and retrieved XPW spectrum (black dashed).

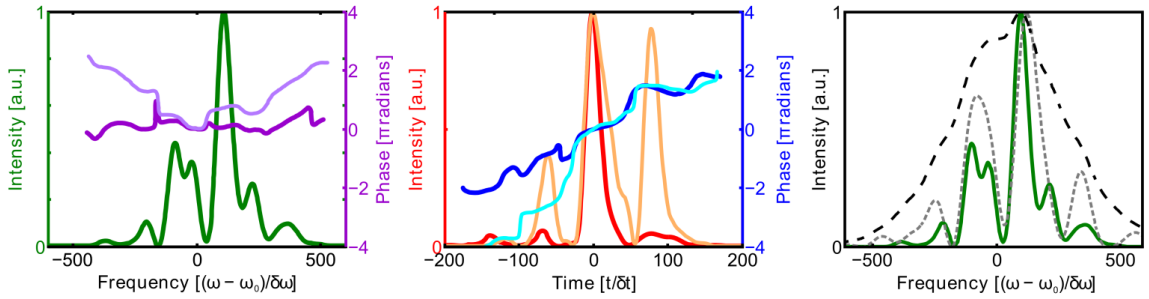

Figure 7.5: Another example simulated SRSI measurement that was not correctly retrieved. See the caption of Figure 7.4 for the color key.

Figure 7.5 shows a rather complicated pulse that also was not correctly retrieved. Again, the measured XPW spectrum is quite different from the retrieved XPW spectrum, very clearly showing that the retrieval has failed. The XPW spectrum measured in the trace shows that this pulse is on the edge of the validity range, neither obviously broader nor narrower than the input spectrum.

Figure 7.6 shows a complex pulse that was correctly retrieved. Note the excellent agreement between the input spectrum measured in the trace and the independent spectrum, and likewise between the XPW spectrum measured in the trace and the XPW spectrum simulated in the retrieval.

In summary, a SRSI measurement is correct if the measured XPW spectrum is broader than the input spectrum and if the measured XPW spectrum matches the retrieved XPW spectrum. Likewise, a measurement that does not have these qualities can

be very wrong. Given that such feedback mechanisms exist, they should be used and presented whenever possible to demonstrate that a result is indeed reliable. Without them, there is no way of knowing whether the measurement of an unknown pulse is actually correct or not.

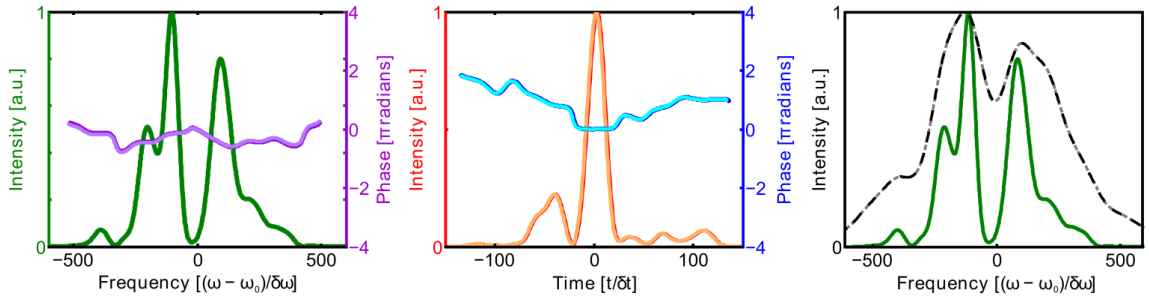

Figure 7.6: Example simulated measurement that was correctly retrieved. See the caption of Figure 7.4 for the color key.

Coherent Artifact Simulation for SRSI

We computed the average SRSI measurement of the random and nonrandom pulse trains (see Fig. 7.7). All three measurements retrieve the same result: a flat phase pulse that has the same temporal width as the stable component of the pulse train. Thus, SRSI measures only the coherent artifact in an unstable pulse train, as has been found for other pulse-measurement techniques that are based on interferometry.

The feedback available in SRSI appears to be quite informative, however. Contrasting the measurement of a stable pulse with the measurements of unstable pulse trains, we see that for the stable pulse, the spectral intensity measured via FTSI agrees exactly with the input spectrum. More importantly, the retrieved and FTSI-measured XPW spectra also agree well for the stable pulse. This is not true for the measurements of the unstable pulse trains. The discrepancy between the measured and retrieved XPW spectra is significant over the whole spectral range for both unstable trains. The average spectrum of the unstable pulses broadens only slightly through the XPW process. The simple flat-phase Gaussian pulse that is retrieved would generate a much broader XPW

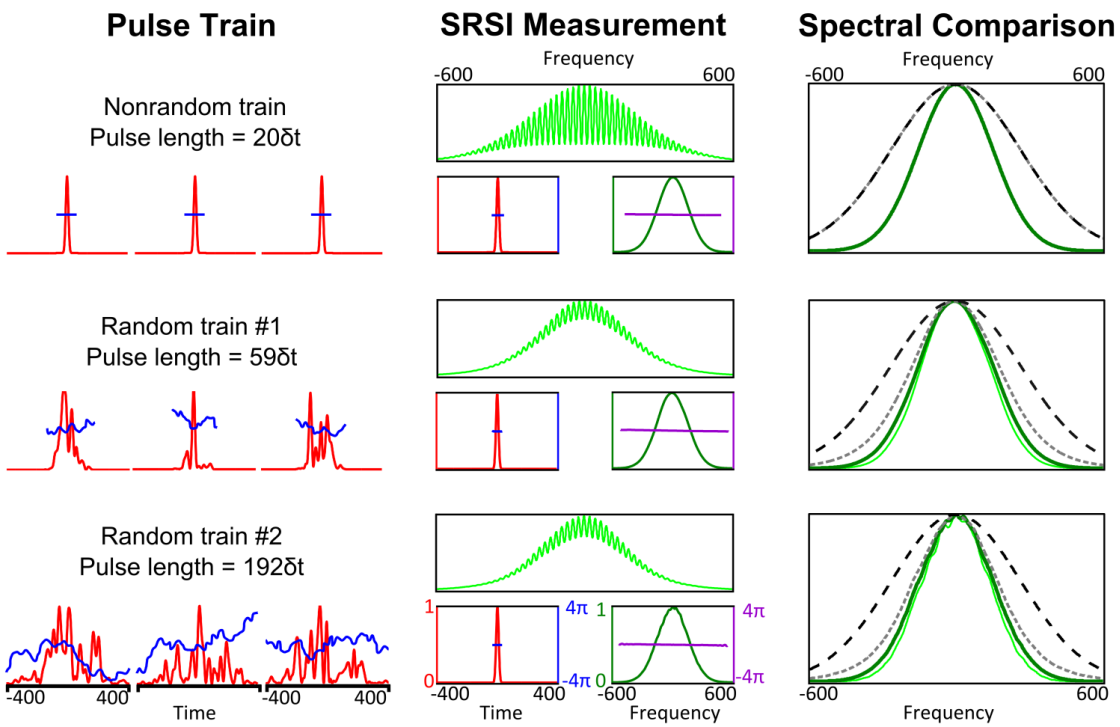

Figure 7.7: Coherent Artifact simulation for SRSI [80]. Example pulses are given on the left. The measurement and retrieved temporal and spectral intensity and phase are in the middle column (Red is temporal intensity, blue is temporal phase, dark green is spectral intensity, and purple is spectral phase). On the right, four spectra are plotted for comparison: the (average) input spectrum (dark green thick solid line), the spectrum of the input pulse measured in the trace (bright green thin solid line), the spectrum of the XPW pulse measured in the trace (gray dotted line), and the spectrum of the retrieved XPW pulse (black dashed line).

pulse, so the retrieved pulse is clearly not correct. Since the measured XPW spectrum is still clearly broader than the input spectrum, the issue does not appear to be that the input pulse is outside the validity range. Naturally, we understand that the real issue is instability, but it is a positive feature that a failed measurement due to instability is distinct from other causes. Since comparing measured and retrieved XPW spectra clearly indicates that the measurements of the unstable pulse trains have failed, the user is able to conclude that the retrieved phase is incorrect for reasons other than being outside the validity range of SRSI.

Contrasting the measured and retrieved XPW spectra plotted in Figs. 7.4-7.6with the corresponding plots in Fig. 7.7 further reinforces our conclusions about the simulated

measurements of unstable trains. These results suggest that if a pulse appears to be simple and inside the validity range, but it cannot be correctly retrieved, it is likely to be unstable.

Conclusions

While SRSI measurements of unstable pulse trains are quite misleading in the absence of feedback, when feedback is included it is much more informative than other interferometric techniques. Given that the feedback provided by comparing measured and retrieved XPW spectra is so helpful in identifying failed measurements, this feedback should be consistently used and reported.

CHAPTER 8

THE COHERENT ARTIFACT IN MULTIPHOTON INTRAPULSE INTERFERENCE PHASE SCAN

Multiphoton intrapulse interference phase scan (MIIPS) [81] is yet another technique for measuring ultrashort pulses. MIIPS is distinct from both autocorrelation techniques (like FROG) and interferometric techniques (like spectral interferometry, SPIDER, etc.). This technique measures the spectrum of a nonlinear signal as a function of the spectral phase applied with a pulse shaper. Because of its unique setup, its response to unstable pulse trains is more difficult to predict.

Retrieving Pulses With MIIPS

MIIPS relies on a pulse shaper to measure the pulse. It applies a phase function to the pulse and measures how the second-harmonic generation (SHG) spectrum of the shaped pulses changes as the phase function changes. Considering the expression for the SHG signal in terms of the spectral amplitude $|E(\omega)|$ and the ***net*** phase $\phi(\omega)$,

$$SHG(2\omega,\phi) \propto \left|\int |E(\omega-u)||E(\omega+u)| \exp\left[i\left(\phi(\omega-u)+\phi(\omega+u)\right)\right] du\right|^2 \quad (8.1)$$

we see that the SHG does indeed change based on the net spectral phase applied to the pulse. When the net phase varies with u, there is destructive interference in the integral and the second harmonic signal is reduced.

If we expand this phase in a Taylor series in terms of u, the odd terms cancel from the SHG integral and it becomes apparent that only the even phase terms affect the SHG signal. The second order term in u, related to the group-delay dispersion (GDD), is the dominant term. The magnitude of the integral is largest when the second harmonic signal experiences constructive interference for all contributing frequencies, implying that the net GDD must be zero to maximize the signal. Therefore if we scan the pulse with a

varying phase function, the SHG energy for a given frequency will peak where the net phase is zero, meaning that the applied phase function locally cancels the GDD. From the peak SHG at each frequency, we can determine the GDD of the pulse, which is easily integrated to give the spectral phase.

One way to scan the phase is to is to apply a series of constant chirps (constant GDD values) to the pulse [82]. The GDD values that maximize the SHG signal at each frequency are the values that locally compensate the pulse GDD. While the resulting traces are fairly intuitive, this approach is limited by the pulse shaper. Pulse shapers have a limited range of phases that they can apply, and phase wrapping can introduce aberrations. As a result, using constant GDD functions is not feasible if the pulse has significant phase.

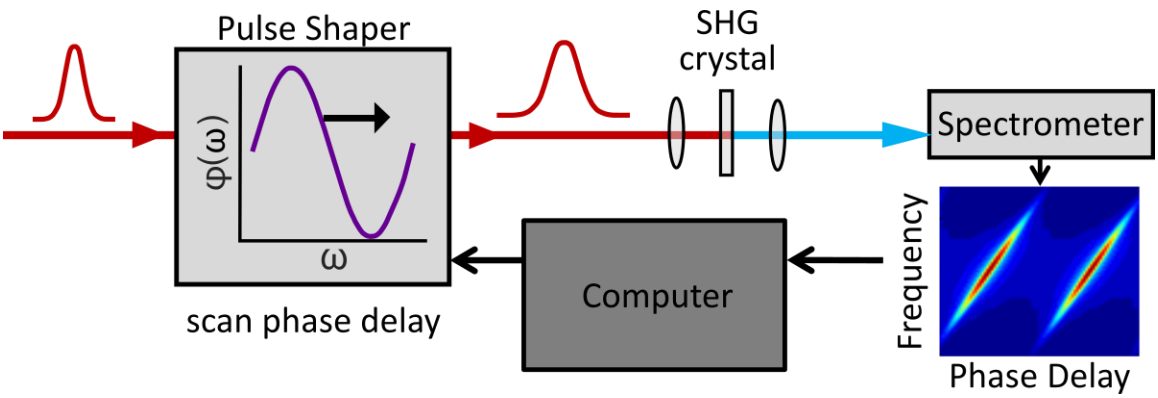

Figure 8.1: Experimental setup diagram for MIIPS. The phase function is scanned over the pulse spectrum to create the trace.

The more commonly used phase function for MIIPS is a sinusoid, because the GDD range of a sinusoidal phase function is larger than the phase range of the original phase function (see Fig. 8.1). The general formula for the sinusoidal phase applied by the pulse shaper is:

$$\phi_{ps}(\omega) = \Phi_0 \sin[f(\omega - \omega_0) - \psi] \tag{8.2}$$

where Φ_0 is the amplitude of the phase modulation, f is the frequency of the phase modulation, and ψ is the phase parameter that scans the modulation over the pulse bandwidth. The GDD applied by the pulse shaper is:

$$\ddot{\phi}_{ps}(\omega) = -\Phi_0 f^2 \sin[f(\omega - \omega_0) - \psi_{max}(\omega)] \tag{8.3}$$

Once the value of ψ that maximizes the SHG at each frequency is determined, the measured GDD of the pulse is equal to the opposite of the GDD applied by the pulse shaper:

$$\ddot{\varphi}(\omega) = -\ddot{\phi}_{ps}(\omega) = \Phi_0 f^2 \sin[f(\omega - \omega_0) - \psi_{max}(\omega)] \tag{8.4}$$

Unfortunately, the SHG peaks don't always represent precisely the local GDD. All frequencies present in the pulse have the potential to contribute to the signal at a given frequency, and consequently fast variations in the local GDD will tend to be smeared out. A dramatic example of this is shown in Figure 8.2. For a pulse with a phase jump, the peaks in the MIIPS trace are not close to the actual GDD of the pulse. However, even if the SHG peaks do not represent the exact GDD, the phase retrieved from the measurement can still be used to partially correct the phase of the pulse. In this way, a series of measurements and corrections can successfully determine and compensate the spectral phase of stable pulses.

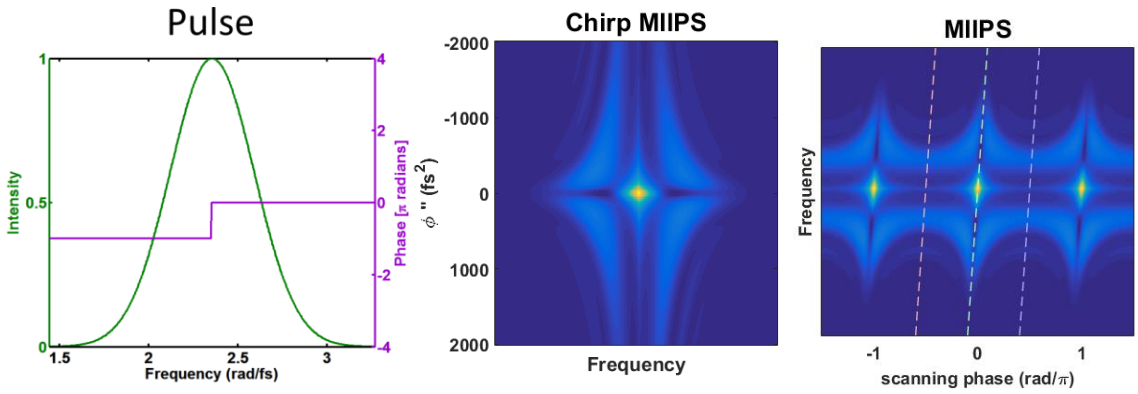

Figure 8.2: MIIPS trace of a pulse with a phase jump. Left: spectrum and spectral phase of the pulse. Middle: Chirp MIIPS measurement. The GDD range is 2000 fs^2. Right: MIIPS measurement. The light green dashed line is the zero-GDD line, and the pink and purple dashed lines are maximum and minimum GDD lines, respectively. Because of the sinusoidal phase function, these lines are diagonal. The total GDD range for the MIIPS measurement is the same as the chirp-MIIPS measurement.

Convergence and Feedback in MIIPS

We have alluded to the fact that MIIPS commonly functions as an iterative optimization routine. After each iteration, the phase applied by the pulse shaper is adjusted using the estimated GDD from the measurement. The pulse shaper compensates the phase measured on the last iteration and performs a new phase scan of the compensated pulse. Any phase remaining in the new scan can be used to more accurately compensate the GDD on the next iteration. The process finishes when the remaining GDD is below a user defined threshold (for ex. $20 fs^2$) or, more typically, when the measured residual phase is below $100\, mrad$. Through this process the MIIPS setup essentially provides its own feedback. If the phase is not fully compensated, it will be apparent in subsequent phase scans.

The simplest way to obtain external feedback on a MIIPS measurement is to compare the SHG spectrum of the fully compensated pulse to the theoretical flat-phase SHG spectrum. The SHG spectrum is already recorded in the trace along the zero-GDD line, and this can be compared to the SHG calculated from an independently-measured spectrum, assuming a flat phase. A full trace can also be computed for the theoretical flat-phase pulse, but this is not typically necessary.

Error Estimation

There are two methods for estimating the error in retrieved phase for MIIPS. The most straightforward is to make several traces of the compensated pulse. Since noise is different for each trace, most noticeably in the wings of the spectrum where the signal is low, the measured residual phase can vary from trace to trace. Comparing the retrieved phases, we can derive a statistical error for the phase. This is especially helpful in determining close to the edges of the spectrum the phase can be well-determined. Unfortunately, it is quite difficult to measure the phase at the edges of the spectrum with any nonlinear method.

A second method for estimating the error in the phase, which also provides good measurement feedback, is to create a retrieved trace using an independent spectrum and the retrieved phase. Any differences in the locations of peak SHG intensity between the measured and retrieved traces indicate an error in the retrieved GDD. As mentioned in previous sections, this is always a possibility because MIIPS theory does not account for the effects of the spectrum on the trace. These differences can even be used to refine the retrieved GDD, updating the phase applied to the independent spectrum until its trace matches the measured one. This iterative trace-matching procedure can even replace the process of making additional MIIPS traces to completely determine the phase [83].

Validity Ranges

The choice of sinusoidal phase function in MIIPS has a large effect on the measurement and must be considered carefully. Choosing appropriate values for Φ_0 and f is key to making a successful measurement.

For MIIPS, the modulation frequency f is often chosen to be close to the temporal pulse length. This is done to decrease the contributions of higher-order terms in the applied GDD. MIIPS theory assumes that only a (linearly varying) second order phase is applied to the pulse, when in reality the applied GDD is a polynomial of many orders:

$$\ddot{\phi}(\omega) \approx -\Phi_0 f^2 \left[(f(\omega - \omega_0) - \psi) - \tfrac{1}{3!} (f(\omega - \omega_0) - \psi)^3 + \cdots \right] \qquad (8.6)$$

Choosing a modulation frequency close to the pulse length avoids having multiple oscillations of the sinusoidal phase function within the pulse bandwidth. This rule of thumb will typically ensure that higher order terms are not too problematic. In any case, lower modulation frequencies are clearly preferred, as long as associated GDD range is larger than the GDD range of the pulse to be measured. From Equation 8.3, we see that the maximum GDD that can be measured and compensated on a single iteration is $\Phi_0 f^2$. If a very large GDD range is required, MIIPS must choose between introducing significant higher-order phase terms with a high modulation frequency, or distorting the

pulse spectrum with a large modulation amplitude that causes phase-wrapping at the pulse shaper.

Ambiguities

Since MIIPS is based on SHG, the trivial ambiguities associated with SHG spectra should be addressed. Although SHG FROG measurements have an ambiguity in the direction of time, this ambiguity is not present for MIIPS because the sign of the phase applied to the pulse by the phase-shaper is always known. Thus positively and negatively chirped pulses are obviously distinguishable. Another potential ambiguity is the relative phase of double pulses. Because the second harmonic spectrum is identical for double pulses with a relative phase of either zero or π, MIIPS cannot distinguish those phases from the trace alone. However, the fundamental pulse spectrum easily resolves this confusion, and the relative phase of two pulses can be determined to within factors of π from the position of spectral fringes in the trace.

I have also attempted to find ambiguities in MIIPS by brute-force trace matching. I simulated a measurement of an arbitrary pulse, and modified a second pulse until the difference between their traces was minimized. Repeating this process hundreds of times yielded no examples of different pulses with the same MIIPS trace. While this does not guarantee that MIIPS is completely free from nontrivial ambiguities, it demonstrates that such ambiguities are difficult to find.

Coherent Artifacts

We computed the averaged MIIPS traces for the unstable pulse trains. Only one phase scan was computed, so the traces do not include any phase compensation. The GDD range for both MIIPS and chirp-MIIPS is 2000 fs^2.

MIIPS responds relatively well to averaging over a train of complicated, unstable pulses. Figure 8.3 shows averaged traces for both MIIPS using sinusoidal phase and

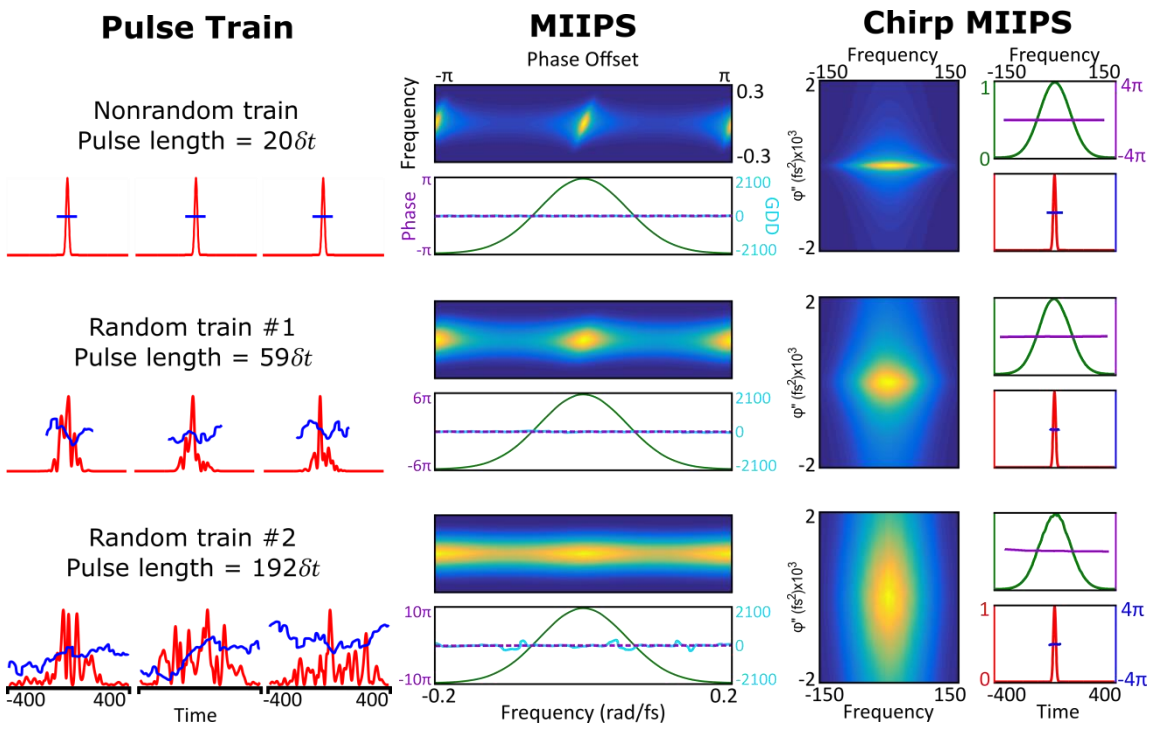

Figure 8.3: Simulated averaged MIIPS measurement of unstable pulse trains. Left: Example pulses from the unstable pulse train. Middle: averaged MIIPS measurement. The GDD range is $\pm$ 2000 fs^2. Retrieved temporal pulse shapes are not show, but they is identical to the pulse shapes retrieved by chirp-MIIPS. Right: chirp-MIIPS measurement. The GDD range is $\pm$ 2000 fs^2.

chirp-MIIPS. As expected, the averaged traces for the two types of phase functions are very much analogous. MIIPS measures a flat phase for the unstable trains, even though the phases of the individual pulses are far from flat. While the retrieved temporal pulse shape is not shown for MIIPS, its results are identical to the results for chirp-MIIPS. MIIPS retrieves only the stable component of the pulse train, and care is therefore necessary.

Since the pulses in the unstable trains have GDDs that vary over a large range, the SHG signal for unstable trains is spread over a large range of applied GDDs, rather than being localized around peak values. Consequently, the averaged traces are unusually wide in the GDD direction compared to the stable measurement. Similar simulations have been done for chirp-MIIPS by another group, showing that the shape of the wings in the GDD direction may contain clues about the type and severity of the instability [84, 85].

While these broadened traces are fairly distinctive, care should be taken that small amounts of GDD broadening do not go unnoticed. It is therefore suggested that a retrieved trace or theoretical trace be computed and compared to the measured trace for added security against unexpected unstable pulses.

Conclusions

MIIPS and its associated issues are described in detail. No non-trivial ambiguities are identified for this method, although a more exhaustive search could be illuminating. MIIPS measurements of unstable pulse trains are slightly ambiguous and could benefit from comparing a measured trace to the trace theoretically expected for a given spectrum. This simple feedback step could be very helpful in identifying or eliminating the possibility of instability. Without this feeback, small amounts of instability may be unnoticed.

CHAPTER 9

PLOTTING SPATIOTEMPORALLY COMPLEX PULSES IN SPACE AND TIME

When performing complete measurements of ultrashort laser pulses, it is difficult to plot the resulting electric field in an intuitive and meaningful way, due to the volume and complexity of data. In the most general case, the measured electric field is a spatiotemporal function whose space and time dependencies are coupled and non-separable. Also, as the electric field is a complex function that contains both magnitude and phase variations, the need to display these variations simultaneously adds additional complexity.

To solve this problem, we generate movies of measurements of complete spatiotemporal electric fields, computing spectrograms to determine the field's spectral content around a local time for each point in space. We then calculate overlap integrals between these spectrograms and red, green and blue (RGB) false-color spectral response functions.

In this chapter, we discuss the general principles of spectrogram-based plotting and RGB color-response characteristics, and we compare this method with a previous instantaneous-frequency-based plotting method in the context of spatiotemporal laser pulse measurements. We demonstrate our method by generating movies of complex and interesting pulses that typically can be observed in ultrafast-optics labs and finally discuss the limitations of this current plotting method.

Difficulty of Spatiotemporal Display

It has recently become possible to measure the complete spatiotemporal electromagnetic field of an ultrashort laser pulse [86]. Among the measurement

techniques, STRIPED FISH [87] and SEA TADPOLE [88] have proven their ability to measure a wide range of pulses [89-91]. When measuring complex spatiotemporal waveforms such as in [92-95], challenges exist not only in the measurements but also in simply plotting the information obtained. The spatiotemporal waveform contains considerable information: the vector electric and magnetic fields are complex values that vary as a function of space (x, y, z) and time (t). All of these characteristics add up to a daunting number of dimensions to display. Fortunately, because the magnetic field corresponds very directly to the electric field [96], plotting magnetic field is not necessary and coveys no additional information. Further, since the z-dependence of electric field can be completely determined by diffraction integrals [97] once the field at a particular z-plane is known, we can eliminate dependence on the z-direction from our measurement. In addition, the electric fields in the majority of laser applications are highly polarized [98], so usually only one polarization direction is of interest and needs to be considered. However, even so, effectively plotting this highly simplified quantity $E(x, y, t)$ remains challenging, because the complex field $E(x, y, t)$ contains two three-dimensional datasets, $I(x, y, t)$ and $\phi(x, y, t)$, corresponding to intensity and phase functions varying with time and two transverse spatial coordinates. Therefore, the measured electric field $E(x, y, t)$ that contains the complete pulse information still has far too many degrees of freedom to be readily displayed in one simple diagram.

Measuring Pulses in Space and Time

Despite the multi-dimensional information contained in the pulses, most current methods to measure ultrashort pulses ignore all but one or two degrees of freedom of the fields [87]. The symmetry properties of pulses in some special cases permit such dimensional reductions in measurements [99, 100] without losing relevant information. Beams may be rotationally symmetric or have invariant or uniform profiles along one

spatial dimension. However, in general, some pulse characterization technique should be able to measure and display arbitrarily-varying complete spatiotemporal field.

Very recently, our group has developed two methods for measuring the spatiotemporal field of an arbitrary ultrashort laser pulse. One, called Spatially Encoded Arrangement for Temporal Analysis by Dispersing a Pair Of Light E-fields (SEA TADPOLE) [88], measures the field with ultrahigh spatial (and temporal) resolution, but it is necessarily multi-shot and so requires a stable, high-repetition-rate laser source. Because SEA TADPOLE requires potentially tedious scanning in the spatial dimensions, it is often used to obtain only a subset of the full 3-dimensional information.

The other, called Spatially and Temporally Resolved Intensity and Phase Evaluation Device: Full Information from a Single Hologram (STRIPED FISH) [87] has more coarse spatial resolution, but it can operate on a single-shot basis and so can measure pulses from high-intensity lasers, which inherently have low repetition rates. STRIPED FISH always measures the complete spatiotemporal field in all dimensions and hence always yields such large datasets.

Basics of STRIPED FISH

STRIPED FISH measures pulses by characterizing their interference with a known reference pulse. The reference pulse can be obtained by splitting off part of the unknown pulse and spatially filtering it (see Fig. 9.1a). This guarantees that the reference pulse is spatially simple and coherent with the (potentially complex) unknown pulse. The spatially filtered reference pulse can be characterized by a temporal-domain measurement technique (which typically assumes a spatially smooth profile), such as Frequency-Resolved Optical Gating (FROG) [43, 101].

By design, STRIPED FISH is a very simple device, comprising a coarse two-dimensional transmission grating, an interference bandpass filter, imaging optics, and a camera (see Fig. 9.1b). The spatiotemporally known reference pulse and unknown pulse

are sent into the STRIPED FISH apparatus with a small relative angle. The slightly rotated coarse grating diffracts the beams into a slightly rotated array of divergent beam pairs. Because the transmission wavelength of the bandpass filter varies with angle, these beam pairs are filtered into different colors by the filter. Then, after passing through the imaging optics (designed to correct aberrations and make the intensities of the holograms homogeneous), the beam pairs finally arrive at the camera, overlapping and forming a slightly rotated array of monochromatic holograms. With knowledge of the reference pulse, the recorded holograms can be interpreted to obtain the unknown spatiotemporal pulse field [87].

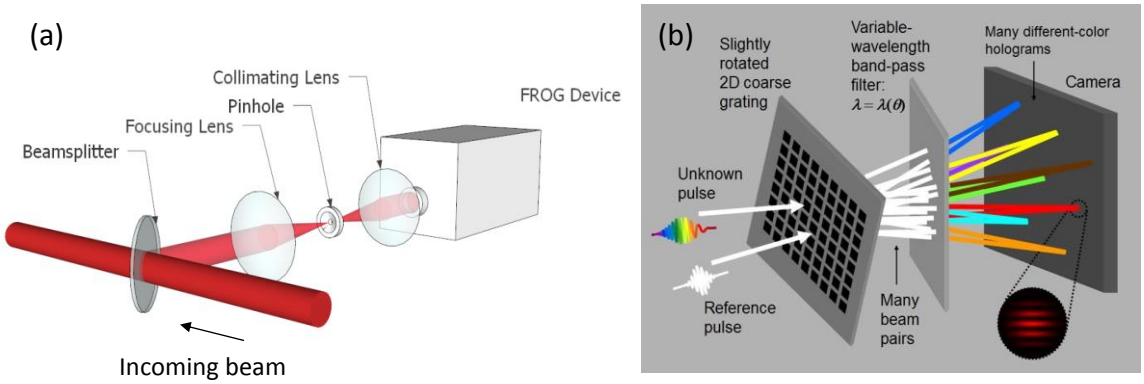

Figure 9.1: Diagrams for STRIPED FISH. (a) Obtaining a known reference pulse. Some of pulse energy is split away, spatially filtered (which yields a spatially uniform pulse) and then temporally measured by a FROG device. This yields a spatiotemporally completely known reference pulse. The spatial filter is made of lenses and pinhole (for ultra-broadband pulses, curved mirrors should be considered to replace the lenses to avoid chromatic aberration). (b) STRIPED FISH apparatus. An unknown pulse and the spatiotemporally known reference pulse are combined into the STRIPED FISH apparatus, forming multiple holograms of different frequency on the camera. Imaging optics are omitted in this conceptual plot.

STRIPED FISH measurement provides the complex electric field versus time or frequency for each transverse spatial point, i.e. $E(x, y, t)$ or $E(x, y, \omega)$. It is important to note that the STRIPED FISH technique measures data in one particular z-plane. Direct retrieval of the data shows the time evolution of the pulse in that particular plane, not the longitudinal pulse structure frozen at a given time. While we can certainly use diffraction

integrals to determine the field profile along the z-direction, considering temporal evolution in the measured z-plane will be the focus of this chapter.

Previous Attempt to Visualize Multi-dimensional Data

The method used to display data measured with SEA TADPOLE has many strengths, but also has a few key weaknesses. An example plot of SEA TADPOLE data is shown in Figure 9.2. The figure brightness is scaled to the intensity $I(x, y, t)$ and color is used to represent instantaneous frequency. The instantaneous frequency of the field is $\omega_{inst} = \frac{\partial \phi(x,y,t)}{\partial t}$ (this expression may have a minus sign depending on the sign conventions used), which characterizes the field phase variation in time. Any local average-frequency deviations away from the carrier frequency will be apparent in a plot of the instantaneous frequency. While this may seem like a natural and effective way to displaying phase/color information, there are some issues with this approach.

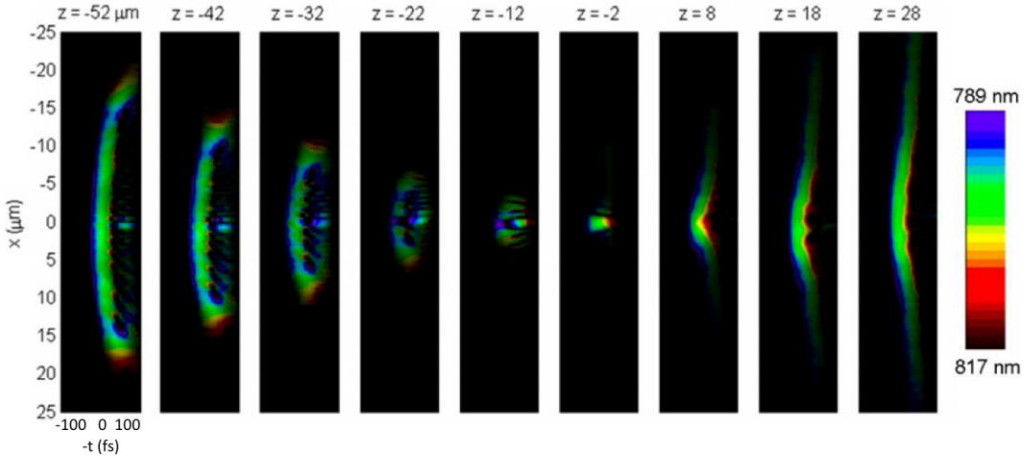

Figure 9.2: A SEA TADPOLE measurement of an aberrated, focusing pulse, from [86]. Measurements taken at 9 different z-planes (and here seen from the side) show the evolution of the spatiotemporal pulse shape through the focus. Color shows the average instantaneous wavelength, but does not display any information about the bandwidth (spectral width) of each part of the pulse.

Plotting the instantaneous frequency (or wavelength) leads to ambiguities, so it is not generally sufficient to describe the phase. From the plot, for example, one cannot tell how large the bandwidth of the fore-runner pulse (the small pulse that precedes the main

pulse) is in the leftmost frame. It is shown as green, which simply means that its average wavelength is around 800nm. It would be plotted the same way if it were nearly monochromatic, or if it contained largely the whole pulse spectrum. Plotting just the instantaneous frequency tells us very little about the spectral field energy distribution. It would be highly preferable to develop an intuitive scheme that displays the phase information by showing the spatiotemporal spectral energy distribution.

Using Spectrograms to Plot the Phase

To represent the phase of pulses more meaningfully, we must first identify a mathematical quantity that has the characteristics we care about. One such mathematical construct that is useful for our purposes is the spectrogram. The spectrogram (or equivalently, the sonogram) has been used for many years specifically for its strength in demonstrating the distribution of signal energy in time and frequency [102]. The first proponent of the spectrogram referred to it as the "physical spectrum" because it intuitively displays the time-frequency characteristics of various signals [103]. A spectrogram is defined as:

$$Sp(T,\omega) = \left| \int_{-\infty}^{+\infty} E(t)g(t-T)\, exp(-i\omega t)dt \right|^2 \tag{9.1}$$

The spectrogram, also called the short-time Fourier transform, is a two-dimensional function of frequency and delay. It requires a gating function $g(t-T)$ to select out a temporal chunk of the signal around a local time T. Then, the spectrum of the gated signal $E(t)g(t-T)$ is recorded for each delay T between the signal and gate. As we will discuss in detail later, a spectrogram depends on the gate function used to construct it and is not unique for a given signal. By itself, the spectrogram does not solve our issue of having too many degrees of freedom to display. In fact, it has made the problem even worse: instead of each point in space having only time-dependent field variations, now each point has its own spectrogram that depends *both* on delay *and* on frequency. At least, however, it will solve the display problems with the instantaneous frequency.

Drawing Inspiration from the Eye

To solve this dilemma, we draw inspiration from the human eye. The human eye observes the motion of objects as "movies", by processing the incoming light from environment. In the retina of human eyes, there are millions of neural photoreceptor cells, called rods and cones. While both rods and cones respond to the intensity of incident light, the rods are more sensitive and saturate at lower intensity values. The receptors that are responsible for color discrimination (related to phase information) are called cones and consist of three types: S, M and L [104]. These three types refer to their peak spectral sensitivity to short, medium and long wavelengths of light, respectively. Acting as a very low-resolution spectrometer, they allow us to appreciate a huge variety of spectral signals of different wavelengths and bandwidths. Lying at the confluence of physics, physiology and neuroscience, the biophysical mechanism behind color vision is rather complex [105-107]: the process includes a multi-stage model of trichromatic color theory (involving the retinal cone cells) and opponent-color theories (involving additional neural cells in the retina and the processing center in the brain), and it is still an active area of research [106]. However, if we consider a simplified trichromatic model of human vision, which only involves the integrated responses of the three primary cone receptors, we can borrow some ideas to visualize ultrashort pulses.

It is important to note that human eyes do not have particularly good temporal resolution. They act as integrating detectors, and they have a minimum repetition rate - our eyes cannot distinguish repeated light pulses above this rate from a steady and continuous light. This minimum repetition rate is referred to as the "flicker fusion threshold". It effectively is related to the temporal sampling frequency of the human eye, and the typical response frequency is between 1 Hz and 60 Hz, depending on the light intensity, wavelength, and modulation rate [108]. Taking inverse of this quantity gives us an upper bound on the effective width of the time gate, employed by our eyes (0.017~1s). The human visual system therefore effectively generates spectrogram

functions for each point in space on the retina, and detects these functions with the S, M, and L cell spectral receptors, through an integration process. This is exactly the visualization problem that we want to solve, and it follows that using coarse spectral filters to color-code the phase through spectrograms is an ideal solution.

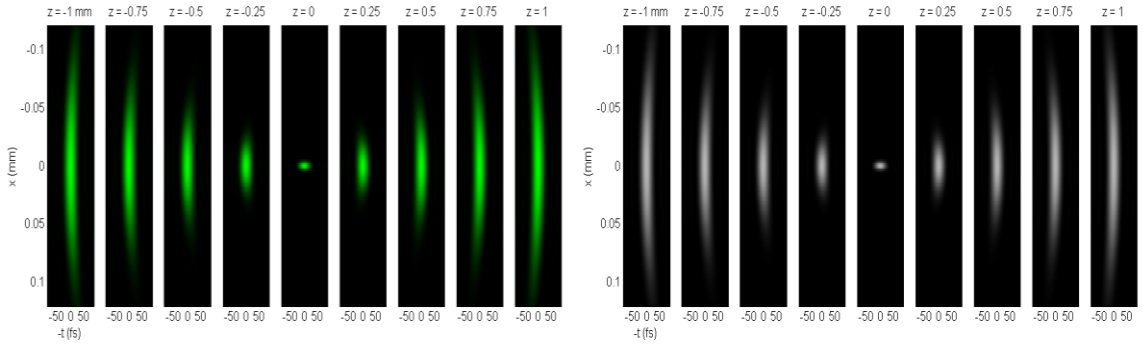

Figure 9.3. Focused pulse with its entire spectrum, plotted using instantaneous frequency coloring as green (left), and using spectrogram-based coloring as white (right).

Accordingly, we will mimic human vision by using not only spectrograms (of course using time gates of the length-scale of ultrashort pulses) but also spectral response functions to encode the phase. We accomplish this by defining simple Gaussian spectral response functions for red, green, and blue color channels. As shown in Figure 9.3, for an ideally focusing pulse with no chromatic aberrations, the instantaneous frequency plotting will make the pulse look green, but the RGB color approach will give white when the whole pulse spectrum is present in the graph. In this way, the RGB color value represents spectral energy distribution.

Converting Spectrograms to RGB

In order to understand the spatiotemporal spectral energy distribution, we compute a spectrogram for each of the spatial points in the beam, depending on the frequency ω and delay T. For a numerically generated gate pulse, $g(t)$, the spectrogram is:

$$Sp(x, y, T, \omega) = \left| \int_{-\infty}^{+\infty} E(x, y, t) g(t - T) \exp(-i\omega t)\, dt \right|^2 \qquad (9.2)$$

To color-code its information for display purposes, we define red, green, and blue response functions $R(\omega)$, $G(\omega)$, and $B(\omega)$, centered at longer, middle, and shorter wavelength sides in the pulse spectrum. We then use overlap integrals to compute how much red, green, and blue content is present at each time and position in the pulse.

$$R(x,y,T) = \int_{-\infty}^{+\infty} Sp(x,y,T,\omega)R(\omega)d\omega \tag{9.3}$$

$$G(x,y,T) = \int_{-\infty}^{+\infty} Sp(x,y,T,\omega)G(\omega)d\omega \tag{9.4}$$

$$B(x,y,T) = \int_{-\infty}^{+\infty} Sp(x,y,T,\omega)B(\omega)d\omega \tag{9.5}$$

Each of these functions is scaled afterwards such that each function has the same total energy and the RGB values are between zero to one, normalizing the colors to the pulse spectrum. This leaves us with three-dimensional RGB functions to plot for each spatial point at each delay, which is ideal for making movies of how the spectral characteristics of the pulse's spatial profile change over time. The brightness of the color then indicates pulse intensity. Intuitively, times and positions that contain no pulse energy will be shown as black. More intense color at each position and delay represents more frequency content of the pulse in that spatiotemporal voxel. Additionally, any part of the pulse that contains the whole pulse spectrum should be unbiased in color and thus appear white (or colorless).

The normalization in this data presentation technique is appropriate for ultrashort pulses because pulses from well-engineered ultrashort lasers tend to have simple, smooth and broad Gaussian spectra with essentially no biases towards high or low frequencies. As a result, using color to display the average spectrum is not what we are very interested in. Instead, we are more interested in cases where different frequencies are present and a local spectrum is (potentially) biased. For other applications, a different normalization system that puts more focus on the average spectrum could be more appropriate under certain circumstances.

Effects of Parameter Choices

The degree of color saturation in the movies we generate is determined by two factors. The choice of the gate pulse plays a very large role. Shorter gate pulses generate spectrograms with better temporal resolution but poorer spectral resolution. This means that the spectrogram signal at each delay will be shorter in time and consequently more broadband in frequency. Given the same spectral response functions, a spectrogram with a shorter gate will result in a lower color saturation and a more white-looking movie. Conversely, choosing a longer gate pulse – implying poorer temporal resolution of the spectrogram – results in a better spectral resolution. A movie made from such a spectrogram will have higher color saturation.

Generally speaking, the most informative results come from achieving an optimal balance between temporal and spectral resolution of the spectrogram. Often the best compromise for ultrashort pulses is to choose a gate pulse close to the same temporal duration as the pulse itself [43]. However, in some cases it may be interesting to emphasize either good spectral resolution or good temporal resolution. When the signal has variations in instantaneous frequency that must be resolved, the optimal gate length scales inversely with the rate of change of the instantaneous frequency (the second derivative of the temporal phase of the pulse) [109]. In other words, the more complicated and quickly varying the signal is in time, the shorter the gate pulse must be to catch these variations.

The two limiting cases for the gate pulse are when the gate is an impulse delta-function in time and when the gate is infinitely long. The first case has the best temporal resolution but totally uncertain, washed-out frequency information, resulting in a movie that shows no spectral energy variations. The arrival time of spatial structures is precise, but the pulse will appear white at all times. The second case gives ultimate frequency resolution but totally non-localized temporal distribution. The spatial distribution of colors will be very well defined, but it will not evolve in time. Both of these cases result

in loss of information in the movies. It is always important to understand that the choice of gate function has a strong impact on the ability of movies to display frequency variations. Color response functions cannot recover frequency resolution that has been lost in making a spectrogram with a short temporal gate function.

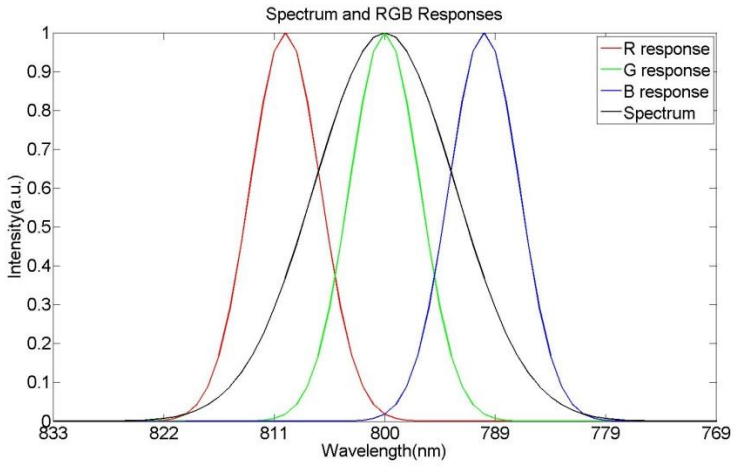

Figure 9.4. Example choice of RGB response functions with respect to the pulse spectrum. Note that RGB function widths and their separations determine appropriate overlapping with the pulse spectrum (and with each other). The pulse under investigation has duration of 70fs and temporal chirp (a linear temporal ramp in frequency) of $-2 \times 10^{-4}\ fs^{-2}$. Similar function parameters are used to make movies in the next section.

While the width and placement of spectral response functions can certainly play a role in the color saturation of the movies, the choice of these functions is somewhat less critical, due to the choice of smoothly-varying Gaussian spectral functions and the normalization of colors. There should be some overlap between the functions chosen (see Figure 9.4), so that there are no areas of zero or near-zero response within the spectrum of the pulse. Otherwise, there may be unnatural-looking divisions of color in movies, or regions that look monochromatic despite actual presence of many different frequencies. If there is a large overlap between the response functions, the color differentiation will be weak and the pulse will simply appear white. Similar to choosing a gate pulse, there are trade-offs and compromises in choosing spectral response functions depending on the plotting purposes.

Movies of Spatiotemporal Pulses

As a first example, Figure 9.5 shows several movie snapshots of a linearly chirped ultrashort pulse. The introduced quadratic phase corresponds to a negative temporal chirp or equivalently a positive spectral chirp. The movie begins orange/red, fades to white, and then to blue. The plotted spectral energy distribution indicates the change of frequency contents across the pulse length – low frequencies occur at early times and high frequencies occur at later times. Of course, we can adjust our emphasis on frequency or temporal resolution with proper gating pulses. Note that, in this case, an instantaneous-frequency-based movie would also show the trend of color change over time and clearly indicated that the pulse is chirped. For this purpose, both plotting schemes should be applicable. The spectrogram-based approach shows, however, that many frequencies are present at the temporal center of the pulse.

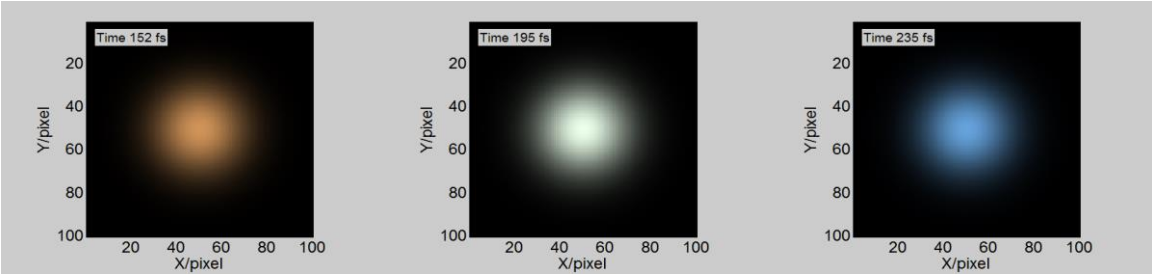

Figure 9.5: Movie snapshots of a linearly chirped pulse. The pulse has duration of 70fs and temporal chirp of -2×10^{-4} fs^{-2}. The pixel size is 10um. See "Figure 9-5 Linearly chirped pulse.gif".

The strength of spectrogram-based plotting is more apparent when considering pulses with more complicated phase structures. Figure 9.6 shows a pulse with pure cubic spectral phase (and no quadratic spectral phase). In the movie, the pulse first appears green; then the green fades while the energy in red and blue increases, reaching a short-lived white equilibrium. After the green is totally gone, the movie becomes purple due to a mixture of red and blue colors, which indicates the simultaneous presence of long and short wavelengths, as is the case for pulses with this distortion. On the other hand, the averaged instantaneous frequency of this pulse is actually constant, so a plot based on

instantaneous frequency would show this pulse as simply being green (the center frequency) at all times, which neglects important phase structure.

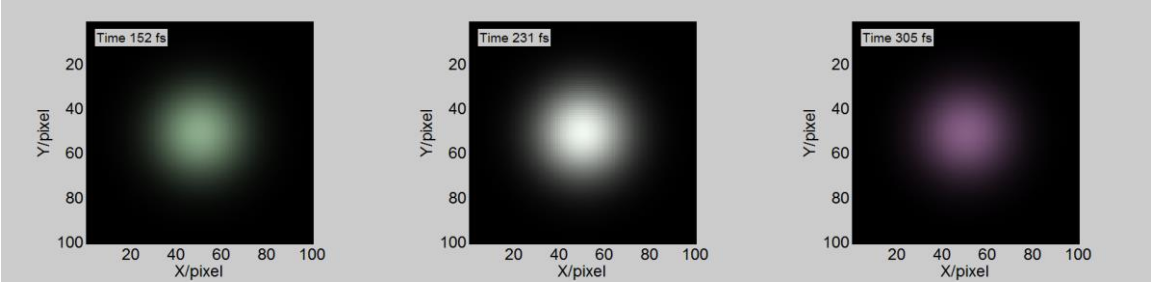

Figure 9.6: Movie snapshots of a pulse with a cubic spectral phase. The pulse has duration of 70fs and cubic spectral phase of 5×10^4 fs^3. See "Figure 9-6 Cubic spectral phase.gif".

This spectrogram plotting method is also able to show pulses with interesting structure in the spatial dimensions. Figure 9.7 shows an interesting waveform consisting of two pulses crossing in space at an angle, experiencing an effect called chirped-pulse beating [87]. If two identically chirped pulses are slightly delayed such that their instantaneous frequencies are different at the same time, they will beat against each other and generate complex spectral structures. For these crossing pulses, the chirped-pulse beating also depends on the spatial location. The horizontal interference fringes, from crossing the beams at a small vertical angle, change color as the chirped pulses evolve.

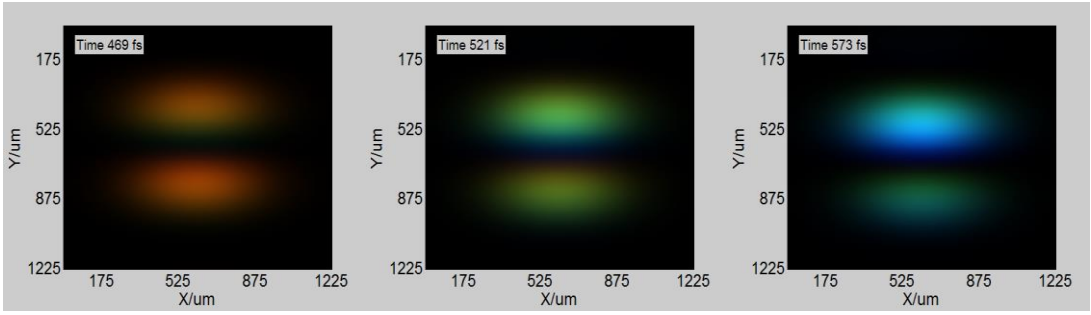

Figure 9.7: Movie snapshots of two delayed positively-chirped pulses crossing at a small vertical angle, from [87]. Chirped-pulse beating behaviors are shown among the fringes. See "Figure 9-7 Chirped pulse beating.gif".

Review of Spatiotemporal Couplings

Next, we investigate a specific class of pulse field effects, known as first-order spatiotemporal couplings. A pulse has a spatiotemporal coupling when its temporal field and spatial field are not separable. Alternatively, we could say that the pulse's temporal profile varies with position (or spatial profile varies with time) [110]. In the presence of spatiotemporal couplings, any integrated measurement method that separately characterizes the pulse's spatial and temporal profile will fail. Spatiotemporal couplings are widely used in laser systems, pulse amplifiers, pulse shaping devices and so on [111-113]. These spatiotemporal couplings further necessitate the development of powerful pulse measurement techniques, and associated plotting methods to display pulses with such complexities.

Among all spatiotemporal couplings, the most commonly observed are the first-order spatiotemporal couplings [112, 114-117]. These couplings can be described by a set of Gaussian equations, in four Fourier-transform-conjugate domains comprised of pairs of dimensions [118]. In these equations, the coupling coefficients are complex, with the real and imaginary parts having different effects on the pulse. The real coefficients are called amplitude coupling terms because they affect energy distribution, and the imaginary parts are called phase coupling term because they affect the phase fronts of the beam.

Starting from the space and time dimensions (in the spatiotemporal domain), the expression for a first-order coupled field is:

$$E(x,t) \propto \exp\{Q_{xx}x^2 + 2Q_{xt}xt - Q_{tt}t^2\} \tag{9.6}$$

For simplicity, we keep our discussion of couplings in x-t dimensions, so there is no need to explicitly write the y-dependence. The real part of Q_{xt} is referred to as the pulse-front tilt, and it can cause the energy in one side of the beam to arrive earlier than the other side. The imaginary part is called the wave-front rotation, which describes how the direction of phase fronts changes with time in the pulse.

We can express the same electric field in terms of different variables by taking the Fourier transform of one or both dimensions. Because Gaussians Fourier-transform to Gaussians, taking the Fourier transform with respect to time leads us to the space-frequency (or spatiospectral) domain, where the field is:

$$E(x,\omega) \propto \exp\{R_{xx}x^2 + 2R_{x\omega}x\omega - R_{\omega\omega}\omega^2\} \tag{9.7}$$

Here, the real part of the coupling term $R_{x\omega}$ is called the spatial chirp, which separates the frequencies in the pulse spatially. The imaginary part causes different frequencies in the pulse to have differently tilted phase fronts, an effect called the wave-front-tilt dispersion. This spatiospectral domain is of particular interest to us, because STRIPED FISH, by measuring the spatial profile at each frequency, measures pulses in this domain. These are the coupling terms that STRIPED FISH can directly measure.

If we instead take one Fourier transform with respect to space instead of time, we obtain an expression in terms of time and spatial frequency. Spatial frequency (or k, a shorthand for the transverse component of the propagation vector $\vec{k}$) is related to the spatial shape of the pulse and the phase front which determines the propagation direction. The field in the k- t domain is then given by:

$$E(k,t) \propto \exp\{P_{kk}k^2 + 2P_{kt}kt - P_{tt}t^2\} \tag{9.8}$$

The real part of P_{kt} is called the time versus angle or the ultrafast lighthouse effect. In energy, it causes early parts of the pulse to propagate in a different direction from the latter parts. The imaginary part of P_{kt}, referred to as the angular temporal chirp, is somewhat less intuitive. It means that different propagation directions have different relative phases as time evolves.

The fourth domain is the frequency and spatial frequency domain. In this domain, the electric field is:

$$E(k,\omega) \propto \exp\{S_{kk}k^2 + 2S_{k\omega}k\omega - S_{\omega\omega}\omega^2\} \tag{9.9}$$

The amplitude coupling between frequency and spatial frequency is angular dispersion, a well-known effect produced by prisms and other optics. Different frequencies propagate in different directions. The phase coupling term, called the angular spectral chirp, is less well-known. This term causes different propagation directions to gain different relative phases for different frequencies.

Since all of these domains are inter-related by Fourier transforms, a coupling in any of these domains generally means that there are related couplings in other domains. Given the field expression in one particular domain (e.g. the spatiospectral domain for STRIPED FISH), one can determine its variants in all other neighboring domains. In most experiments, pulse amplitude couplings are more observable. In the following, we show some example pulses with such amplitude couplings.

Movies of Spatiotemporal Couplings

When pulse-front tilt is present, different parts of the pulse arrive at one transverse plane at different times. The pulse arrival time depends linearly on the position of consideration. As shown in Figure 9.8, the right part of the pulse arrives earlier than the left part. And the non-chirped pulse appears white at all times, which implies that all frequencies are coincident along the time axis.

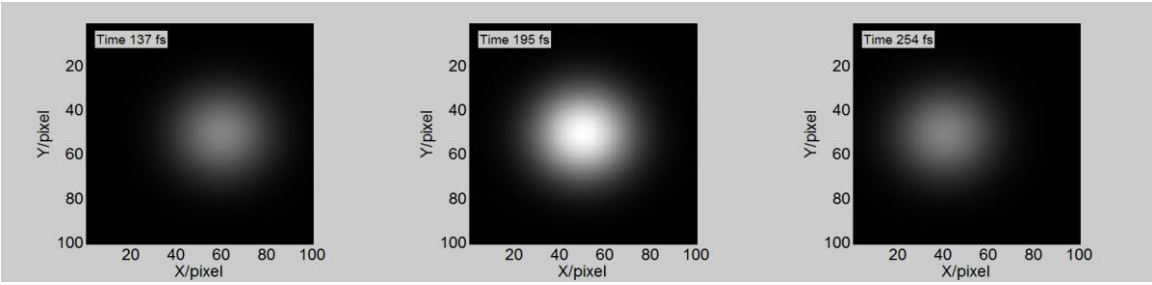

Figure 9.8. Movie snapshots of a pulse with pulse front tilt (40fs/mm) and no temporal/spectral chirp. See “Figure 9-8 Pulse front tilt.mp4”.

Figure 9.9 demonstrates spatial chirp. In a pulse with a constant spatial chirp, each frequency component will shift linearly in space. In the movie, because no temporal/spectral chirp is present in the pulse, all frequency components arrive at the

same time. But their positions differ from red on the left, to white in the middle (all frequencies are present and overlap), to blue on the right. The movie clearly demonstrates the effects of spatial chirp on the pulse.

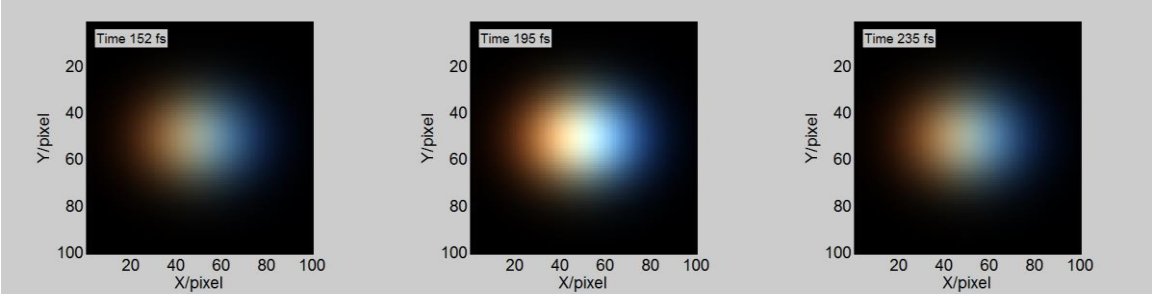

Figure 9.9: Movie snapshots of a pulse with spatial chirp (21fs/mm) and no temporal/spectral chirp. See "Figure 9-9 Spatial chirp.mp4".

These movies show the distribution of spectral energy in time and space, which means that pulse-front tilt and spatial chirp can be clearly displayed. As mentioned above, there are two other amplitude coupling terms, angular dispersion and time vs. angle. Unfortunately, since these movies exist in one single *z*-plane, couplings involving angular variations are impossible to display well. As a result, a movie of angular dispersion will look very similar to a movie of spatial chirp, and time vs. angle will hardly be differentiated from pulse-front tilt.

The four phase coupling terms, wave-front rotation, wave-front-tilt dispersion, angular temporal chirp and angular spectral chirp, are much less well-known. This is partly because the phase couplings are typically more difficult to observe than the amplitude couplings with intensity-sensitive detectors. While STRIPED FISH is capable of measuring all these coupling effects, additional improvements to the plotting method will be required to clearly differentiate and display these ultrashort pulse characteristics.

Limitations in this Plotting Approach

Although the spectrogram-based RGB plotting is an intuitive method for displaying the spatiotemporal field variations, it does possess some limitations. The

problem with the current approach is that because the movie is generated at one particular z-plane, the movie does not address angular effects well. The generated movie does not show the pulse propagation direction (or the wave front of the field), which can cause ambiguities in the display. The simplest example is a focusing pulse with non-zero wave-front curvature, which just yields the same movie as that of a well-collimated pulse. As a result, it is also not possible to distinguish the angular properties of first-order spatiotemporal couplings using the current plotting approach. Spatial chirp and angular dispersion can look identical if we only observe the field at only one z-plane. Clearly, the current plotting approach does not fully display all the information that is measured by STRIPED FISH and potentially could be of interest.

Additionally, the choice of time gate function and parameters requires some care. For a given signal field, the plotted result is not unique, as different choices of gate functions can lead to very different the appearance of movies. Further, even for the same gate function, a different choice of spectral response functions will make the resulting movie differ, as discussed. All these parameters should be tailored to illuminate the pertinent effects in a specific pulse measurement case.

Conclusions

In conclusion, we have discussed the challenges associated with displaying multidimensional characteristics of electromagnetic fields of ultrashort pulses. Because such pulses possess intensity and phase characteristics as a function of time and space and in general have couplings between the spatial and temporal dimensions, a powerful method for displaying such interesting and complex signals is desirable. Previous efforts to display such pulses were subject to ambiguities in the local spectral energy distribution, due to the use of instantaneous frequency plotting values. We solved this problem by calculating a numerically generated spectrogram of the data. This spectrogram is integrated with three separate response functions $R(\omega)$, $G(\omega)$, and $B(\omega)$,

reminiscent of the spectral response functions of the S, M, and L cone receptors in the human eye. The values acquired from each of these spectrogram integrals are assigned to R, G, and B functions, respectively, and a color movie is generated following this RGB representation. This method of displaying ultrashort pulses offers key advantages in the representation of the spectral energy content as a function of space and time, thereby overcoming the ambiguities encountered by previous methods. We have provided sample data movies using our spectrogram-based RGB plotting method. Additionally, we summarized first-order couplings between space and time (and their respective frequency domains) and displayed how our technique can plot these effects as well. We reiterate that the choice of parameters, such as temporal gate function used in generating the spectrogram, the distribution functions used for $R(\omega)$, $G(\omega)$, and $B(\omega)$, and the choice of which dimensional quantities to display allows for versatility in the presentation of complex pulse fields. Multiple plots with sets of varying display parameters could be used in clearly conveying the information for most complicated pulses, addressing different perspectives of the measured field.

CHAPTER 10

PLOTTING THE PROPAGATION OF SPATIOTEMPORALLY COMPLEX PULSES

The previous chapter described the limitations of the spectrogram-based movies for displaying effects such as focusing and angular dispersion. Because these movies are limited to showing only one z-plane, they cannot display the pulse wavefronts or show differences in propagation direction. Since the spatial phase of these pulses can be measured and the electric field is therefore completely known, the natural solution is to use diffraction integrals to calculate the electric field at other z-planes. Plotting the evolution of pulses will allow us to display spatiotemporal couplings involving their propagation direction. In conjunction with the spectrogram-based encoding of the temporal/spectral phase, we will be able to clearly show interesting spatiotemporal distortions.

Angular Spectrum Propagation

I chose to use the Angular Spectrum description of diffraction [119, 120], which has been shown to be equivalent to the first Rayleigh-Sommerfeld solution [121]. After computing the two-dimensional spatial Fourier transform of the original electric field, the field at any z-plane is given simply by:

$$E(k_x, k_y, \omega, z) = E\left(k_x, k_y, \omega, 0\right) \exp\left(iz\sqrt{\frac{\omega^2}{c^2} - k_x^2 - k_y^2}\right) \tag{10.1}$$

where k_x and k_y are the spatial frequencies or off-axis k-vectors in the x and y dimensions. Using this model, propagation is described as a simple transfer function. $E(x, y, t, z)$ is easily determined for plotting purposes by three Fourier transforms. This method has the huge advantage of allowing us to leverage fast Fourier transforms to

avoid computationally laborious integrals. We also compute the field at an entire z-plane in one multiplication, rather than having to calculate the signal at each point in the desired z-plane, as would be required using the original Rayleigh-Sommerfeld formulas.

Issues with Angular Spectrum Propagation

While propagating pulses analytically using the angular spectrum causes no problems, doing so in a discrete computation generates errors for large propagation distances. The source of these errors is poor sampling of the propagation transfer function. As z and k increase, the complex transfer function oscillates more and more quickly (see Fig. 10.1). Past a certain limit, the transfer function becomes aliased and generates errors for large spatial frequencies. This limit is labeled as k_{max} in Figure 10.1. Even though the rate of variation of the transfer function continues to increase with k past the limit k_{max}, aliasing of the transfer function causes it to appear otherwise.

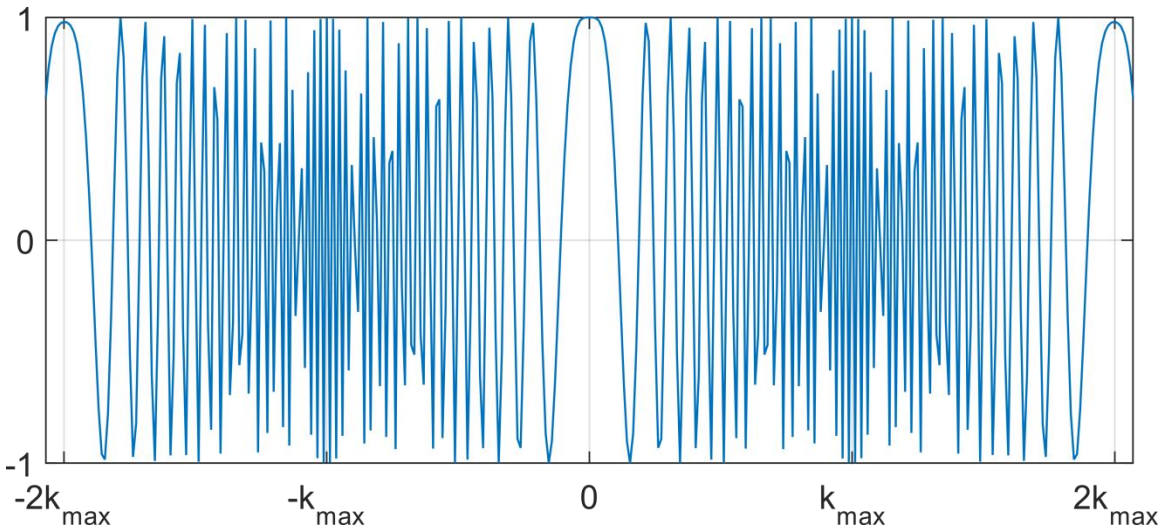

Figure 10.1: Real part of the angular spectrum propagation transfer function in one dimension for a large z. k_{max} is the largest k for which no aliasing occurs.

The limit k_{max} is determined by the Nyquist theorem [122]. Any frequencies above k_{max} introduce errors into the propagated field. The limit is calculated as:

$$k_{max} = \left(\lambda\sqrt{(2\Delta kz)^2 + 1}\right)^{-1} \tag{10.2}$$

where λ is the wavelength of the light and Δk is the spatial frequency sampling. The frequency sampling is of course related to the size of the spatial grid. Using a larger spatial grid will decrease Δk and increase k_{max}.

In order to prevent aliasing from introducing errors into the propagated field, I simply zero out the transfer function for values of k_x and k_y above k_{max} (as suggested by Ref [122]). I also take the additional step of checking how many discrete points lay between $-k_{max}$ and k_{max}. If too few points are in the non-zero region, I expand the spatial grid to increase the spatial frequency sampling. These steps have been sufficient to prevent errors over the small distances of interest to us.

Displaying Electric Fields in 3D

I display the electric fields by plotting several translucent surfaces of constant intensity (see Fig. 10.2). These surfaces are colored using the spectrogram-based coloring routine described in Chapter 9. This has the effect of making the brightest part of the pulse more solid and brightly colored. I also include projections of the pulse to the x-z and y-z planes, which can be helpful in understanding the structure of complicated pulses as well as noisy data.

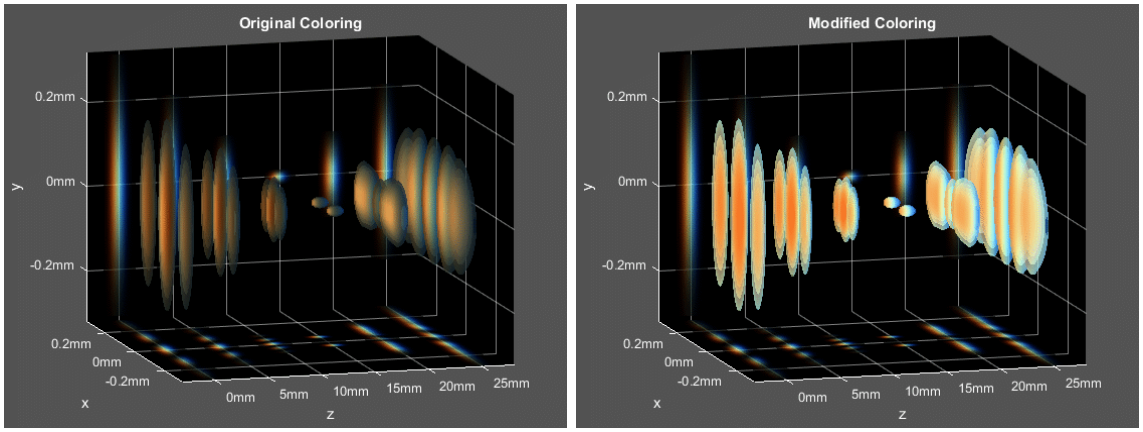

Figure 10.2: Negatively chirped, focusing pulses crossing in space shown with original (left) and modified (right) coloring schemes.

In order to show the shape of the outer edges of the pulse, it is necessary to plot some of the surfaces of constant intensity where the pulse intensity is low. Unfortunately, because the spectrogram-based coloring routine naturally makes areas of zero intensity black, low-intensity parts of the pulse are quite dark (see Fig. 10.2). This generally interferes with being able to see other parts of the pulse. Because of this effect, the coloring routine must be adjusted for 3D plotting by renormalizing the color of pixels. The surfaces of constant intensity provide an indicator of relative intensity, so mapping intensity to brightness is no longer necessary to understand the field. To preserve colors, each pixel gets the highest of the R, G, or B values boosted to the maximum value, and the other colors are multiplied by the same factor.

Plotting Spatial Chirp and Angular Dispersion

As discussed in the last chapter, some spatiotemporal distortions are difficult to tell apart if viewed in only a single *z*-plane. Two such distortions (spatial chirp and angular dispersion) are plotted in Figure 10.3. For these simulations, I start with a defocusing Gaussian pulse in space and time with the appropriate spatiotemporal distortion. This field is then propagated numerically. While the local field in some planes

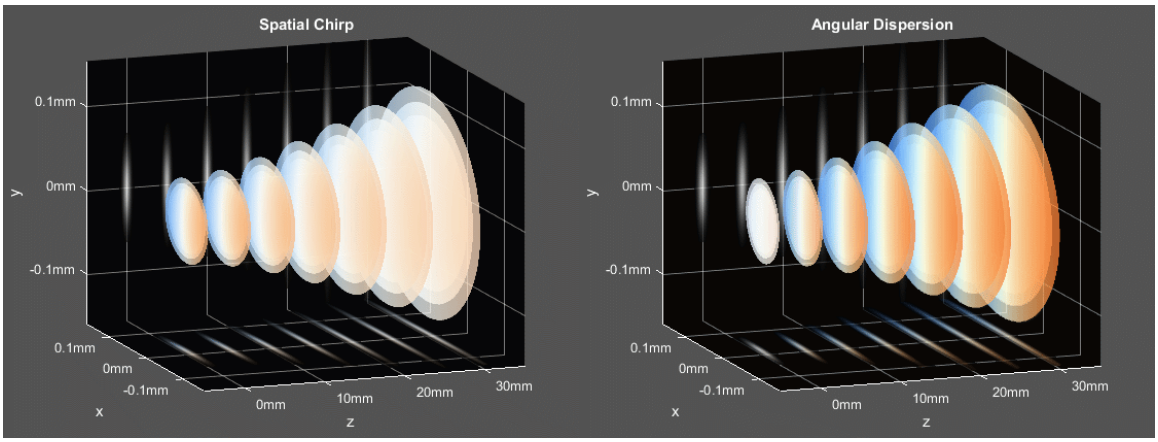

Figure 10.3: Spatial chirp and angular dispersion in a simulated defocusing pulse. See "Figure 10-3 Spatial chirp propagation.mp4" and "Figure 10-3 Angular dispersion propataion.mp4"

is very similar for spatial chirp and angular dispersion, the overall evolution of these two pulses is quite different. The inclusion of several z-planes makes it much easier to understand the electric field.

It is important to keep in mind that the first-order spatiotemporal distortions are not independent from each other. As an example, the plot of angular dispersion shows that the spatial chirp of the pulse increases with propagation distance. A close inspection of the associated movie reveals some pulse-front tilt. Because angular dispersion, spatial chirp, and pulse-front tilt are associated with different pairs of coordinates (k-ω, x-ω, and x-t respectively), a pulse with a distortion in one domain will generally have distortions in all domains. The relative strengths of these distortions depend on many pulse parameters. Nevertheless, it is often helpful to discuss the primary, intended coupling while noting the other distortions that result from it.

Plotting Measured Data

Of course, this type of plotting is most helpful for measured data that is more difficult to visualize. Figure 10.4 shows a pulse measured with STRIPED FISH whose primary coupling is time vs angle (k-t coupling known as "the ultrafast lighthouse effect"). Couplings involving k are particularly difficult to plot using other methods. To create this pulse, we induced pulse-front tilt (x-t coupling) using a prism pair, and the pulse was then focused. Because pulse-front tilt cases the pulse energy to arrive earlier on one side of the beam than the other, focusing this pulse causes the direction of propagation of beam to change with time. This distortion can also be understood by noting that focusing a beam performs a spatial Fourier transform. The focusing lens transforms a coupling between x and t into a coupling between k and t.

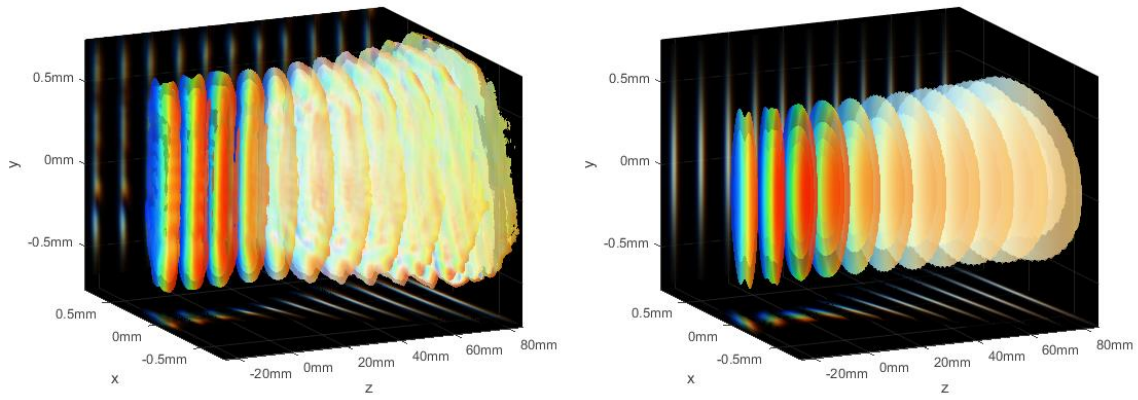

Figure 10.4: Plot of a pulse with time vs angle. The focus of the beam is located at $z = 0$. Left: measured data from STRIPED FISH. Right: simulation of this pulse. See "Figure 10-4 Lighthouse measured data.mp4" and "Figure 10-4 Lighthouse simulated pulse.mp4".

A simulation of this pulse is also shown to demonstrate that its distortions are well-understood. The simulated field was defined at the focusing lens, 150mm before the focus (the focus is defined as $z = 0$), using the measured spectrum and spectral phase. In this case, the STRIPED FISH measurement was taken 85mm after the focus and the measured field was back-propagated. The excellent agreement between these two plots gives us great confidence in the measurement and in the propagation code. (I highly recommend watching the movies associated with these plots.) Despite the small local color variations in the plot of the measured data, the two plots share some very distinct spatio-spectral structure around the pulse focus. The pulse at the focus shows extreme spatial chirp. It is also interesting to note the change in the direction of pulse-front tilt before and after the focus.

Summary

I have implemented diffraction using the angular spectrum method to plot the evolution of ultrashort pulses in space. Combining this information with the spectrogram-based color plotting from the previous chapter gives us a robust and informative way of plotting ultrashort pulses, particularly those with interesting spatial structure and/or

spatiotemporal couplings. This plotting method is demonstrated using the measured electric field of a complex pulse with time vs angle. This spatiotemporal distortion is not easily displayed with other methods. We obtain excellent agreement with a simulated pulse, giving us confidence in both the plotting and in the measurement.

REFERENCES

1. J. A. Giordmaine, P. M. Rentzepis, S. L. Shapiro, and K. W. Wecht, "Two-photon excitation of fluorescence by picosecond light pulses," Applied Physics Letters **11**(7), 216-218 (1967).

2. J. A. Armstrong, "Measurement of picosecond laser pulse widths," Applied Physics Letters **10**(1), 16-18 (1967).

3. H. P. Weber, "Method for Pulsewidth Measurement of Ultrashort Light Pulses Generated by Phase-Locked Lasers using Nonlinear Optics," Journal of Applied Physics **38**(5), 2231-2234 (1967).

4. M. A. Duguay, S. L. Shapiro, and P. M. Rentzepis, "Spontaneous Appearance of Picosecond Pulses in Ruby and Nd: Glass Lasers," Physical Review Letters **19**(18), 1014-1016 (1967).

5. S. L. Shapiro, M. A. Duguay, and L. B. Kreuzer, "Picosecond substructure of laser spikes," Applied Physics Letters **12**(2), 36-37 (1968).

6. M. Bass and D. Woodward, "Observation of picosecond pulses from a Nd:YAG laser," Applied Physics Letters **12**(8), 275-277 (1968).

7. H. P. Weber, "Comments on the pulse width measurement with two-photon excitation of fluorescence," Physics Letters A **27**(5), 321-322 (1968).

8. J. R. Klauder, M. A. Duguay, J. A. Giordmaine, and S. L. Shapiro, "Correlation effects in the display of picosecond pulses by two-photon techniques," Applied Physics Letters **13**(5), 174-176 (1968).

9. R. H. Brown and R. Q. Twiss, "Correlation between Photons in two Coherent Beams of Light," Nature **177**(4497), 27-29 (1956).

10. R. H. Brown and R. Q. Twiss, "Interferometry of the Intensity Fluctuations in Light. I. Basic Theory: The Correlation between Photons in Coherent Beams of Radiation," Proceedings of the Royal Society of London. Series A. Mathematical and Physical Sciences **242**(1230), 300-324 (1957).

11. R. J. Glauber, "Coherent and Incoherent States of the Radiation Field," Physical Review **131**(6), 2766-2788 (1963).

12. L. Mandel and E. Wolf, "Coherence Properties of Optical Fields," Reviews of Modern Physics **37**(2), 231-287 (1965).

13. H. Weber and R. Dandliker, "Intensity interferometry by two-photon excitation of fluorescence," Quantum Electronics, IEEE Journal of **4**(12), 1009-1013 (1968).

14. M. Duguay, J. Hansen, and S. Shapiro, "Study of the Nd: Glass laser radiation," Quantum Electronics, IEEE Journal of **6**(11), 725-743 (1970).

15. H. Rowe and L. Tingye, "Theory of two-photon measurement of laser output," Quantum Electronics, IEEE Journal of **6**(1), 49-67 (1970).

16. E. Ippen and C. Shank, "Techniques for measurement; Ultrashort Light Pulses," S. Shapiro, ed. (Springer Berlin / Heidelberg, 1984), pp. 83-122.

17. D. J. Bradley and G. H. C. New, "Ultrashort pulse measurements," Proceedings of the IEEE **62**(3), 313-345 (1974).

18. R. J. Harrach, "Effects of partial mode-locking on contrast ratios in two-photon excitation of fluorescence," Physics Letters A **28**(6), 393-394 (1968).

19. R. J. Harrach, "Determination of ultrashort pulse widths by two-photon fluorescence patterns," Applied Physics Letters **14**(5), 148-151 (1969).

20. S. K. Kurtz and S. L. Shapiro, "Two photon fluorescence displays with a non-mode-locked Nd:YAG laser," Physics Letters A **28**(1), 17-18 (1968).

21. S. L. Shapiro and M. A. Duguay, "Observation of subpicosecond components in the mode-locked Nd:glass laser," Physics Letters A **28**(10), 698-699 (1969).

22. A. A. Grütter, H. P. Weber, and R. Dändliker, "Imperfectly Mode-Locked Laser Emission and Its Effects on Nonlinear Optics," Physical Review **185**(2), 629-643 (1969).

23. R. H. Picard and P. Schweitzer, "Theory of Intensity-Correlation Measurements on Imperfectly Mode-Locked Lasers," Physical Review A **1**(6), 1803-1818 (1970).

24. J. Herrmann, M. Palme, and K. E. Süsse, "The influence of phase fluctuations and phase modulation on two-photon fluorescence," Optical and Quantum Electronics **10**(3), 195-203 (1978).

25. Z. Fried, "On the structure of picosecond pulses," Physics Letters A **33**(2), 62-63 (1970).

26. W. H. Glenn and M. J. Brienza, "Time evolution of picosecond optical pulses," Applied Physics Letters **10**(8), 221-224 (1967).

27. H. A. Pike and M. Hercher, "Basis for Picosecond Structure in Mode-Locked Laser Pulses," Journal of Applied Physics **41**(11), 4562-4565 (1970).

28. R. Dandliker, A. Grutter, and H. Weber, "Statistical amplitude and phase variations in mode-locked lasers," Quantum Electronics, IEEE Journal of **6**(11), 687-693 (1970).

29. E. B. Treacy, "Measurement of picosecond pulse substrucure using compression techniques," Applied Physics Letters **14**(3), 112-114 (1969).

30. E. B. Treacy, "Compression of picosecond light pulses," Physics Letters A **28**(1), 34-35 (1968).

31. R. A. Fisher and J. J. A. Fleck, "On the phase characteristics and compression of picosecond light pulses," Applied Physics Letters **15**(9), 287-290 (1969).

32. J. Ratner, G. Steinmeyer, T. C. Wong, R. Bartels, and R. Trebino, "Coherent artifact in modern pulse measurements," Opt. Lett. **37**(14), 2874-2876 (2012).

33. E. P. Ippen and C. V. Shank, "Dynamic spectroscopy and subpicosecond pulse compression," Applied Physics Letters **27**(9), 488-490 (1975).

34. R. K. Jain and C. P. Ausschnitt, "Subpicosecond pulse generation in a synchronously mode-locked cw rhodamine 6G dye laser," Opt. Lett. **2**(5), 117-119 (1978).

35. C. P. Ausschnitt and R. K. Jain, "Pulse-width dependence on intracavity bandwidth in synchronously mode-locked cw dye lasers," Applied Physics Letters **32**(11), 727-730 (1978).

36. J. P. Heritage and R. K. Jain, "Subpicosecond pulses from a tunable cw mode-locked dye laser," Applied Physics Letters **32**(2), 101-103 (1978).

37. E. W. Van Stryland, "The effect of pulse to pulse variation on ultrashort pulsewidth measurements," Optics Communications **31**(1), 93-96 (1979).

38. A. Birmontas, R. Kupris, A. Piskarskas, V. Smil'gyavichyus, and A. Stabinis, "Determination of the duration of fluctuating picosecond optical pulses," Soviet Journal of Quantum Electronics **12**(6), 792-794 (1982).

39. J. Catherall and G. New, "Role of spontaneous emission in the dynamics of mode locking by synchronous pumping," Quantum Electronics, IEEE Journal of **22**(9), 1593-1599 (1986).

40. J. Q. Bi, W. Hodel, and H. P. Weber, "Numerical simulation of coherent photon seeding: A new technique to stabilize synchronously pumped mode-locked lasers," Optics Communications **81**(6), 408-418 (1991).

41. E. J. Akutowicz, "On the determination of the phase of a Fourier integral. I," Trans. Am. Math. Soc. **83**, 234-239 (1956).

42. R. Trebino, E. K. Gustafson, and A. E. Siegman, "Fourth-order partial-coherence effects in the formation of integrated-intensity gratings with pulsed light sources," J. Opt. Soc. Am. B **3**(10), 1295-1304 (1986).

43. R. Trebino, *Frequency-Resolved Optical Gating: The Measurement of Ultrashort Laser Pulses* (Kluwer Academic Publishers, 2002).

44. X. Gu, L. Xu, M. Kimmel, E. Zeek, P. O'Shea, A. P. Shreenath, R. Trebino, and R. S. Windeler, "Frequency-resolved optical gating and single-shot spectral measurements reveal fine structure in microstructure-fiber continuum," Opt. Lett. **27**(13), 1174-1176 (2002).

45. B. Schenkel, R. Paschotta, and U. Keller, "Pulse compression with supercontinuum generation in microstructure fibers," J. Opt. Soc. Am. B **22**(3), 687-693 (2005).

46. G. Genty, S. Coen, and J. M. Dudley, "Fiber supercontinuum sources (Invited)," J. Opt. Soc. Am. B **24**(8), 1771-1785 (2007).

47. F. Mitschke, G. Steinmeyer, and A. Schwache, "Generation of one-dimensional optical turbulence," Physica D: Nonlinear Phenomena **96**(1–4), 251-258 (1996).

48. C. Brée, A. Demircan, and G. Steinmeyer, "Modulation instability in filamentary self-compression," Laser Physics **21**(7), 1313-1318 (2011).

49. A. Hideur, T. Chartier, M. Brunel, S. Louis, C. Özkul, and F. Sanchez, "Generation of high energy femtosecond pulses from a side-pumped Yb-doped double-clad fiber laser," Applied Physics Letters **79**, 3389-3391 (2001).

50. J. D. Kafka, T. Baer, and D. W. Hall, "Mode-locked erbium-doped fiber laser with soliton pulse shaping," Optics Letters **14**, 1269-1271 (1989).

51. G. Stibenz and G. Steinmeyer, "High dynamic range characterization of ultrabroadband while-light continuum pulses," Optics Express **12**, 6319-6325 (2004).

52. T. M. Fortier, J. Ye, S. T. Cundiff, and R. S. Windeler, "Nonlinear phase noise generated in air-silica microstructure fiber and its effect on carrier-envelope phase," Optics Letters **27**, 445-447 (2002).

53. L. Xu, C. Spielmann, A. Poppe, T. Brabec, F. Krausz, and T. W. Hänsch, "Route to phase control of ultrashort light pulses," Optics Letters **21**, 2008-2010 (1996).

54. K. Osvay, M. Görbe, C. Grebing, and G. Steinmeyer, "Bandwidth-independent linear method for detection of the carrier-envelope offset phase," Optics Letters **32**, 3095-3097 (2007).

55. H. R. Telle, G. Steinmeyer, A. E. Dunlop, J. Stenger, D. H. Sutter, and U. Keller, Appl. Phys. B **69**, 327-332 (1999).

56. H. A. Haus and A. Mecozzi, "Noise of Mode-Locked Lasers," IEEE J. Quantum Electron. **29**, 983-996 (1993).

57. D. von der Linde, "Characterization of the noise in continuously operating mode-locked lasers," Applied Physics B **39**, 201-217 (1986).

58. M. Rhodes, G. Steinmeyer, J. Ratner, and R. Trebino, "Pulse-shape instabilities and their measurement," Laser & Photonics Reviews **7**(4), 557-565 (2013).

59. J. M. Dudley, G. Genty, and S. Coen, "Supercontinuum generation in photonic crystal fiber," Reviews of Modern Physics **78**, 1135-1184 (2006).

60. D. J. Kane and R. Trebino, "Single-shot measurement of the intensity and phase of an arbitrary ultrashort pulse by using frequency-resolved optical gating," Optics Letters **18**(10), 823-825 (1993).

61. K. W. DeLong, B. Kohler, K. Wilson, D. N. Fittinghoff, and R. Trebino, "Pulse retrieval in frequency-resolved optical gating based on the method of generalized projections," Optics Letters **19**(24), 2152-2154 (1994).

62. L. Xu, E. Zeek, and R. Trebino, "Simulations of frequency-resolved optical gating for measuring very complex pulses," J. Opt. Soc. Am. B **25**(6), A70-A80 (2008).

63. R. P. Scott, N. K. Fontaine, J. Cao, K. Okamoto, B. H. Kolner, J. P. Heritage, and S. J. B. Yoo, "High-fidelity line-by-line optical waveform generation and complete characterization using FROG," Opt. Express **15**(16), 9977-9988 (2007).

64. C. Iaconis and I. A. Walmsley, "Spectral phase interferometry for direct electric-field reconstruction of ultrashort optical pulses," Opt. Lett. **23**(10), 792-794 (1998).

65. M. Rhodes, M. Mukhopadhyay, J. Birge, and R. Trebino, "Coherent artifact study of two-dimensional spectral shearing interferometry," JOSA B **32**(9), 1881-1888 (2015).

66. M. Takeda, H. Ina, and S. Kobayashi, "Fourier-transform method of fringe-pattern analysis for computer-based topography and interferometry," J. Opt. Soc. Am. **72**(1), 156-160 (1982).

67. M. Lederer, B. Luther-Davies, H. Tan, C. Jagadish, N. Akhmediev, and J. Soto-Crespo, "Multipulse operation of a Ti: sapphire laser mode locked by an ion-implanted semiconductor saturable-absorber mirror," JOSA B **16**(6), 895-904 (1999).

68. J. R. Birge, R. Ell, and F. X. Kärtner, "Two-dimensional spectral shearing interferometry for few-cycle pulse characterization," Opt. Lett. **31**(13), 2063-2065 (2006).

69. J. R. Birge and F. X. Kärtner, "Analysis and mitigation of systematic errors in spectral shearing interferometry of pulses approaching the single-cycle limit [Invited]," J. Opt. Soc. Am. B **25**(6), A111-A119 (2008).

70. E. M. Kosik, A. S. Radunsky, I. A. Walmsley, and C. Dorrer, "Interferometric technique for measuring broadband ultrashort pulses at the sampling limit," Optics Letters **30**(3), 326-328 (2005).

71. D. R. Austin, T. Witting, and I. A. Walmsley, "High precision self-referenced phase retrieval of complex pulses with multiple-shearing spectral interferometry," J. Opt. Soc. Am. B **26**(9), 1818-1830 (2009).

72. T. Oksenhendler, S. Coudreau, N. Forget, V. Crozatier, S. Grabielle, R. Herzog, O. Gobert, and D. Kaplan, "Self-referenced spectral interferometry," Applied Physics B: Lasers and Optics **99**(1), 7-12 (2010).

73. C. Froehly, A. Lacourt, and J. C. Vienot, "Notions de réponse impulsionnelle et de fonction de transfert temporelles des pupilles optiques, justifications expérimentales et applications," Nouv. Rev. Opt **4**, 183-196 (1973).

74. A. Jullien, L. Canova, O. Albert, D. Boschetto, L. Antonucci, Y. H. Cha, J. P. Rousseau, P. Chaudet, G. Chériaux, J. Etchepare, S. Kourtev, N. Minkovski, and S. M. Saltiel, "Spectral broadening and pulse duration reduction during cross-polarized wave generation: influence of the quadratic spectral phase," Applied Physics B: Lasers and Optics **87**(4), 595-601 (2007).

75. L. Lepetit, G. Chériaux, and M. Joffre, "Linear techniques of phase measurement by femtosecond spectral interferometry for applications in spectroscopy," J. Opt. Soc. Am. B **12**(12), 2467-2474 (1995).

76. A. Moulet, S. Grabielle, C. Cornaggia, N. Forget, and T. Oksenhendler, "Single-shot, high-dynamic-range measurement of sub-15 fs pulses by self-referenced spectral interferometry," Opt. Lett. **35**(22), 3856-3858 (2010).

77. T. Oksenhendler, S. Coudreau, N. Forget, V. Crozatier, S. Grabielle, R. Herzog, O. Gobert, and D. Kaplan, "Self-referenced spectral interferometry," Applied Physics B **99**(1-2), 7-12 (2010).

78. T. Oksenhendler, "Self-referenced spectral interferometry theory," arXiv preprint arXiv:1204.4949 (2012).

79. S. Grabielle, A. Moulet, N. Forget, V. Crozatier, S. Coudreau, O. Gobert, C. Cornaggia, and T. Oksenhendler, "Sub-12 fs pulses characterization by self-referenced spectral interferometry," presented at the Lasers and Electro-Optics (CLEO), 2011 Conference on, 1-6 May 2011, 2011.

80. M. Rhodes, G. Steinmeyer, and R. Trebino, "Standards for ultrashort-laser-pulse-measurement techniques and their consideration for self-referenced spectral interferometry [Invited]," Applied Optics **53**(16), D1-D11 (2014).

81. V. V. Lozovoy, I. Pastirk, and M. Dantus, "Multiphoton intrapulse interference. IV. Ultrashort laser pulse spectral phase characterization and compensation," Optics Letters **29**(7), 775-777 (2004).

82. Y. Coello, V. V. Lozovoy, T. C. Gunaratne, B. Xu, I. Borukhovich, C.-h. Tseng, T. Weinacht, and M. Dantus, "Interference without an interferometer: a different approach to measuring, compressing, and shaping ultrashort laser pulses," JOSA B **25**(6), A140-A150 (2008).

83. A. Comin, R. Ciesielski, N. Coca-López, and A. Hartschuh, "Phase retrieval of ultrashort laser pulses using a MIIPS algorithm," Optics Express **24**(3), 2505-2512 (2016).

84. V. V. Lozovoy, G. Rasskazov, D. Pestov, and M. Dantus, "Quantifying noise in ultrafast laser sources and its effect on nonlinear applications," Optics Express **23**(9), 12037-12044 (2015).

85. G. Rasskazov, V. V. Lozovoy, and M. Dantus, "Spectral amplitude and phase noise characterization of titanium-sapphire lasers," Optics Express **23**(18), 23597-23602 (2015).

86. S. Akturk, X. Gu, P. Bowlan, and R. Trebino, "Spatio-temporal couplings in ultrashort laser pulses," Journal of Optics **12**, 093001 (2010).

87. Z. Guang, M. Rhodes, M. Davis, and R. Trebino, "Complete characterization of a spatiotemporally complex pulse by an improved single-frame pulse-measurement technique," JOSA B **31**(11), 2736-2743 (2014).

88. P. Bowlan, P. Gabolde, A. Shreenath, K. McGresham, R. Trebino, and S. Akturk, "Crossed-beam spectral interferometry: a simple, high-spectral-resolution method for completely characterizing complex ultrashort pulses in real time," Opt. Expr. **14**(24), 11892 (2006).

89. P. Bowlan, P. Gabolde, and R. Trebino, "Directly measuring the spatio-temporal electric field of focusing ultrashort pulses," Opt. Expr. **15**, 10219-10230 (2007).

90. Z. Guang and R. Trebino, "Complete Spatiotemporal Measurement of Ultrashort Pulses Emerging from Multi-mode Optical Fiber," presented at the CLEO: Science and Innovations, 2015.

91. P. Gabolde and R. Trebino, "Single-frame measurement of the complete spatio-temporal intensity and phase of ultrashort laser pulse(s) using wavelength-multiplexed digital holography," J. Opt. Soc. Am. B **25**(6), A25-A33 (2008).

92. D. J. McCabe, A. Tajalli, D. R. Austin, P. Bondareff, I. A. Walmsley, S. Gigan, and B. Chatel, "Spatio-temporal focusing of an ultrafast pulse through a multiply scattering medium," Nature Communications **2**, 447 (2011).

93. Z. Guang, M. Rhodes, and R. Trebino, "Simple single-shot complete spatiotemporal characterization of the intensity and phase of a complex ultrashort pulse," presented at the SPIE LASE, 2015.

94. Y. Vidne and M. Rosenbluh, "Spatial modes in a PCF fiber generated continuum," Optics express **13**(24), 9721-9728 (2005).

95. A. Braun, G. Korn, X. Liu, D. Du, J. Squier, and G. Mourou, "Self-channeling of high-peak-power femtosecond laser pulses in air," Optics Letters **20**(1), 73-75 (1995).

96. M. Born and E. Wolf, *Principles of optics: electromagnetic theory of propagation, interference and diffraction of light* (Cambridge university press, 1999).

97. J. W. Goodman, *Introduction to Fourier optics* (McGraw-hill New York, 1968), Vol. 2.

98. A. E. Siegman, "Lasers. Mill Valley," (University Science Books, 1986).

99. W. Amir, T. A. Planchon, C. G. Durfee, J. A. Squier, P. Gabolde, R. Trebino, and M. Müller, "Simultaneous visualization of spatial and chromatic aberrations by 2D Fourier Transform Spectral Interferometry," Opt. Lett. **31**(19), 2927 (2006).

100. F. Bragheri, D. Faccio, F. Bonaretti, A. Lotti, M. Clerici, O. Jedrkiewicz, C. Liberale, S. Henin, L. Tartara, and V. Degiorgio, "Complete retrieval of the field of ultrashort optical pulses using the angle-frequency spectrum," Optics Letters **33**(24), 2952-2954 (2008).

101. R. Trebino, K. W. DeLong, D. N. Fittinghoff, J. N. Sweetser, M. A. Krumbügel, B. A. Richman, and D. J. Kane, "Measuring ultrashort laser pulses in the time-frequency domain using frequency-resolved optical gating," Review of Scientific Instruments **68**(9), 3277-3295 (1997).

102. W. Koenig, H. Dunn, and L. Lacy, "The sound spectrograph," The Journal of the Acoustical Society of America **18**(1), 19-49 (1946).

103. W. D. Mark, "Spectral analysis of the convolution and filtering of non-stationary stochastic processes," Journal of Sound and Vibration **11**(1), 19-63 (1970).

104. M. D. Fairchild, *Color appearance models* (John Wiley & Sons, 2013).

105. S. G. Solomon and P. Lennie, "The machinery of colour vision," Nature Reviews Neuroscience **8**(4), 276-286 (2007).

106. S. Lee Guth, "Model for color vision and light adaptation," JOSA A **8**(6), 976-993 (1991).

107. W. Rushton, "Review lecture. Pigments and signals in colour vision," The Journal of physiology **220**(3), 1-31 (1972).

108. G. Brindley, J. Du Croz, and W. Rushton, "The flicker fusion frequency of the blue-sensitive mechanism of colour vision," The Journal of physiology **183**(2), 497-500 (1966).

109. L. Cohen, *Time-frequency analysis* (Prentice Hall PTR Englewood Cliffs, NJ:, 1995), Vol. 1406.

110. A. Kostenbauder, "Ray-pulse matrices: a rational treatment for dispersive optical systems," Quantum Electronics, IEEE Journal of **26**(6), 1148-1157 (1990).

111. F. Frei, A. Galler, and T. Feurer, "Space-time coupling in femtosecond pulse shaping and its effects on coherent control," The Journal of chemical physics **130**(3), 034302 (2009).

112. H. Vincenti, A. Borot, T. Hammond, K. T. Kim, J. Wheeler, C. Zhang, T. Ruchon, T. Auguste, J. Hergott, and D. Villeneuve, "Applications of ultrafast wavefront rotation in highly nonlinear optics," Journal of Physics B: Atomic, Molecular and Optical Physics **47**(12), 124004 (2014).

113. A. Weiner, *Ultrafast optics* (John Wiley & Sons, 2011), Vol. 72.

114. H. Vincenti and F. Quéré, "Attosecond lighthouses: how to use spatiotemporally coupled light fields to generate isolated attosecond pulses," Physical Review Letters **108**(11), 113904 (2012).

115. J. A. Wheeler, A. Borot, S. Monchocé, H. Vincenti, A. Ricci, A. Malvache, R. Lopez-Martens, and F. Quéré, "Attosecond lighthouses from plasma mirrors," Nature Photonics **6**(12), 829-833 (2012).

116. A. Zaukevičius, V. Jukna, R. Antipenkov, V. Martinėnaitė, A. Varanavičius, A. P. Piskarskas, and G. Valiulis, "Manifestation of spatial chirp in femtosecond noncollinear optical parametric chirped-pulse amplifier," JOSA B **28**(12), 2902-2908 (2011).

117. G. Zhu, J. Van Howe, M. Durst, W. Zipfel, and C. Xu, "Simultaneous spatial and temporal focusing of femtosecond pulses," Optics Express **13**(6), 2153-2159 (2005).

118. S. Akturk, X. Gu, P. Gabolde, and R. Trebino, "The general theory of first-order spatio-temporal distortions of Gaussian pulses and beams," Optics Express **13**(21), 8642-8661 (2005).

119. J. Ratcliffe, "Some aspects of diffraction theory and their application to the ionosphere," Reports on Progress in Physics **19**(1), 188 (1956).

120. J. W. Goodman, *Introduction to Fourier optics* (Roberts and Company Publishers, 2005).

121. G. C. Sherman, "Application of the convolution theorem to Rayleigh's integral formulas," JOSA **57**(4), 546-547 (1967).

122. K. Matsushima and T. Shimobaba, "Band-limited angular spectrum method for numerical simulation of free-space propagation in far and near fields," Optics Express **17**(22), 19662-19673 (2009).

VITA

MICHELLE A. RHODES

Michelle was born in Lilburn, Georgia. She attended public schools in Gwinnett County. She began her B.S. in Physics at the Georgia Institute of Technology in Atlanta before transferring to the University of Hawaii at Mānoa in Honolulu, Hawaii. She completed her degree in 2010 and returned to Georgia Tech to pursue a doctorate in Physics. Michelle enjoys electronic music, fantasy literature, and collaborative gaming.